Aalborg Universitet

AALBORG UNIVERSITY
DENMARK

Computational and Experimental Study of Bubble Size in Bubble Columns

Hansen, Rolf

Publication date:
2009

Document Version
Publisher's PDF, also known as Version of record

[Link to publication from Aalborg University](#)

Citation for published version (APA):
Hansen, R. (2009). *Computational and Experimental Study of Bubble Size in Bubble Columns*. Esbjerg Institute of Technology, Aalborg University.

Computational and Experimental Study of Bubble Size in Bubble Columns

Ph.D. thesis

Submitted by

Rolf Hansen

to The Faculty of Engineering and Science, Aalborg University
for the degree of Doctor of Philosophy.

Group for Chemical Fluid Flow Processes
Esbjerg Institute of Technology
Aalborg University Esbjerg
Niels Bohrs Vej 8
DK-6700 Esbjerg, Denmark

June 2009

Rolf Hansen
Computational and Experimental Study of Bubble Size in Bubble Columns.
Ph.D. thesis, Aalborg University Esbjerg, 2009.

Abstract

In this thesis an Eulerian two-phase Computational Fluid Dynamics (CFD) model for modelling bubble columns is presented. The model is able to predict bubble size with the use of an Interfacial Area Concentration Equation (IACE) coupled to the dispersed phase as a scalar transport equation. The IACE model is able to predict bubble coalescence and breakup and a resulting Sauter Mean Diameter (SMD) in the computational domain.

The bubble size distribution in a square bubble column is measured with the non-intrusive optical laser based method Interferometric Particle Imaging (IPI) and the bubble velocity is measured with Particle Tracking Velocimetry (PTV). The measurements are done for three superficial gas velocities in a plane in the middle of the bubble column. The IPI measurements show a bubble SMD of approximately 6.0mm in the entire field of view, which is also observed visually. Local bubble size histograms are presented in order to gain data for comparison of computational and experimental data. The experimental SMD seems to be constant in the axial direction, whereas it is decreasing radially toward the wall. It also seems that the experimental SMD is decreasing with increasing superficial gas velocity.

A computational analysis of the flow pattern in the square bubble column is done without employing the IACE model. Different interfacial forces and turbulence models are tested, and simulated velocity profiles are compared with experimental PIV data from the literature. Excellent agreement with the experimental data is obtained. It is observed that the lift force is essential for modelling the fluctuating behaviour of the bubble plume.

Two different kernels for bubble coalescence and breakup are implemented in the IACE model. Both kernels are tested on the square bubble column at three superficial gas velocities. The simulations show some agreement with experimental IPI data. The simulated SMD is decreasing in the axial direction, whereas the experimental SMD seems constant. In the radial direction the simulated SMD is decreasing toward the walls just like the experimental SMD. The simulated SMD is increasing with increasing superficial gas velocity. This is not seen in the experimental IPI data, where the SMD seems constant or even decreasing with increasing superficial gas velocity. Overall the kernels by Moilanen *et al.* (2008) seem to perform better than the kernels by Wu *et al.* (1998). The inclusion of bubble size dependent lift force does not yield good results, which is quite surprising.

A flat pseudo-2D bubble column is modelled with the IACE model and compared with experimental data from the literature. The kernels by Wu *et al.* (1998) are not able to predict the SMD satisfactorily. The SMD is decreasing axially, which is the opposite trend seen in the experiments. The kernels by Moilanen *et al.* (2008) do a better prediction of the axial SMD. Especially when employing both bubble size dependent lift and bubble induced turbulence. For the latter case the trend of the experimental SMD is captured, although the simulated SMD is about 50% higher than the experimental SMD.

Synopsis

I denne afhandling præsenteres en Eulerisk tofaset numerisk fluid-dynamik model til modellering af boblekolonner. Modellen kan beregne boblestørrelse ved brug af en grænsearealskoncentrationsligning (IACE), der er koblet til den spredte fase som en skalær transportligning. IACE-modellen kan beregne sammenklumpning og opbrydning af bobler, hvorved en Sauter gennemsnitsdiameter (SMD) beregnes i domænet.

Boblestørrelsesfordelingen måles i en kvadratisk boblekolonne med "Interferometric Particle Imaging" (IPI), som er en ikke-indtrængende optisk laserbaseret metode. Boblehastigheden måles samtidig med "Particle Tracking Velocimetry" (PTV). Målingerne udføres for tre superficielle gashastigheder i en plan i midten af boblekolonnen. IPI-målingerne viser en SMD på omkring 6.0mm for hele måleområdet, hvilket også er observeret visuelt. Lokale boblestørrelseshistogrammer præsenteres for at få data, der kan sammenlignes med beregningerne. Den eksperimentelle SMD synes at være konstant lodret gennem boblekolonnen, men faldende fra midten ind mod væggen horisontalt. Den eksperimentelle SMD synes også at falde med stigende superficiel gashastighed.

En beregningsanalyse af flowmønstret i den kvadratiske boblekolonne er udført uden brug af IACE-modellen. Forskellige grænsefladekræfter og turbulensmodeller er testet, og simulerede hastighedsprofiler er sammenlignet med eksperimentelle PIV data fra litteraturen. Simuleringerne viser god enighed med eksperimentelle data. Det er observeret at løftekraften er essentiel for at modellere den fluktuerende opførsel af den opstigende boblekaskade.

To forskellige kerner, der kan beregne sammenklumpning og opbrydning af bobler er implementeret i IACE-modellen. Begge kerner er testet på den kvadratiske boblekolonne ved tre forskellige superficielle gashastigheder. Simuleringerne viser nogen enighed med de eksperimentelle IPI data. Den simulerede SMD falder med stigende højde i boblekolonnen, hvor den eksperimentelle SMD synes at være konstant. Fra midten af boblekolonnen ud mod væggene viser den simulerede SMD en faldende tendens, hvilket den eksperimentelle SMD også gør. Den simulerede SMD stiger med stigende superficiel gashastighed. Dette er ikke observeret ud fra de eksperimentelle IPI data, hvor SMD synes at være konstant eller endda faldende med stigende superficiel gashastighed. Alt i alt synes kernen fra Moilanen *et al.* (2008) at give bedre resultater end kernen fra Wu *et al.* (1998). Inkludering af boblestørrelsesafhængig løftekraft giver ikke gode resultater, hvilket er ret overraskende.

En flad psudo-2D boblekolonne modelleres med IACE-modellen, og resultaterne er sammenlignet med data fra litteraturen. Kernen fra Wu *et al.* (1998) er ikke i stand til at beregne en tilfredsstillende SMD. SMD falder med stigende højde i boblekolonnen, hvilket er den modsatte tendens sammenlignet med eksperimentelle data. Kernen fra Moilanen *et al.* (2008) er bedre til at beregne SMD i boblekolonnen sammenlignet med eksperimentelle data, især hvis den boblestørrelsesafhængige løftekraft samt bobleinduceret turbulens er inkluderet i modellen. Med disse indstillinger viser simuleringen den samme tendens i SMD som de eksperimentelle data med stigende højde i boblekolonnen, dog er den simulerede SMD ca. 50 % højere end den eksperimentelle værdi.

Acknowledgements

Contents

Nomenclature

A	Area	[m^2]
a	Area concentration	[m^{-1}]
a_i	Interfacial area concentration	[m^{-1}]
C	Second random collisions model constant	[-]
C_{BIT}	Model constant in the BIT formulation	[-]
C_D	Drag coefficient	[-]
C_L	Lift coefficient	[-]
C_{RC}	Random collisions model constant	[-]
C_{TI}	Turbulent impact model constant	[-]
C_{VM}	Virtual mass coefficient	[-]
C_{WE}	Wake entrainment model constant	[-]
d_a	Aperture diameter	[m]
d_B	Bubble diameter	[m]
d_p	Particle diameter	[m]
E	Bubble aspect ratio	[-]
$E\ddot{o}$	Eötvös number	[-]
$E\ddot{o}_d$	Modified Eötvös number	[-]
f	Focal length	[m]
g	gravity	[m/s^2]
I	Unit tensor	[-]
M_D	Drag force	[N/m^3]
$M_{I,k}$	Interfacial force per unit volume of phase k	[N/m^3]
M_L	Lift force	[N/m^3]
M_{VM}	Virtual mass force	[N/m^3]
m	Relative refractive index	[-]
N_f	Number of fringes	[-]
n_x	Number of pixels in the x-direction	[-]
P	Porosity	[-]
p	Pressure	[Pa]
Q	Flow rate	[m^3/s]
Re_B	Bubble Reynolds number	[-]

S	Characteristic filtered rate of strain	$[\text{s}^{-1}]$
S_a	Interfacial area source/sink rate	$[\text{m}^{-1}\cdot\text{s}^{-1}]$
t	Time	$[\text{s}]$
U	Time average velocity	$[\text{m/s}]$
u	Velocity	$[\text{m/s}]$
u_f	Root mean square velocity between two bubbles	$[\text{m/s}]$
u_r	Relative velocity	$[\text{m/s}]$
u_{rw}	Relative velocity averaged over the wake length	$[\text{m/s}]$
V	Volume	$[\text{m}^3]$
We	Weber number	$[-]$
We_{cr}	Critical Weber number	$[-]$
z	Distance to lightsheet	$[\text{m}]$
z_r	Position of the camera behind the lens	$[\text{m}]$
z_l	Minimum standoff distance	$[\text{m}]$

Greek Letters

α	Volume fraction	$[-]$
Δ	Filter width	$[\text{m}]$
Δx	Dimension of CCD array in the x-direction	$[-]$
ε	Turbulent dissipation rate	$[\text{m}^2/\text{s}^3]$
ϕ	Off-axis angle	$[°]$
κ	Geometric factor	$[\text{m}^{-1}]$
λ	Wave length	$[\text{m}]$
μ	Dynamic viscosity	$[\text{kg/m}\cdot\text{s}]$
ρ	Density	$[\text{kg/m}^3]$
σ	Surface tension	$[\text{N/m}]$
τ	Stress term	$[\text{kg/m}\cdot\text{s}^2]$
Ψ	Shape factor	$[-]$

Subscripts

B	Bubble
Bm	Bubble mean
eff	Effective
G	Gas phase
i	Interfacial
k	k^{th} phase

L	Liquid phase
Lam	Laminar
min	Minimum
max	Maximum
o	Orifice
RC	Random collisions
sup	Superficial
TI	Turbulent impact
t	Turbulent
WE	Wake entrainment
We	Weber
x	Coordinate
y	Coordinate
z	Coordinate

Abbreviations

AMD	Advanced Micro Devices
BIT	Bubble Induced Turbulence
BSD	Bubble Size Distribution
CCD	Charged Coupled Device
CFD	Computational Fluid Dynamics
CM	Classes Method
CPU	Central Processing Unit
DQMOM	Direct Quadrature Method Of Moments
FFT	Fast Fourier Transform
FoV	Field of View
IACE	Interfacial Area Concentration Equation
IPI	Interferometric Particle Imaging
IPL	Image Processing Library
LDA	Laser Doppler Anemometry
LES	Large Eddy Simulation
MUSIG	MUltiple-SIze-Group
PBE	Population Balance Equation
PCA	Parallel Classes Approach
PDA	Phase Doppler Anemometry
PIV	Particle Image Velocimetry
PPDC	Parallel Parent and Daughter Class
PTV	Particle Tracking Velocimetry

QMOM   Quadrature Method Of Moments
SMD   Sauter Mean Diameter
VOF   Volume Of Fluid

Chapter 1

Introduction

1.1 Bubble columns

Bubble columns are used in a variety of industrial processes as reactors, absorbers or strippers etc. Bubble columns have distinct advantages when compared to other gas-liquid contactors. Two of these are the simple construction and the absence of moving mechanical parts. Therefore the bubble column is easy to construct and maintain.

The optimal configuration of a bubble column can be determined experimentally or computationally. Experimental determination of an optimal configuration requires a series of steps. Typically a lab scale model is set up and experiments are done. A pilot scale plant is then built based on the findings on the lab scale and further experiments are done. In the end the full scale bubble column is built into an existing plant from the experiences obtained with the pilot plant using scale-up laws. This process is time consuming and quite expensive.

Computational Fluid Dynamics (CFD) can provide data which is not obtainable from traditional experimental techniques in less time and with fewer costs. Because of the dramatic increase in computing power over the last few decades, the usage of CFD for designing and optimizing unit operations has increased immensely. CFD should however be used with caution as the mathematical closures implemented in CFD codes are seldom universal. It is of great importance to validate mathematical closures against experimental data to see if the closures can be used for a small or large range of applications.

1

Detailed review papers on modelling of bubble columns using CFD are available from Jacobsen *et al.* (1997) and Rafique *et al.* (2004).

1.2   Experimental data

It is of interest to conduct experimental studies of the flow pattern and Bubble Size Distribution (BSD) in a variety of bubble columns because of the need for validation of theoretical models. Experimental data on the flow pattern in bubble columns are available from different studies. Some of these are mentioned in the following.

Becker *et al.* (1994) measured the flow in a flat rectangular bubble column with Laser Doppler Anemometry (LDA) and measuring probes and anemometers. The inlet was located 10cm to the left of the centre in the bottom plate.

Borchers *et al.* (1999) studied the flow in a flat rectangular bubble column and measured the liquid velocity with LDA. The inlet was located in the centre of the bottom plate.

Becker *et al.* (1999) studied the time dependent flow behaviour of the liquid phase in a flat rectangular bubble column with focus on the dynamics of circulation flows. The measurement method was LDA. The inlet was located in the centre of the bottom plate.

Delnoij *et al.* (2000) employed a new ensemble correlation multiphase flow Particle Imaging Velocimetry (PIV) technique in a flat bubble column. The technique featured a single camera setup compared to the known two-camera PIV setup. The inlet was located near the right wall in the bottom plate.

Bröder & Sommerfeld (2000) employed a two camera PIV/PTV (Particle Tracking Velocimetry) system to measure the flow in a circular bubble column. Fluorescent particles were added to the continuous phase to be able to measure the liquid velocity.

Deen (2001) measured the flow in a square bubble column with PIV and LDA. The inlet of the bubble column was placed in the centre of the bottom plate.

Bubble size has bee measured with a variety of measuring techniques in different bubble columns. A few studies are presented in the following.

Lage and Espósito (1999) measured bubble diameters of air bubbles in aqueous isopropanol photographically in a bubble column at different superficial gas velocities. The diameter of the bubbles was determined manually and BSDs were fitted from the data.

Laín et al. (1999) used a two-component Phase Doppler Anemometer (PDA) to measure bubble size distribution and velocities of both phases in a circular bubble column.

Magaud et al. (2001) used a dual optical probe technique to measure void fraction, bubble size and bubble velocity in a vertical rectangular channel. The technique is based on changes in the optical index of the medium located at the probe tip.

Van den Hengel (2004) used a shadow imaging technique to measure the bubble size in a flat rectangular bubble column. The

Majumder et al. (2006) used a shadow imaging technique to determine the BSD and the gas-liquid specific interfacial area as a function of axial location, nozzle diameter and superficial gas and liquid velocities in a modified bubble column.

This work is a continuation of the work done on a square bubble column by Deen (2001). Since the flow pattern in the square bubble column is already mapped, the emphasis should be on measuring the bubble size distribution in the square bubble column.

1.3   Flow modelling

Besides measuring the flow pattern in the square bubble column with LDA and PIV, Deen (2001) also did a computational analysis of the flow pattern with CFD. Deen (2001) compared computations, which showed good agreement with experimental data.

Deen *et al.* (2001) found that the standard k-ε turbulence model was not able to capture the dynamic behaviour of the bubble plume inside the column. Therefore a Large Eddy Simulation (LES) sub-grid approach proposed by Smagorinsky (1963) was employed, which was able to simulate the large scale fluctuations and thereby the dynamic behaviour of the bubble plume, provided that essential interfacial forces were also employed. Zhang *et al.* (2005) successfully predicted the dynamic behaviour in the square bubble column using a k-ε turbulence model extended with Bubble Induced Turbulence (BIT).

It was also found by Deen (2001) that careful choice of the interfacial forces was important. It was observed that the lift force was an essential interfacial force. Zhang *et al.* (2006) did a more thorough study of different interfacial forces on the square bubble column. Zhang *et al.* (2006) also observed that the lift force plays a critical role for capturing the dynamic behaviour of the bubble plume.

1.4   Modelling bubble size

Bubble size plays an important role in a gas-liquid contactor such as a bubble column. The mass transfer between phases is directly related to the surface area of gas bubbles. Therefore it is important to know the BSD. A bubble column is a dynamic system, where bubbles collide with walls and other bubbles, resulting in bubble coalescence and bubble breakup. Bubble coalescence and breakup can also be induced by turbulence which complicates matters significantly. The resulting bubble size distribution in a bubble column as a function of operating conditions is therefore difficult to describe computationally.

A number of different approaches to modelling bubble size exist. A few are mentioned in the following.

Wu *et al.* (1998) used an Interfacial Area Concentration Equation (IACE) to model one dimensional vertical bubbly flow. Here the IACE is solved by a scalar transport equation in the dispersed phase of a two-phase flow. Ishii and Kim (2001) used the latter IACE model to predict one dimensional bubbly flow in round pipes. Moilanen *et al.* used a modified version of the latter IACE model to predict bubble size and mass transfer in an aerated vessel.

Sanyal *et al.* (2005) compared the performance of Population Balance Equations (PBE) in bubble columns. The PBEs were the Classes Method (CM) and the Quadratic Method Of Moments (QMOM). With CM the BSD is divided into N classes, and the number density equation is solved for each class. With QMOM 2N moments are tracked and a pd-algorithm is used for obtaining the BSD, which is represented by N size classes.

Bove *et al.* (2005) use a PBE approach to model the bubble size in bubble columns. The PBE was split into a convective part and a coalescence-breakage part. The convective part was solved with the Parallel Classes Approach (PCA) and the coalescence-breakage part was then solved with the Parallel Parent and Daughter Class (PPDC) approach.

Cheung *et al.* (2007) used a PBE approach with the MUSIG model and three different IACE models by Wu *et al.* (1998), Hibiki & Ishii (2002) and Yao & Morel (2004) to predict bubble size in isothermal vertical bubbly flow.

Krepper *et al.* (2008) modelled the BSD with a generalized inhomogeneous MUSIG model. Here the dispersed phase was divided into N velocity groups each having its own velocity field, and the overall BSD was represented by dividing the bubble diameter range within each of the velocity groups.

Bannari *et al.* (2008) used a Classes Method PBE to model bubble size in bubble columns. Here the BSD was represented through a finite number of bubble classes.

In this work the bubble size distribution in bubble columns will be modelled with the IACE approach.

1.5   Objectives of the current work

The objectives of this study are to determine the bubble size distribution in a square bubble column experimentally and computationally, and to compare the computations with the experimental data. Furthermore the computational model should be tested on a different bubble column and compared with experimental data.

1.6   Organization of the thesis

In Chapter 2 the experimental work done on a square bubble column is presented for three superficial gas velocities. IPI and PTV are used for determining bubble size and bubble velocity respectively.

The theory behind CFD for multiphase flow is presented in Chapter 3. Also the specific models for modelling the flow and bubble size in the bubble column are presented.

In Chapter 4 the numerical simulations of the flow pattern in the square bubble column are presented. The simulations are run with different turbulence- and interfacial forces presented in Chapter 3. Furthermore the simulations are run with two different inlet conditions. The results are compared with a selected simulation by Deen (2001) and the PIV experiments by Deen (2001).

Numerical simulations of bubble size in the square bubble column are presented for three superficial gas velocities in Chapter 5. The bubble size is calculated with the IACE model. Two different kernels for coalescence and breakup are used in the simulations. The simulated bubble size is compared to experimental IPI data from Chapter 2 and velocity profiles are compared to PIV data by Deen (2001).

Additional bubble size simulations on a flat pseudo 2D bubble column with the IACE model are presented in Chapter 6. The simulations are compared to experimental data by van den Hengel (2004).

In Chapter 7 a summary on the discoveries in this thesis is given and conclusions are drawn. Furthermore an outlook on future work is presented.

Chapter 2

Experiments

2.1 Introduction

In this chapter the theory behind the Interferometric Particle Imaging with Particle Tracking Velocimetry (IPI/PTV) optical laser based measurement technique is presented. Furthermore the experimental setup and the results from the experiments are presented.

IPI is a relatively new imaging technique for determining the diameter of spherical transparent particles and its origins can be traced back to König *et al.* (1986) who focused a single laser beam onto a stream of monodispersed droplets and measured the resulting fringe pattern in the out-of-focus field (Albrecht *et al.,* 2003). The possibility of combining the method with Particle Image Velocimetry (PIV) was then discussed by Glover *et al.* (1995).

The strength of the IPI technique is its ability to measure the instantaneous bubble diameter and velocity of spatially distributed bubbles (Madsen, 2006). Furthermore the IPI sizing technique is readily implemented in the standard and well known Particle Image Velocimetry (PIV) setup by employing an extra camera, which means that it is possible to do instantaneous whole-field measurements of the particle diameter instead of point measurements as for Phase Doppler Anemometry (PDA).

The whole-field measurements will not only yield the size of the bubbles, but also the position because the bubbles are registered individually. By

using double exposure imaging, the velocity components of the bubble can then be evaluated with PTV (Dantec, 2003).

2.2   Interferometric Particle Imaging (IPI)

When focusing a camera on a transparent bubble that has been illuminated by a coherent laser sheet, the scattered light will produce two bright spots or glare points on a Charged Coupled Device (CCD) chip (as seen from the receiver). One glare point represents the reflected ray and the other glare point represents the refracted ray. This is shown in Figure 1.

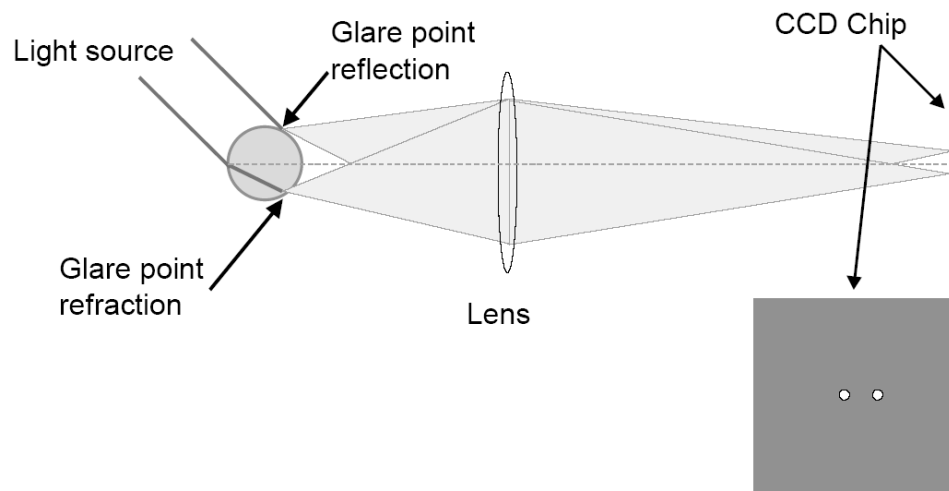*Figure 1   Glare points on the CCD chip generated by the reflected and refracted light respectively (Dantec, 2003).*

The existence of both glare points is dependent on the light scattering properties of the particle-medium and the off-axis angle of the receiver.

By defocusing the camera with respect to the particle the two glare points will interfere to produce measurable fringes on a CCD array, which is illustrated in Figure 2.
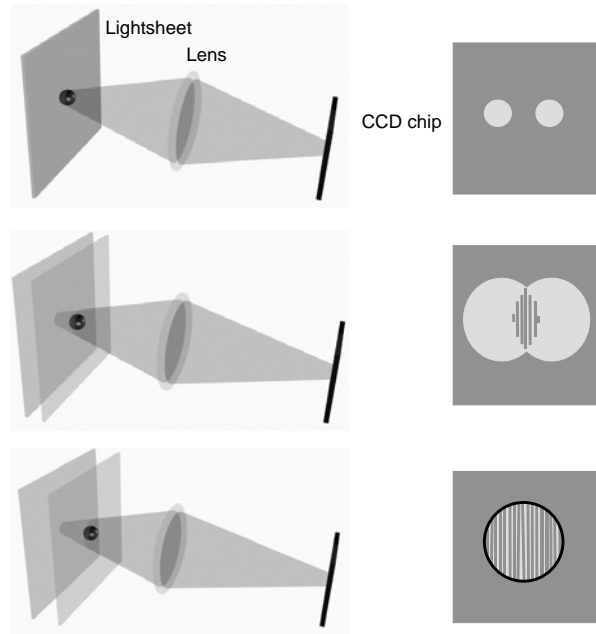
Figure 2   Generation of fringes by moving the focus plane of the camera away from the plane of the light sheet and particle (Madsen et al., 2003).

From the frequency of the fringes it is possible to determine the distance between the glare points and thereby the size of the particle. In order to get good image quality (contrast), the relative refraction index (m) should be below 0.8 or above 1.2 (Dantec, 2003). Since this study deals with air bubbles in water (m=0.75), this condition is satisfied.

The sphericity of the particles is important, because of the orientation of the fringes. A particle with a sphericity of unity will yield horizontal fringes, whereas a particle with sphericity below unity will angle the fringes relative to the horizontal position. This means that the angle is a good measure for validation of the particle diameter.

The size of the out-of-focused particle image is independent of particle size, but rather on particle position in the light sheet and the amount of user applied defocusing.

2.2.1   Numerical relations

The relationship between the number of fringes N_f and the particle diameter d_p is linear and given by Hesselbacher *et al.* (1991):

$$N_f = \kappa \, d_p \tag{1}$$

where κ is the geometric factor. When measuring air bubbles in water, $m < 1$ and κ is found from (Maeda *et al.*, 2000):

$$\kappa = \frac{sin^{-1}\left(\dfrac{d_a}{2z}\right)}{\lambda}\left[m\,cos\frac{\phi}{2} - \frac{m\,sin\dfrac{\phi}{2}}{\sqrt{m^2 + 1 - 2m\,cos\dfrac{\phi}{2}}} \right] \tag{2}$$

where d_a is the aperture diameter, z is the distance to the lightsheet, λ is the wavelength and ϕ is the off-axis angle.

The minimum particle diameter is given by the following relationship, which is the size represented by a fringe count of unity:

$$d_{min} = \frac{1}{\kappa} \tag{3}$$

Here the generally accepted minimum diameter that can be measured is 5-8 microns (Madsen, 2006).

The maximum particle diameter is given from the Nyquist criteria, where at least two pixels define the existence of a fringe (Dantec, 2003):

$$d_{max} = \frac{n_x}{2\kappa \Delta x}\left[1 - z_r\left(\frac{1}{f} - \frac{1}{z_1}\right) \right] \tag{4}$$

where n_x is the number of pixels in the x-direction, Δx is the dimension of the CCD array in the x-direction, z_r is the position of the camera behind the lens, f is the focal length and z_1 is the minimum standoff distance (see Figure 3). In practice, fringes exhibit gradients and are not perfectly

straight, so a more reasonable requirement is three or four pixels per fringe (Madsen, 2006).
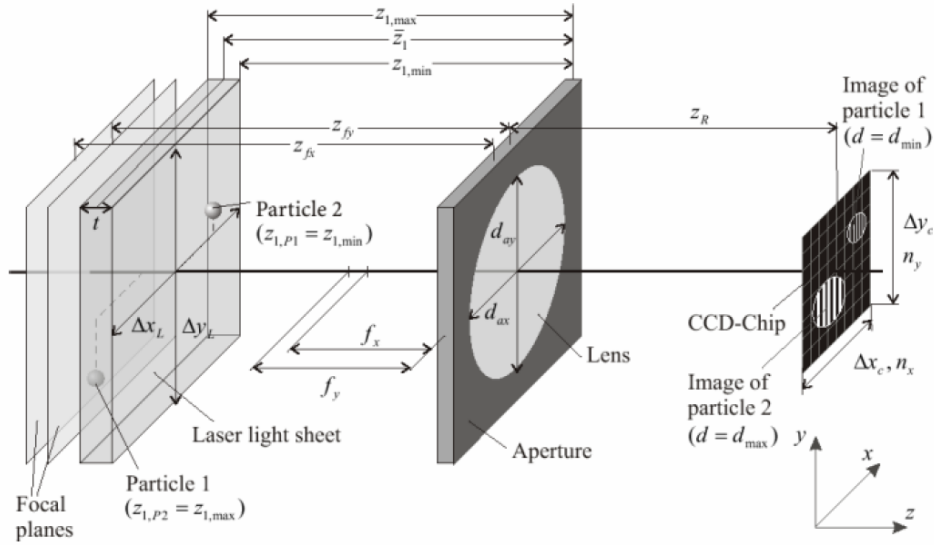

Figure 3   Optics schematics (Albrect, 2003).

The maximum particle size that can be measured will depend on the size of the out-of-focus particle image, the optic configuration, and the camera resolution (Madsen, 2006). From the equations for κ and d_{max} there are a number of parameters that need to be determined in order to define d_{min} and d_{max}. However in practice there are only a few parameters that are adjustable (not defined by the measurement equipment) such as z, ϕ and n_x, where z and ϕ are used for defining both d_{min} and the field of view and n_x is used for defining d_{max}. When ϕ and z and thereby d_{min} has been chosen, d_{max} can only be increased by user controlled defocusing. There is however a trade-off between defocusing and image contrast. When defocusing the number of detectable fringes increase, but the signal to noise ratio will become lower. Therefore it is important to select a suitable d_{min}, so that the level of defocusing can be kept to a minimum.

A representative image of fringes from an out of focus image is shown in Figure 4. The range of fringes present can be seen to range from approximately 2 to 30.
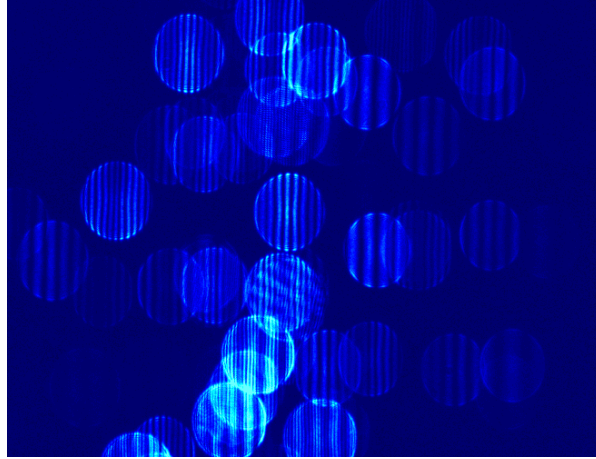
Figure 4   Out-of-focus image showing fringes (Madsen et al., 2003).

2.3   Particle Tracking Velocimetry (PTV)

Particle tracking Velocimetry (PTV) is used for determining the velocity of the particles. PTV is used instead of PIV when the number of particles in the image is sparse.

In an IPI setup, an out of focus camera is recording the bubble size and the in focus camera is recording the position of the particle. By using double exposure on the in focus camera, the displacement of the particle between bursts is recorded. It is therefore possible to calculate the velocity of the particle, which is done with PTV.

PTV is done in four steps. First a cross-correlation is done for double exposure images. This generates vectors that represent the flow direction of particles in local areas. For each of the particles in frame 1 a comparison is done for each of the particles in frame 2 using the cross-correlation. Thereby matching each particle in frame 1 with likely candidates in frame 2. Statistics are then employed to determine, which of the candidates is most likely the perfect match. The velocity is then determined from the pixel displacement of the particle and the time between the double exposure (Dantec, 2003). This is illustrated in Figure 5.
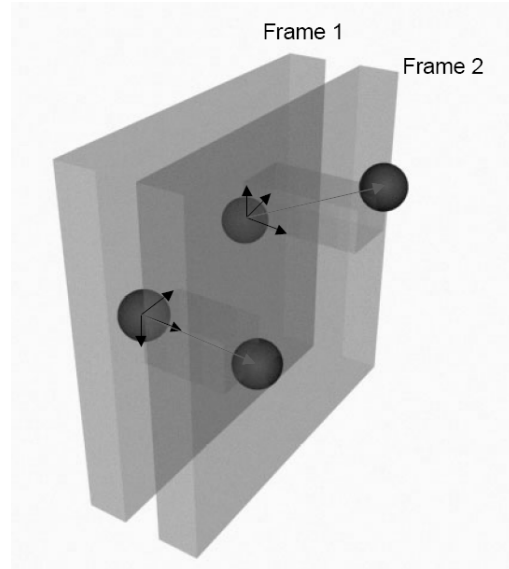
Figure 5   Illustration of PTV (Dantec, 2003).

When doing PTV an optimal time between bursts (double exposure) is important. If the time is too short, the pixel displacement will be none for some of the particles and the velocity will be zero. If the time between exposures is too long, the cross-correlation and statistics will fail to predict the matching pair of particles between frame 1 and 2. The time between exposures is found by doing tests before acquiring data. When the data is acquired it is obviously not possible to change the exposure time in order to produce better PTV results.

2.4   Experimental setup

Measurements were done on a square bubble column with dimensions 0.15m x 0.15m x 1m (water level at 0.45m). The column is built in Plexiglas and raised from the ground in a steel skeleton, so that optical access is possible. A sketch of the square bubble column can be seen in Figure 6.
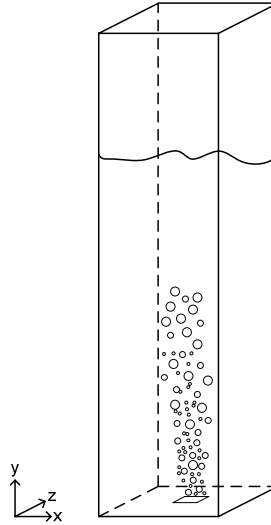
Figure 6   Sketch of the square bubble column.

The inlet of the square bubble column is a distributor plate with 49 holes with diameter of 1 mm at a square pitch of 6.25 mm (see Figure 7). The plate is expected to yield bubbles with a mean diameter of 4mm (Deen, 2001). The inlet is centred in the bottom of the column.
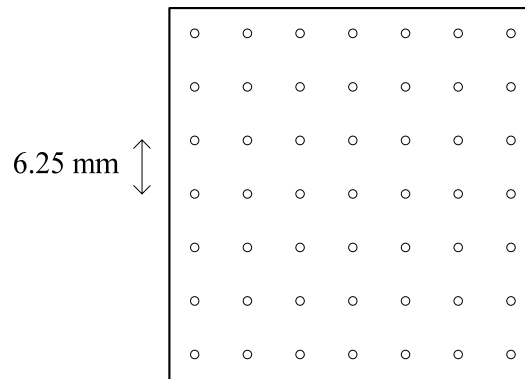
Figure 7   The distributor plate in the bottom of the bubble column.

The experimental setup is a Dantec FlowMap Particle Sizer system at Aalborg University Esbjerg, which consists of a laser, two cameras, traversing unit, a Dantec Flowmapper and a PC. The cameras were placed parallel to one another and directed onto a common viewing area

at an angle to the light sheet. The laser source was a 120 mJ double-pulsed Nd:YAG laser at $\lambda = 532$ nm with a repetition frequency of 15 Hz, and a laser sheet thickness of about 1.0mm. The laser light was polarized perpendicular to the laser sheet. The cameras used were 8-bit Kodak MegaPlus ES1.0 digital CCD cameras with a resolution of 1008 × 1016 pixels. For both cameras a 60mm objective lens was used. The cameras and laser head were mounted on a 3D traversing unit, so it was possible to access almost the entire column. The size of measurement area was approximately 0.15m × 0.12m. Double images were acquired in order to be able to measure velocities of the dispersed phase with PTV. Dantec Dynamic Studio software was used for the post-processing of the acquired data. In Figure 8 a schematic representation of the experimental setup is shown.
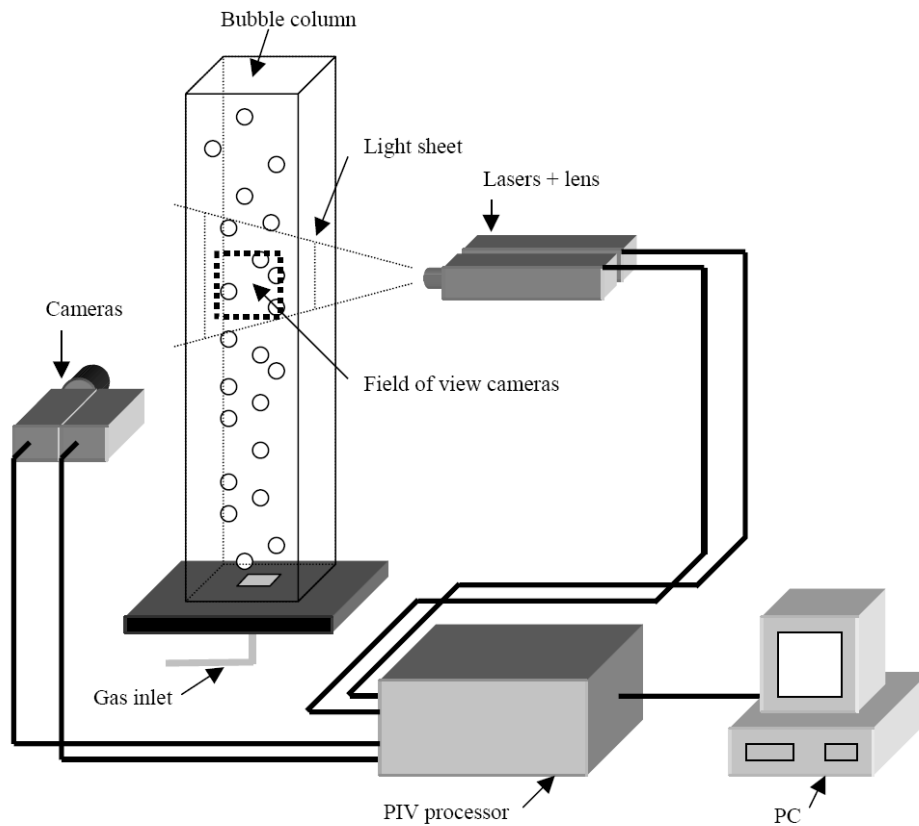

Figure 8   Schematic representation of the experimental setup (Deen, 2001).

Distilled water and air at room temperature was used in all experiments. Following the work by van den Hengel (2004), a small amount of Octanol (10^{-4} kmol/m^3) was added in order to obtain almost spherical bubbles. When the Octanol was added, a significant visible effect was seen. The column looked like it was boiling erratically as soon as the Octanol was added, but after a while the bubble plume went back to normal behaviour and the bubbles were significantly more spherical than before.

The measurements were done at a single location in the bubble column, where the centre of the camera was fixed vertically at y = 0.25m and the measurement plane (field of view) was fixed at a depth of z = 0.075m. This is shown in Figure 9.
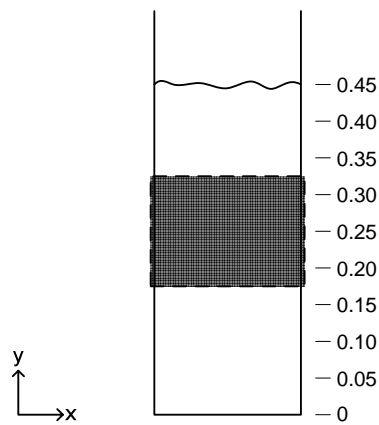
Figure 9   Sketch of the measurement location. The centre of the rectangular field of view is located at a height of 0.25m. The plane of measurement is located at a depth of 0.075m.

Deen (2001) recorded PIV data in the bubble column at a superficial gas velocity of 4.9 mm/s, so this velocity is naturally chosen as the starting point for obvious comparison reasons. Two other superficial gas velocities were also planned, and it was observed that with a superficial gas velocity above 6.6 mm/s the bubble plume started to act differently in the column. This velocity was chosen as the upper limit. The lower limit was then set to 3.2 mm/s, so that the velocity 4.9 mm/s was right in the middle of the limits. Measurements were then done at three different superficial gas velocities: 3.2 mm/s, 4.9 mm/s and 6.6 mm/s.

The aim of the measurements was to be able to measure the width of the bubble column in every picture, and that a sufficiently large bubble diameter could be detected. The adjustable parameters in the experimental setup *z*, ϕ and n_x were chosen accordingly.

The distance to the light sheet, z, was determined together with the off-axis angle ϕ. For bubbles in liquid, the off-axis angle ϕ should be positioned below 45° as can be seen from the example in Figure 10.
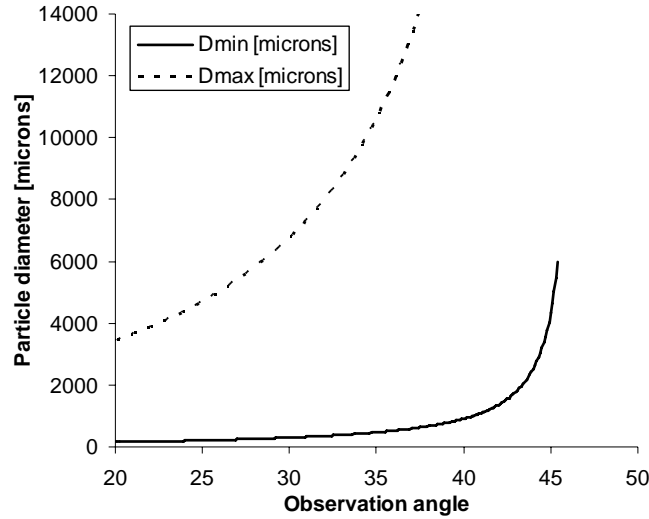
Figure 10   Example of minimum and maximum diameter as a function of observation angle with z = 0.9m (Hansen et al., 2007).

It is observed from Figure 10 that with z = 0.9m, ϕ should be less than 40° as the slope of d_{min} increases rapidly with $\phi > 40°$. n_x is set to 90 pixels in Figure 10 in order to show the maximum detectable diameter. After multiple tests and considerations ϕ is set to 35° and $n_{x,max}$ was set to 90, which was regarded as being the maximum value, as the noise level began to dominate.

The number of samples was set to 10,000 image pairs per run. It was found during the initial test runs that every image pair yielded approximately 10 validated bubbles, which gives 10^5 bubbles per run. If the field of view (0.15m × 0.13m) is divided into a 7 x 6 grid, only

approximately 2300 validated bubbles will be found in each grid cell on average. This is regarded as being appropriate for statistical analysis on the data.

The experimental settings are listed in Table 1.

Table 1   Experimental settings.

Variable	Setting
Wavelength of laser (λ)	532 nm
Distance to the light sheet (z)	0.9 m
Aperture diameter (d_a)	21.4 mm
Defocused bubble diameter	~ 80 pixels
Camera angle (ϕ)	35°
Samples per run	10000 image pairs
Time between bursts (PTV)	1000 ms
Superficial air velocity	3.2, 4.9 and 6.6 mm/s
Water level	0.45 m (Deen 2001)

2.5   Post processing of acquired experimental data

After acquiring the data, it was processed using Dantec Dynamic Studio software. Here the IPI and PTV processing was done simultaneously. The processing of a single measurement with 10,000 image pairs took approximately 60 hours on an AMD 2.1 GHz CPU from 2007.

2.5.1   IPI processing

The IPI processing is done in several steps. First a bubble is spotted on the focused image. The location of the bubble in the focused image is then used for finding a matching defocused bubble in the defocused image. If a match is found, the circle size of the defocused bubble is determined.

If the bubble is overlapping with another bubble, the overlap is masked (ignored), and the remaining measurable area is calculated (Dantec, 2003). This is shown in Figure 11.
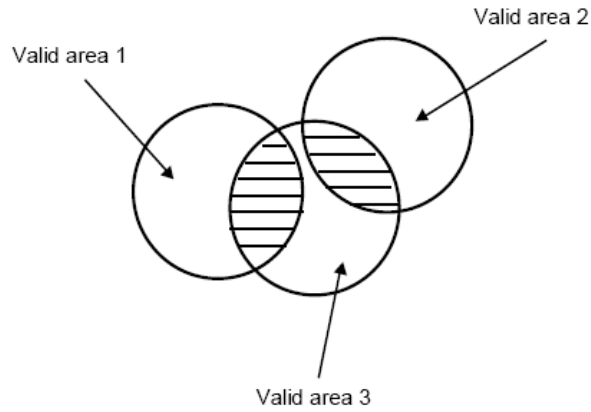
Figure 11   Defocused bubble images are overlapping. The overlapping areas are masked (Dantec, 2003).

A 2D FFT and a 2D Gaussian interpolation are then employed to determine the dominant frequency peak, from which the diameter of the bubble can be determined using Eqs. 3 and 4.

In Figure 12, the influence of the overlap on frequency determination is shown. The error in the frequency calculation of an overlap of 46% and 92% is 3% and 5% respectively (Dantec, 2003).

0 % overlap	46 % overlap	92 % overlap

Peak frequency=21.1	Peak frequency=20.4	Peak frequency=20.1
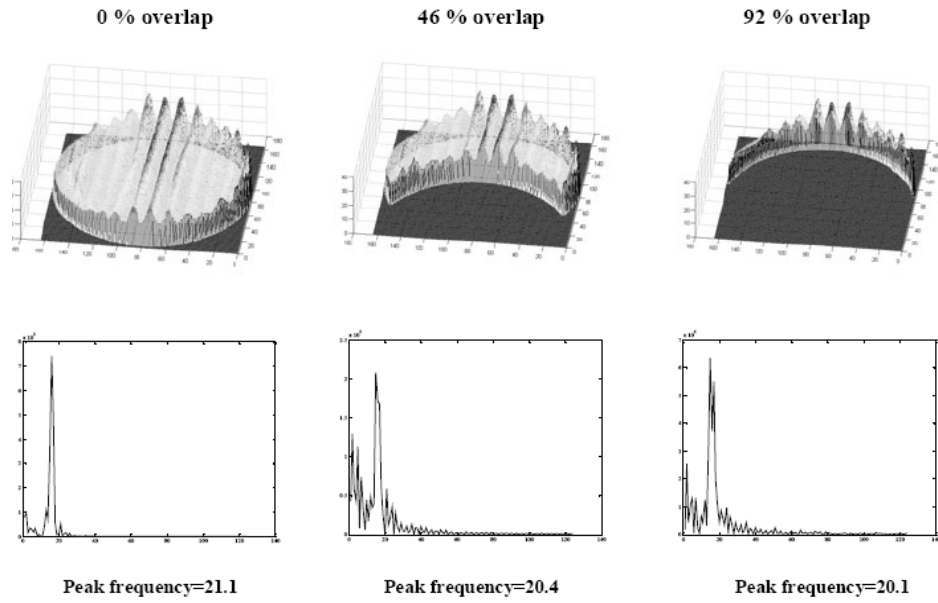
Figure 12   Influence of the overlap on frequency determination (Dantec, 2003).

Before doing IPI on the raw images it can be a good idea to do filtering on the images with the built-in Image Processing Library (IPL). When experiencing weak fringes or fringes varying in intensity on the defocused image, it is recommended to use a high pass filter to remove the low frequency information. Also one can use a low pass filter to remove extraneous background noise (Dantec, 2003). In Figure 13 a defocused image with and without IPL filtering is shown.

Figure 13   Left: defocused image of two detected bubbles showing fringe patterns. Right: With IPL filtering. (Hansen et al., 2007).

In the left image, two detected bubbles are showing fringes of different quality. The bubble on the left is clearly showing a fringe pattern, whereas the bubble on the right is not showing a clea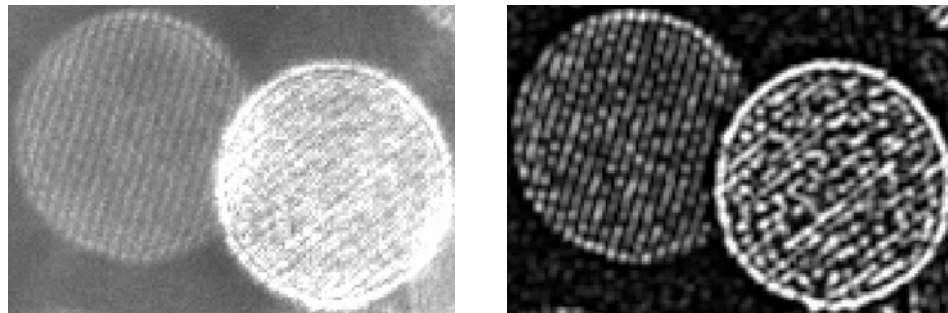r fringe pattern. Using IPL on the raw defocused image with a high pass and a low pass filter yields the image on the right. It is now possible to see a fringe pattern in the bubble on the right. The high pass filter removes the low frequency information, so that the fringes are easy to spot, whereas the low pass filter removes the background noise.

The bubble on the left was validated and the bubble on the right was rejected by the software. The rejection is either due to peak level validation or frequency ratio validation. The quality of the fringe pattern in the bubble on the right is simply too poor.

2.5.2   IPI validation

When doing the IPI analysis a number of validation parameters have to be determined. There are four important settings: frequency ratio, peak level, overlap and image brightness (Dantec, 2003).

- A frequency ratio threshold is set in order to reject bubbles with no or poor fringe definition. As the frequency in the x-direction is more dominant than in the y-direction for IPI measurements an Fx / Fy ratio threshold is employed.
- A peak level threshold rejects bubbles with a peak level lower than a percentage of the maximum peak determined.
- An overlap threshold is employed to ensure that the error in the frequency determination is kept at a minimum.
- A bubble detection threshold on the focused image ensures that faint bubbles, detected on the focused image, will be matched on the defocused image, as a faint bubble will not yield fringes on the defocused image.

2.5.3 PTV validation

The most important parameter of the PTV analysis is the size of the interrogation area. The entire field of view of the camera is divided into smaller interrogation areas. The size of the interrogation area varies from 16 (4x4) to 256 (16x16) pixels in Dantec Dynamic Studio. When doing PTV on flows with few bubbles the interrogation area should be as large as possible. As a rule of thumb there should be a minimum of 10-11 bubbles present per interrogation area (Dantec, 2003).

2.5.4 IPI/PTV settings

The IPI/PTV post processing settings are listed in Table 2.

Table 2   IPI/PTV post processing settings.

Variable	Setting
Minimum size of defocused image	70 pixels
Maximum size of defocused image	90 pixels
Window type	Hanning
Window strength	0%
Validation peak level threshold	3 %
Validation allowable overlap	70 %
Validation Fx/Fy frequency ratio threshold	1
IPL filtering	No
Interrogation area	256 pixels
Background noise removal	50 %

For the current experimental setup the resulting diameter range is found to be $0.472mm < d_B < 10.620mm$.

The effect of IPL filtering was investigated on the defocused images, but as the number of bubble counts increased with approximately 50%, this filtering method was discarded.

2.6   Results

In this section the results from the experiments are presented. The section is divided into two parts, bubble size distribution and bubble velocity. Bubble size histograms along with statistics and profiles of bubble velocities are shown for all three superficial gas velocities (3.2, 4.9 and 6.6 mm/s).

2.6.1   Bubble size distribution in the bubble column

Entire field of view

In Figure 14 - Figure 16 bubble size distributions (BSD) are shown for the entire field of view (Figure 9) for all three superficial velocities.

Diameter Histogram

D10 = 2397.29 µm
Counts = 82998
s.d. = 1967.54 µm
D20 = 3101.32 µm
D30 = 3927.75 µm
D32 = 6299.99 µm
D43 = 8028.97 µm
Valid Conc. = 1 #/cm³
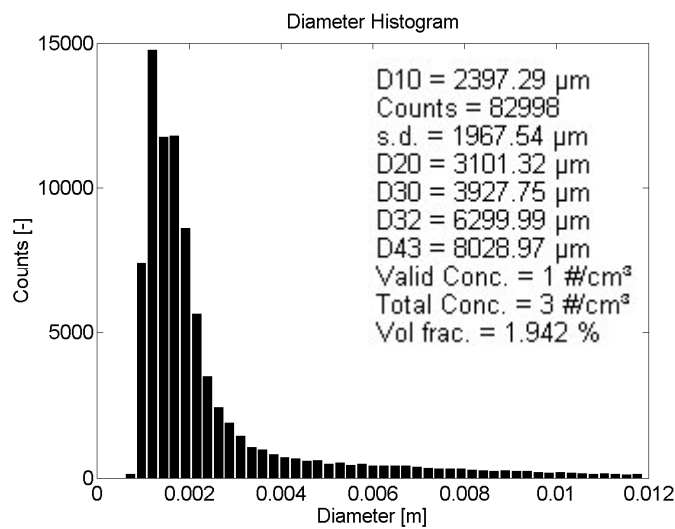Total Conc. = 3 #/cm³
Vol frac. = 1.942 %

Figure 14   BSD in the entire field of view for $u_{sup,G}$ = 3.2 mm/s. Number of bins: 50.

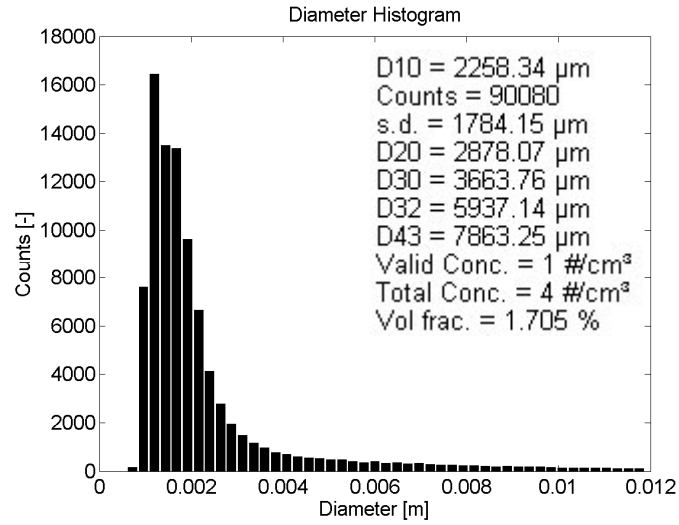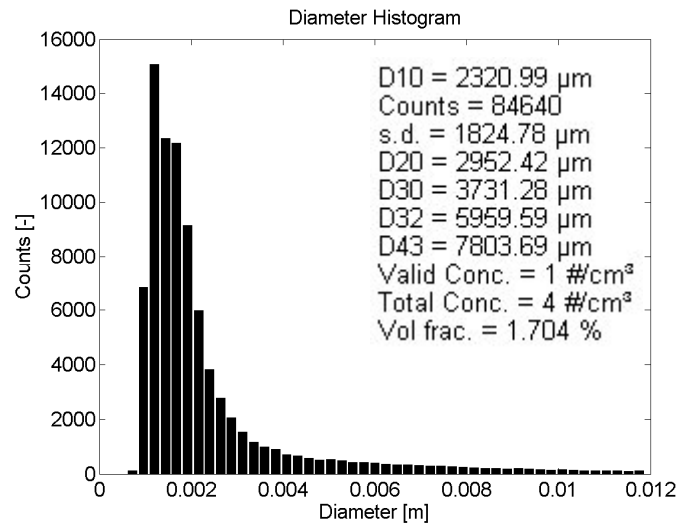*Figure 15   BSD in the entire field of view for $u_{sup,G}$ = 4.9 mm/s. Number of bins: 50.*

Figure 16   BSD in the entire field of view for $u_{sup,G}$ = 6.6 mm/s. Number of bins: 50.

As expected Figure 14, Figure 15 and Figure 16 show a Poisson distribution. The highest number of bubble counts is in the range 1.2-2.4mm. From this point the number of counts decreases potentially with

increasing diameter. The d_{10} and d_{32} is approximately 2.3mm and 6.0mm respectively and the total diameter count is approximately 85000. During the experiments the diameter was observed visually to be around 5-6mm, which is in good agreement with the measured d_{32}. The number of bubble counts, the mean bubble diameters d_{10} and d_{32} and the standard deviation for all three superficial gas velocities measured are listed in Table 3.

Table 3   Statistical data for bubble diameter histograms

Variable	$u_{G,sup}$ = 3.2 mm/s	$u_{G,sup}$ = 4.9 mm/s	$u_{G,sup}$ = 6.6 mm/s
Counts [-]	82998	90080	84640
d_{10} [mm]	2.40	2.26	2.32
d_{32} [mm]	6.30	5.94	5.96
s.d. [mm]	1.97	1.78	1.82

Detailed histograms are shown in Figure 17 with bubble sizes ranging from 3mm.
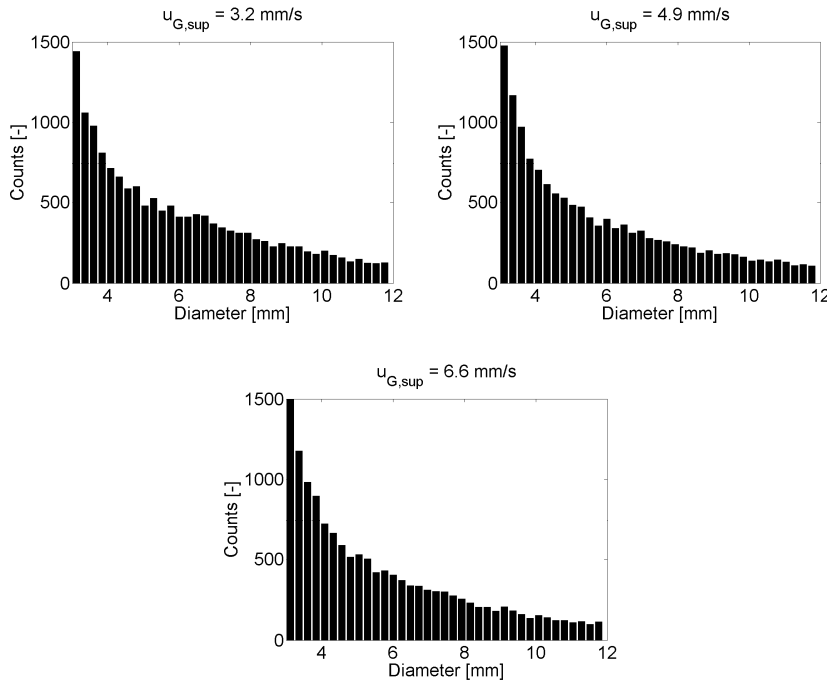

Figure 17   Histograms of bubble sizes ranging from 3mm for all three superficial gas velocities for the entire field of view.

Local bubble size distributions

Instead of looking at the entire field of view it would be interesting to see
if local variations occur in the field of view. Therefore five different
locations of 2x2 cm^2 in the field of view are investigated. The five
locations are shown in Figure 18.
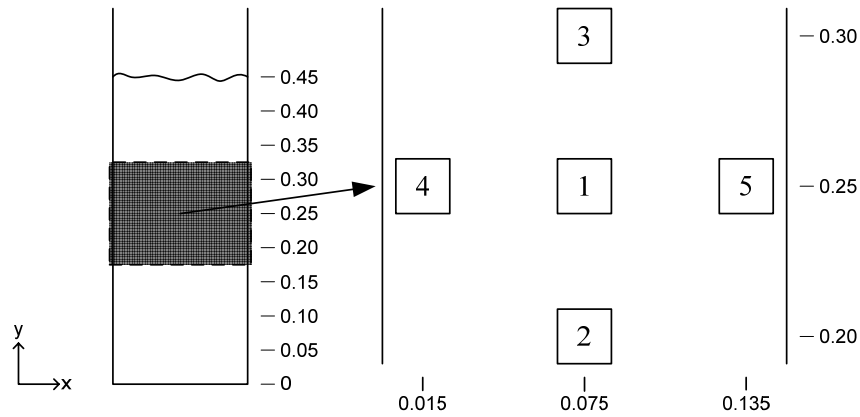
Figure 18   Sketch of the five different locations in the field of view.

Figure 19, Figure 20 and Figure 21 show bubble size histograms for the
five locations at all three superficial gas velocities.

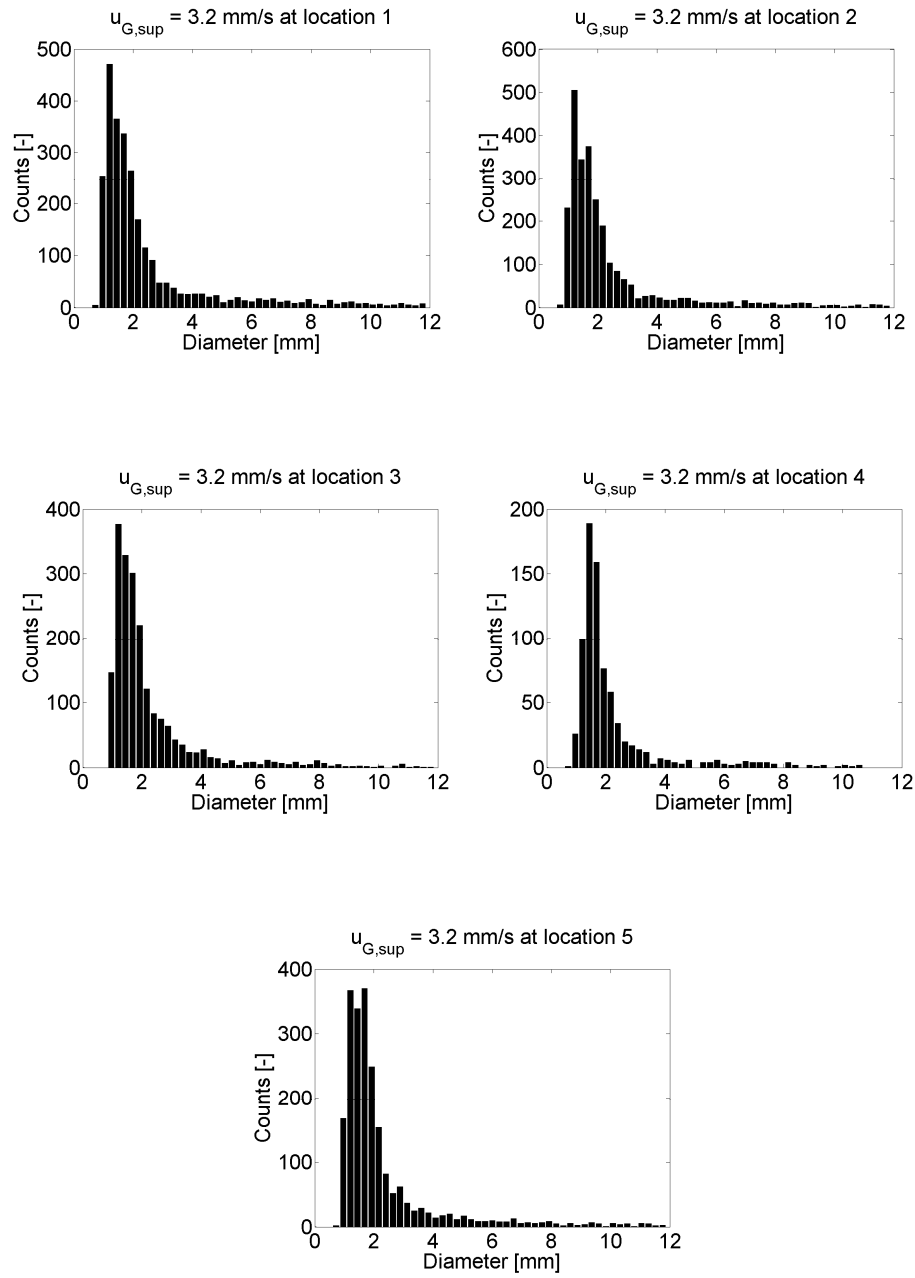*Figure 19   Histograms of bubble size for the five different locations in the field of view. Superficial gas velocity 3.2 mm/s.*
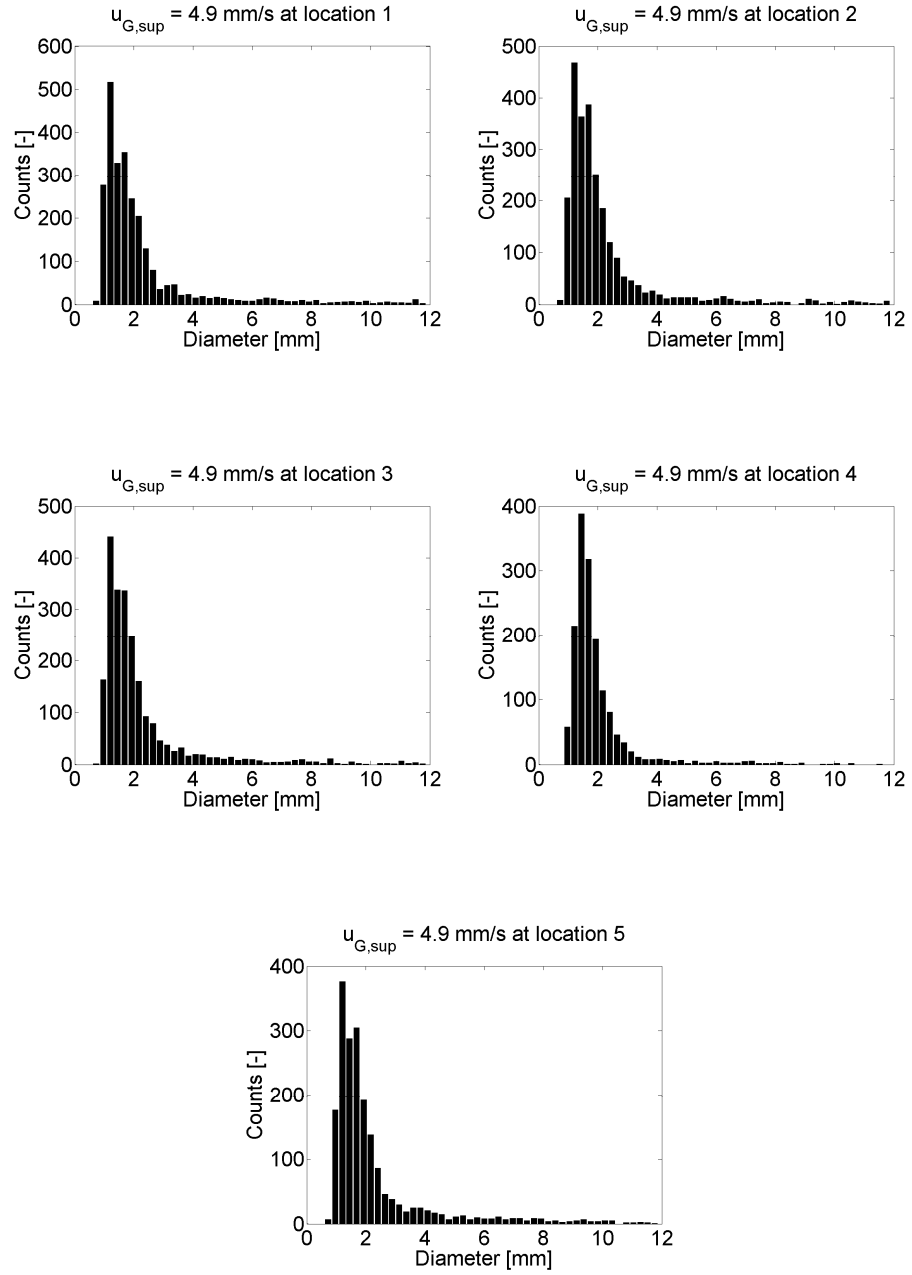
Figure 20   Histograms of bubble size for the five different locations in the field of view. Superficial gas velocity 4.9 mm/s.
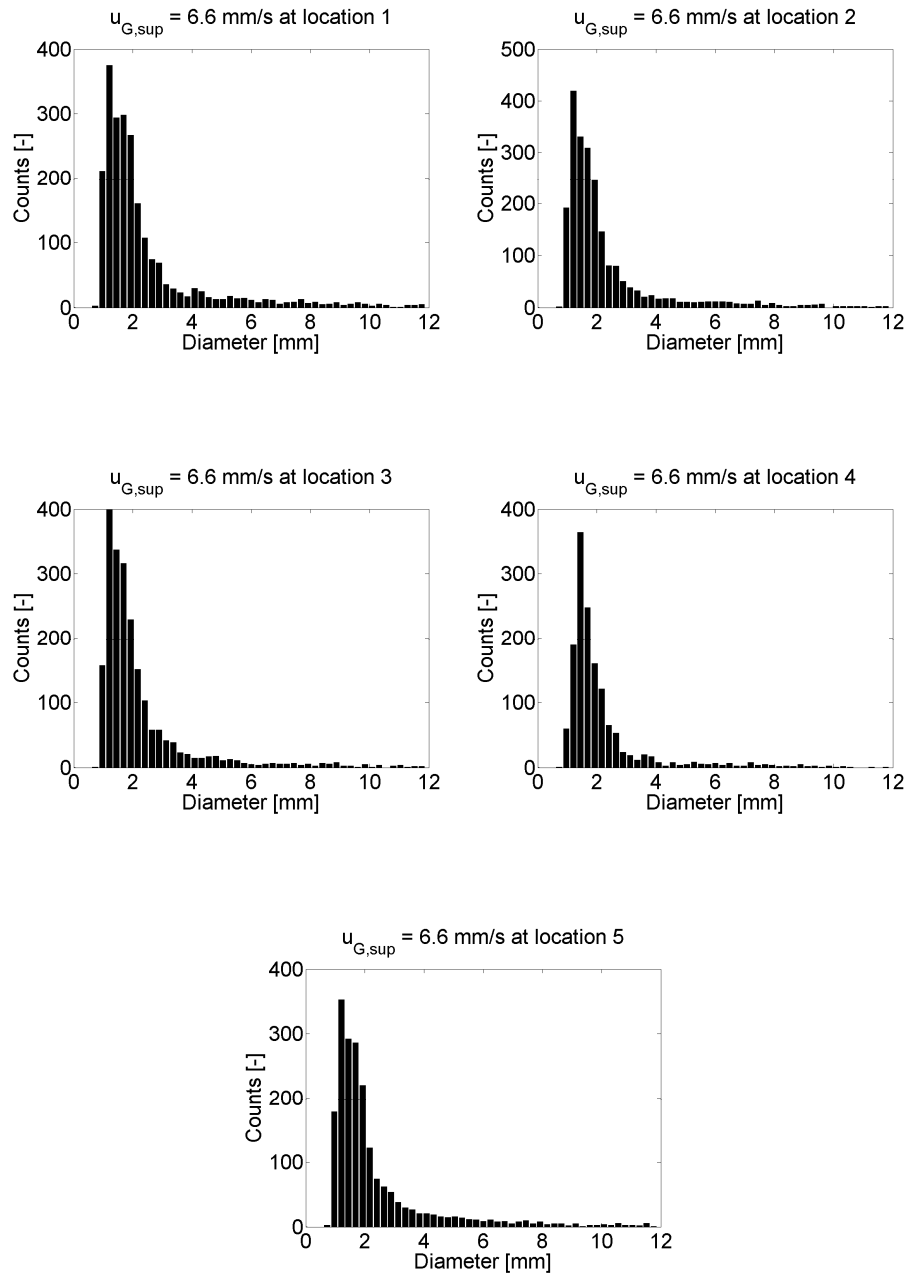
Figure 21 Histograms of bubble size for the five different locations in the field of view. Superficial gas velocity 6.6 mm/s.

The histograms in Figure 19 - Figure 21 are observed to be very similar. Statistical data from the histograms are listed in Table 4.

Table 4   Comparison of statistical data for bubble diameter at five different locations and the entire field of view (FoV).

Variable	Loc. 1	Loc. 2	Loc. 3	Loc. 4	Loc. 5	FoV
$U_{G,sup}$ = 3.2 mm/s						
Counts [-]	2662	2614	2047	793	2208	82998
d_{10} [mm]	2.52	2.38	2.24	2.23	2.32	2.40
d_{32} [mm]	6.74	6.38	5.58	5.35	6.09	6.30
s.d. [mm]	2.15	1.98	1.66	1.62	1.84	1.97
$U_{G,sup}$ = 4.9 mm/s						
Counts [-]	2621	2521	2255	1583	1982	90080
d_{10} [mm]	2.34	2.27	2.25	2.00	2.29	2.26
d_{32} [mm]	6.52	6.12	5.84	4.39	5.95	5.94
s.d. [mm]	1.99	1.82	1.75	1.24	1.83	1.78
$U_{G,sup}$ = 6.6 mm/s						
Counts [-]	2275	2221	2145	1473	2013	84640
d_{10} [mm]	2.43	2.28	2.23	2.17	2.35	2.32
d_{32} [mm]	6.21	5.85	5.59	5.20	6.02	5.96
s.d. [mm]	1.95	1.79	1.68	1.54	1.86	1.82

From the results in Table 4, the difference in d_{10} is observed to be small with respect to location for all three superficial gas velocities. The difference in d_{32} is a bit larger. The number of counts in location 4 is noticed to be low compared to the other locations in all three measurements.

In Figure 22 the average d_{32} from Table 4 is plotted in the axial direction.
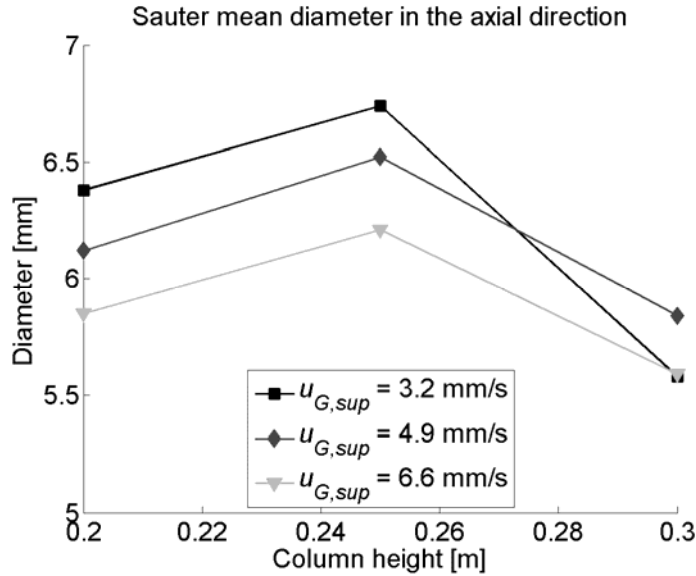
Figure 22 Sauter mean bubble diameter at the axial centreline at a depth of 0.075m.

It is observed that the average d_{32} decrease with increasing superficial gas velocity except for location 3 (y = 0.30). The maximum d_{32} is found in location 1 for all three superficial gas velocities, which seems a little strange as an increasing, decreasing or even steady mean bubble diameter is expected with increasing height (y).

In Figure 23 the average d_{32} from Table 4 is plotted in the radial direction. It is observed that the average d_{32} is decreasing toward the walls for all three superficial gas velocities. The maximum diameter for all three measuring locations is found with the lowest superficial gas velocity. It is not evident here that the average d_{32} is indeed decreasing with increasing superficial gas velocity.
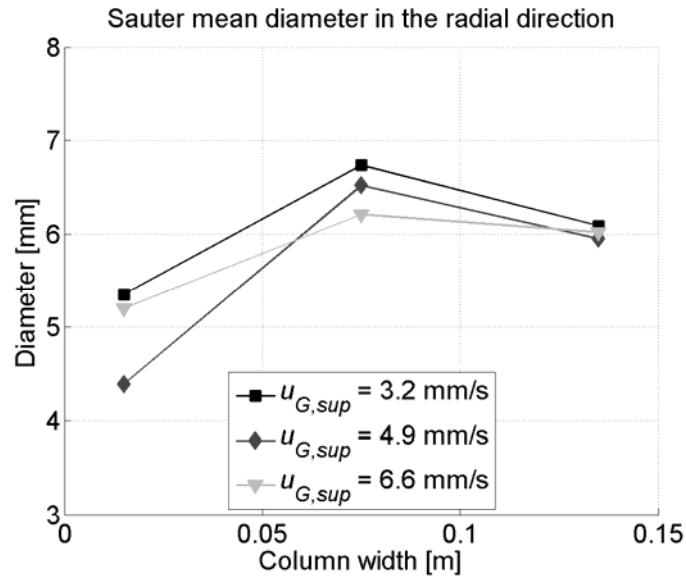
Figure 23 Sauter mean bubble diameter in the radial direction at a height of 0.25m and a depth of 0.075m.

2.6.2   Bubble velocity

The bubble velocity is calculated with PTV. Vector plots and line plots are shown for all three superficial gas velocities and the measurement with $u_{G,sup}$ = 4.9 mm/s is compared with experimental data by Deen (2001).

Vector plots of velocity magnitude for the entire field of view are shown in Figure 24 for all three superficial gas velocities.

Figure 24   Vector plots of experimentally determined velocity magnitude for the entire field of view. From left to right: 3.2, 4.9 and 6.6 mm/s.

The velocity vectors seem to be pointing in the axial direction as expected. There are however two certain locations in all the plots, where all neighbouring vectors are pointing toward each other. This unphysical behaviour is believed to be due to mirroring effects in the column.

In Figure 25 the velocity vectors from Figure 24 are shown without the radial component for all three superficial velocities.
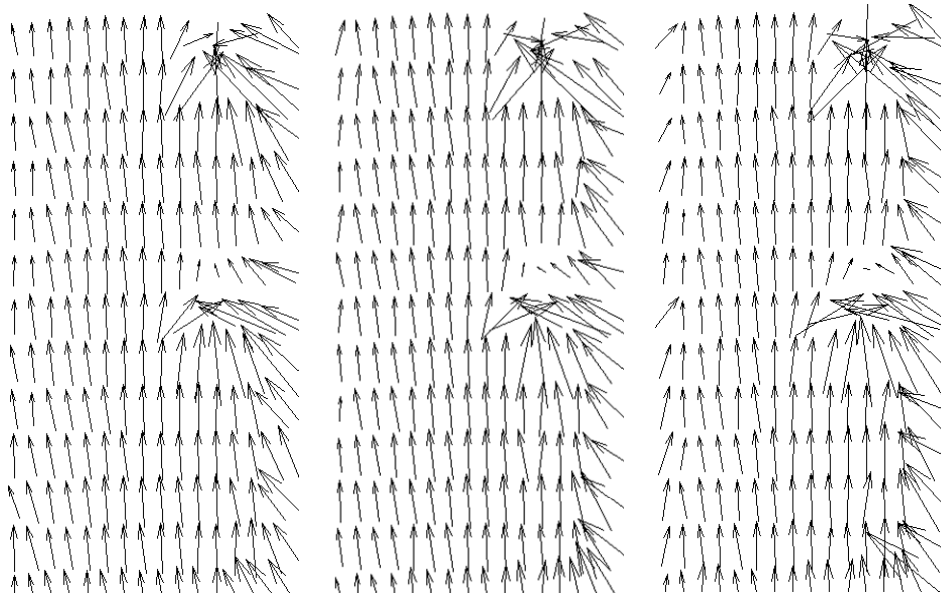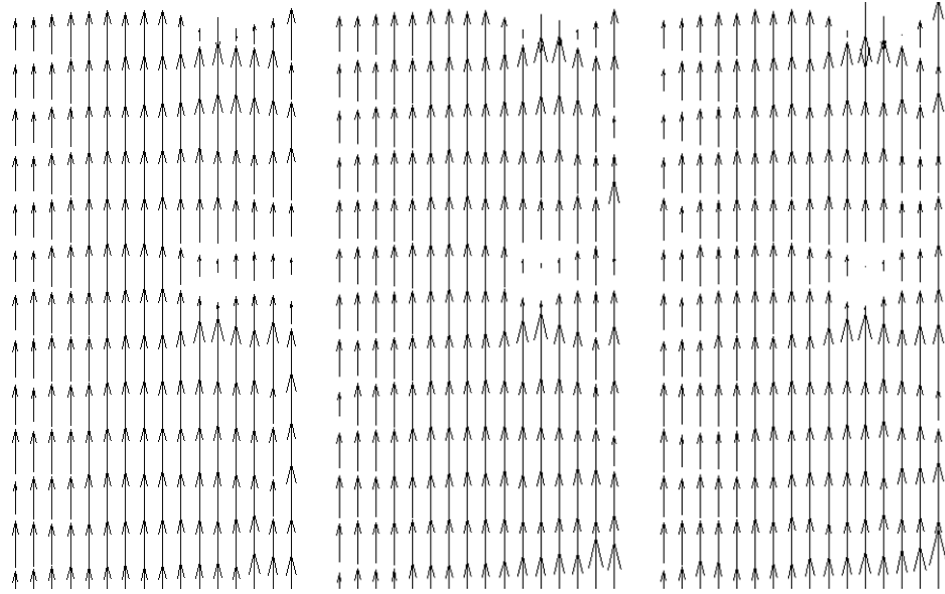
Figure 25   Vector plots of experimentally determined axial velocity for the entire field of view. From left to right: 3.2, 4.9 and 6.6 mm/s.

It is observed that the there are both positive and negative vectors in the vicinity of the two "mirroring" locations. This is expected from the plots in Figure 24.

Velocity profiles of the axial velocity are shown in Figure 26 for all three superficial gas velocities. Because of the "mirroring" effect at y = 0.25m the profiles are shown at y = 0.275m.
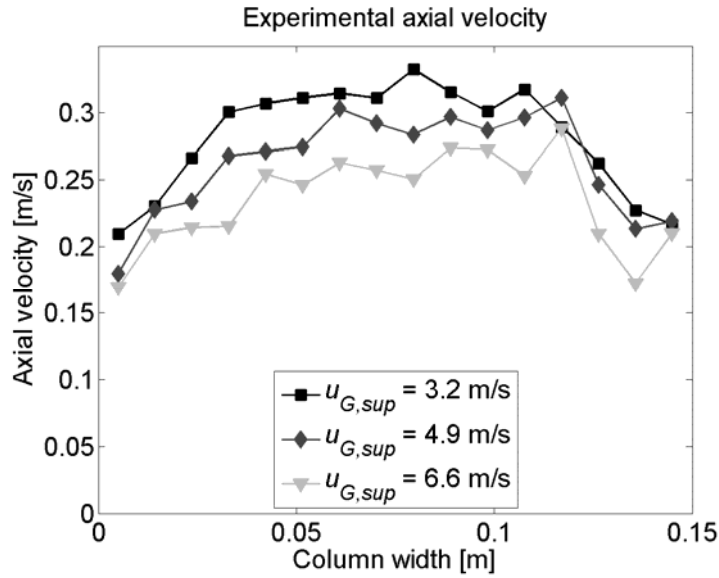
Figure 26 Velocity profiles of time averaged axial velocity for all three velocities at y = 0.275m and z = 0.075m.

The core velocity is noticed to be decreasing with increasing superficial velocity. This was not expected. This trend was also discovered by Dillerop (2000), who did PIV experiments on the bubble column. Velocity profiles from the study by Dillerop with different superficial gas velocities are shown in Figure 27.
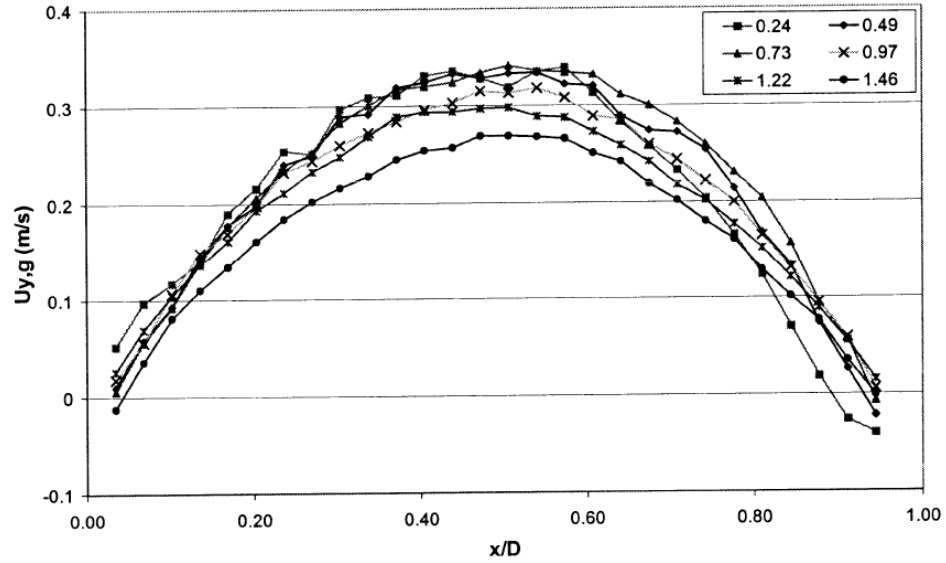
*Figure 27   Time averaged axial gas velocity for different superficial gas
           velocities in y = 0.352m and z = 0.075m. Superficial gas
           velocities are reported in cm/s in the legend (Dillerop, 2000).*

The results from Figure 27 show that the time averaged gas velocity is
decreasing with increasing $u_{G,sup}$, this is however only the case when
$u_{G,sup}$ is above 9.7 mm/s. When $u_{G,sup}$ is below 9.7 mm/s, the velocity
profile is not changing. It should be noted that the results in Figure 27 are
at a height of 0.352 m, so they are not directly comparable with the PTV
data in Figure 26. It is however believed that the trend from Figure 27
will be the same in a height of 0.25m.

Since the superficial gas velocities in this thesis are smaller than 9.7
mm/s, a different reason for the decreasing gas velocities must exist. The
time between bursts may have been set too large in the experiment,
resulting in bad correlation of data. If this is the problem it may explain
why the bubble velocity is decreasing with increasing superficial gas
velocity, as the bubble displacement grows larger with increasing
superficial gas velocity. The time between bursts can only be changed by
repeating the experiment
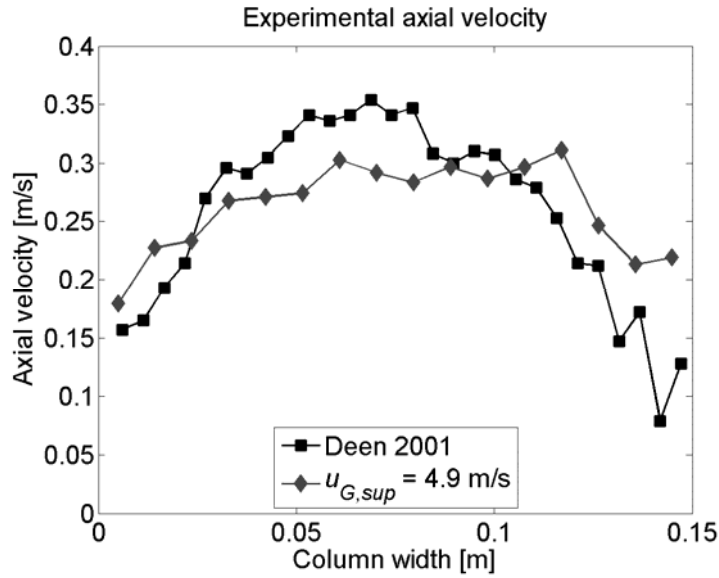
Figure 28   Velocity profiles of time averaged axial velocity for $u_{G,sup}$ = 4.9 mm/s in y = 0.275m and z = 0.075m Experimental data by Deen (2001) is in y = 0.025m.

From Figure 28 it is evident that the PTV data is not in very good agreement with the PIV data by Deen (2001). The core velocity is too low and the velocity toward the walls is a bit too high.

Interpolated PIV data

In addition to the PIV measurements at a superficial gas velocity of 4.9 mm/s, Deen (2001) also did PIV measurements at superficial gas velocities of 2.4 mm/s and 7.3 mm/s. The PIV data from all three superficial velocities (2.4, 4.9 and 7.3 mm/s) are therefore interpolated to yield pseudo experimental data at superficial gas velocities of 3.2 mm/s and 6.6 mm/s. In Figure 29 the interpolation is shown for superficial velocity 3.2 mm/s.

Figure 29   Velocity profiles of time averaged experimental PIV data by Deen (2001) and interpolated PIV data for a superficial gas velocity of 6.6 mm/s at a height of y = 0.25m and a depth of z = 0.075m.

It is observed that the liquid and gas core velocity are more or less constant for superficial velocities of 2.4 and 4.9 mm/s. The significant difference in the velocity profiles between the two measurements is found for the fluctuations, which decrease with decreasing superficial velocity. In the work by Dillerop (2000) it was observed with PIV that the axial gas velocity was constant for superficial gas velocities between 2.4mm/s and 7.3 mm/s at a height of 0.352m, which is also seen at y = 0.25m in the PIV data by Deen (2001). It was also observed by Dillerop (2000) that the axial liquid velocity was significantly lower with a superficial velocity of 2.4 mm/s at a height of 0.352m. This is not seen in the PIV data by Deen (2001) at y = 0.25m.

In Figure 30 the interpolation of PIV data is shown for superficial velocity 6.6 mm/s.
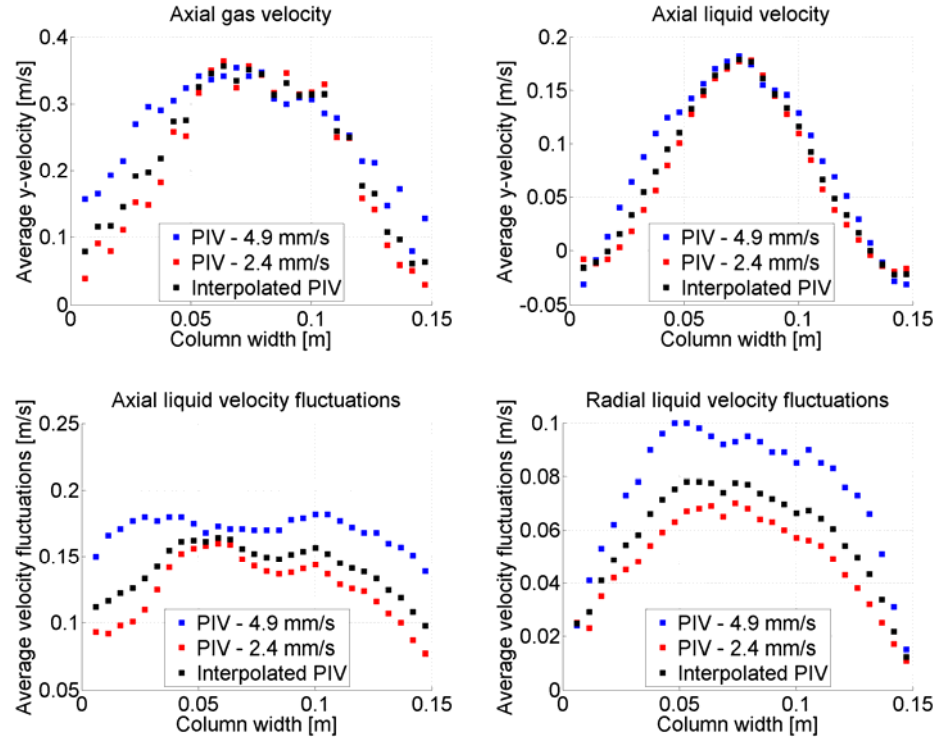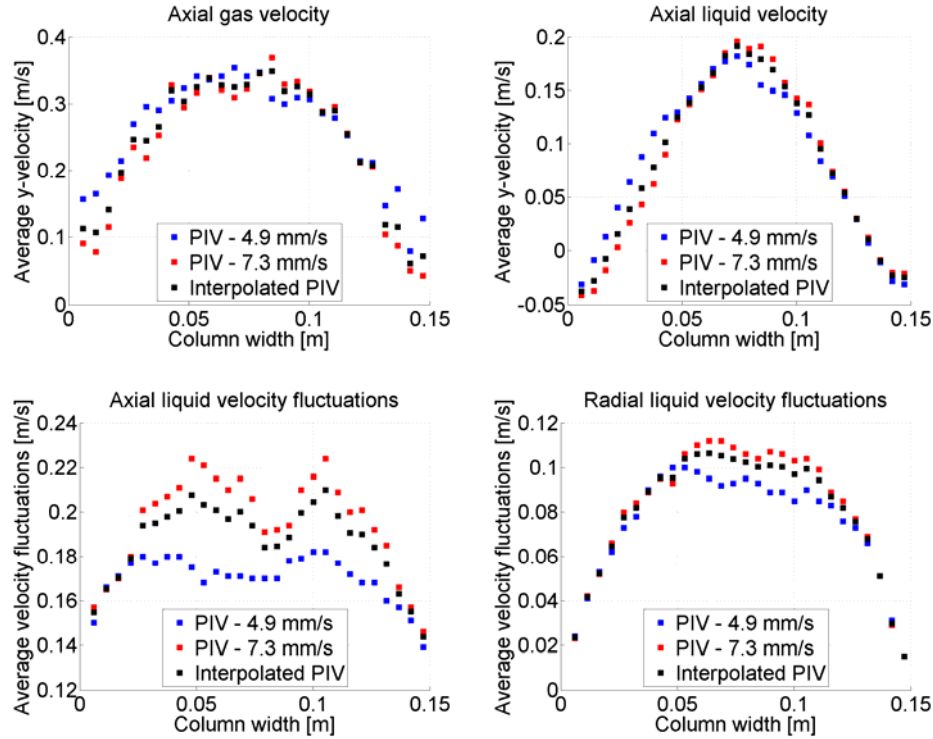
*Figure 30   Velocity profiles of time averaged experimental PIV data by
            Deen (2001) and interpolated PIV data for a superficial gas
            velocity of 6.6 mm/s at a height of y = 0.25m and a depth of z
            = 0.075m.*

From Figure 30 it is observed that the axial gas velocity is a little bit
lower with a superficial velocity of 7.3 mm/s compared to a superficial
velocity of 4.9 mm/s when looking at the core velocity. The opposite is
seen for the axial liquid velocity. It is also observed that the velocity
fluctuations are higher with a superficial velocity of 7.3 mm/s compared
to a superficial velocity of 4.9 mm/s especially when looking at the axial
velocity fluctuations.

In Figure 31 the PTV data for superficial gas velocities 3.2 mm/s and 6.6
mm/s are compared with interpolated PIV data.
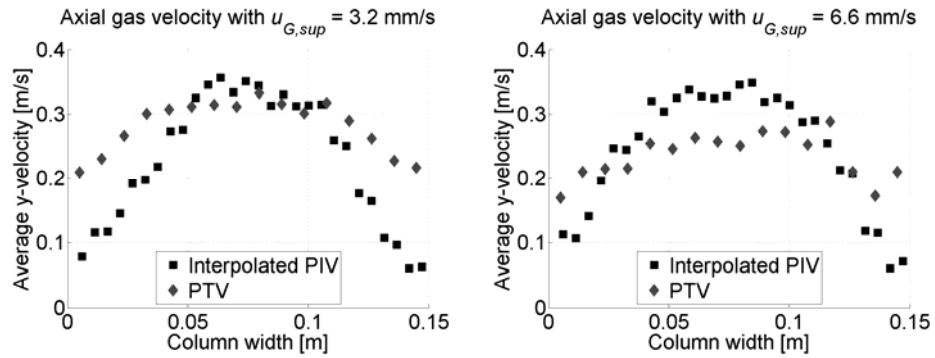
Figure 31   Comparison of time averaged PTV data and interpolated PIV data at a height of 0.25m and a depth of 0.075 m in the bubble column.

It is observed that core velocity and velocity toward the walls are lower and higher respectively when compared to the interpolated PIV data. This was expected when looking at Figure 26 and taking the findings by Deen (2001) and Dillerop (2000) into consideration.

2.7   Summary

In this chapter the bubble size distribution and bubble velocity in a square column has been experimentally measured by Interferometric Particle Imaging (IPI) and Particle Tracking Velocimetry (PTV) respectively. The experiment was done for three superficial gas velocities in one plane in the middle of the bubble column.

An introduction to IPI and PTV and a description of the experimental setup and post processing techniques have been presented.

The IPI results from the experiment have been presented in bubble diameter histograms, profile plots and tables and the PTV data has been presented as vector plots and profile plots along with a comparison with experimental and interpolated Particle Image Velocimetry (PIV) data from Deen (2001).

Bubble size

From the experimental IPI results it is found that the mean d_{10} and d_{32} are approximately 2.3mm and 6.0mm respectively. The mean diameter was observed visually to be approximately 5-6 mm, which is in excellent agreement with the measured value of d_{32}. When looking at bubble diameter histograms at different geometric locations in the bubble column it is not possible to distinguish between two arbitrarily selected bubble diameter histograms. They all show the same trend.

When looking at mean bubble diameter profiles in the axial direction in the bubble column it seems that the Sauter mean bubble diameter, d_{32}, is decreasing with increasing superficial gas velocity. The maximum d_{32} is however found in the middle for all three superficial gas velocities. This seems a little strange as an increasing, decreasing or even steady average d_{32} is expected axially.

The mean bubble diameter profiles in the radial direction show that the average d_{32} is smaller near the walls when compared to the average d_{32} at the axial centreline. This is also expected as large bubbles are migrating toward the middle or core region of the bubble column, whereas smaller bubbles migrate toward the wall according to the experimental observations by Tomiyama (2004). It is not evident here that d_{32} is decreasing with increasing superficial gas velocity.

Bubble velocity

The experimental PTV results are not in good agreement when compared to experimental PIV data from Deen (2001). The core velocity is too low and the velocity toward the walls is a bit too high. Also a wrong trend in the velocity is observed when compared to the discoveries by Dillerop (2000). When increasing the superficial gas velocity, the bubble velocities in the axial direction decrease significantly. It is believed that this is due to a too large time between bursts, which is essential for the quality of the PTV data. Furthermore a mirroring effect is believed to be present at two distinct locations in the field of view, which distorts the data, so that the data is unusable in the vicinity of those locations.

Deen (2001) performed a number of PIV experiments with different superficial gas velocities. The data from these are interpolated to obtain pseudo experimental PIV data at the two superficial gas velocities 3.2 mm/s and 6.6 mm/s. The axial gas and liquid velocity profiles at these superficial velocities are almost identical to the velocity profiles with a superficial gas velocity of 4.9 mm/s. A significant difference in the velocity profiles is however observed when looking at the axial and radial liquid velocity fluctuations.

Chapter 3

CFD for Multiphase Flow and Bubble Size Prediction

3.1   Introduction

In this chapter the theory behind CFD for multiphase flow is presented. Also the specific models for modelling the flow and bubble size in the bubble column are given.

3.2   Multiphase flow modelling

The models for solving multiphase flow can generally be divided into three classes:

- Interphase tracking models
- Eulerian-Lagrangian models
- Eulerian-Eulerian models

The interphase tracking models include among others level-set methods and Volume Of Fluid (VOF) methods. These methods accurately describe the interface between two phases, which is important for properly modelling for example the change in the shape of a rising bubble in quiescent liquid. The drawback is however that these methods require a high level of resolution both in grid and modelling in order to describe the interface properly, which requires large computational

efforts. These methods are therefore not suitable for solving dispersed bubbly flows.

The Eulerian-Lagrangian models are used for modelling dispersed flows. In this method the primary phase is treated as a continuum and the dispersed phase particle trajectories are tracked individually. This means that each particle has a velocity and very distinct properties, which allows for a detailed description of the flow of the individual particles. The drawback is that the computational effort increases as the total number of particles to be tracked increases. This method is therefore only suited for solving dilute flows.

The Eulerian-Eulerian models are used for modelling any type of multiphase flows. In this method all phases are treated as separate interpenetrating continua, and all equations with interaction terms are averaged and solved for each phase. This means this method is able to model large scale multiphase flows. The drawback is, however, that detailed modelling of the interphase interactions have to be supplied.

All the modelling in this thesis is done with the Eulerian-Eulerian approach, as this is regarded as being the most suitable method for modelling flow and bubble size distribution in the bubble columns.

3.3   Eulerian multiphase model[1]

As already mentioned, all phases in the Eulerian multiphase model are treated as separate interpenetrating continua. In bubble columns the water phase is treated as the continuous or primary phase and the air bubbles are regarded as the dispersed or secondary phase(s). The primary and secondary phases are characterized by volume fractions, which all per definition sum up to unity:

---

[1] The modelling in this chapter is based on Hansen *et al.* (2008).

$$\alpha_L + \sum_{q=1}^{N} \alpha_q = 1 \tag{5}$$

where α_L is the liquid volume fraction, α_q is the volume fraction of the qth gas phase and N is the total number of gas phases.

In the following, the fluid in each phase is assumed to be incompressible and isothermal. Therefore energy balances are not required. Also the interfacial mass transfer between the water and gas phase(s) is zero.

3.3.1 Governing equations

By conditionally ensemble averaging of the local instant conservation equations of single-phase flow, the governing equations of the multiphase model can be derived (Drew, 1983; Drew and Passman, 1999). The continuity equation for phase k is given by:

$$\frac{\partial}{\partial t}\left(\alpha_k \rho_k\right) + \nabla \cdot \left(\alpha_k \rho_k U_k\right) = 0 \tag{6}$$

where ρ_k and U_k are density and average velocity of phase k respectively. The momentum equation for phase k is given by:

$$\begin{aligned}\frac{\partial}{\partial t}\left(\alpha_k \rho_k U_k\right) + \nabla \cdot \left(\alpha_k \rho_k U_k U_k\right) = \\ -\nabla \cdot \left(\alpha_k \tau_k\right) - \alpha_k \nabla p + \alpha_k \rho_k g + M_{I,k}\end{aligned} \tag{7}$$

where p is the pressure shared for all phases, g is the gravity and $M_{I,k}$ is the interfacial momentum transfer for phase k. τ_k is the stress tensor for phase k, which is described with:

$$\tau_k = -\mu_{eff,k}\left(\nabla U_k + \left(\nabla U_k\right)^T - \frac{2}{3}I\left(\nabla U_k\right)\right) \tag{8}$$

where $\mu_{eff,k}$ is the effective viscosity of phase k and I is the unit tensor.

3.3.2   Interfacial forces

The interfacial momentum transfer from the gas phase to the liquid phase, $M_{I,k}$, accounts for drag, lift and virtual mass forces. The interfacial forces are calculated with the following:

$$M_{I,k} = M_{I,L} = -M_{I,G} = M_{D,L} + M_{L,L} + M_{VM,L} \tag{9}$$

where $M_{D,L}$ is the drag force, $M_{L,L}$ is the lift force and $M_{VM,L}$ is the virtual mass force. The drag force is given by:

$$M_{D,L} = -\frac{3}{4}\alpha_G \rho_L \frac{C_D}{d_B}|U_G - U_L|(U_G - U_L) \tag{10}$$

where C_D is the drag coefficient and d_B is the bubble diameter. The drag coefficient is modelled with the expression by Ishii and Zuber (1979) for distorted bubbles in water:

$$C_D = \frac{2}{3}\sqrt{E\ddot{o}} \tag{11}$$

where $E\ddot{o}$ is the dimensionless Eötvös number, given by:

$$E\ddot{o} = \frac{g(\rho_L - \rho_G)d_B^2}{\sigma} \tag{12}$$

The lift force is modelled with:

$$M_{L,L} = \alpha_G \rho_L C_L (U_G - U_L) \times \nabla \times U_L \tag{13}$$

where C_L is the lift coefficient, which is either set to a constant value of 0.5 as in the work by Deen (2001) or modelled with the relation by Tomiyama (2004)

$$C_L = min\left[0.288\,tanh(0.121\,Re_B), f(E\ddot{o}_d)\right] \tag{14}$$

where Re is the bubble Reynolds number given by:

$$Re_B = \frac{\rho_L u_r d_B}{\mu_L} \qquad (15)$$

where u_r is the slip velocity between the gas and liquid phase.

$Eö_d$ is the modified Eötvos number, given by:

$$Eö_d = \frac{Eö}{E^{\frac{2}{3}}} \qquad (16)$$

where E is the bubble aspect ratio. According to Wellek *et al.* (1966) it is given by:

$$E = \frac{1}{1 + 0.163 Eö^{0.757}} \qquad (17)$$

f(Eö$_d$) is given by:

$$f(Eö_d) = 0.00105 Eö_d^3 - 0.0159 Eö_d^2 - 0.0204 Eö_d + 0.474 \qquad (18)$$

The Tomiyama (2004) lift coefficient defined in Eq. 14 is plotted in Figure 32 versus bubble diameter.

The lift coefficient, C_L, is seen to change sign when $d_B > 0.0058$m. This is consistent with the observations by Tomiyama (2004), where large bubbles migrate toward the middle or core region of the flow (negative C_L), whereas smaller bubbles migrate toward the wall (positive C_L).

The virtual mass force is modelled with:

$$M_{VM,L} = \alpha_G \rho_L C_{VM} \left(\frac{DU_G}{Dt} - \frac{DU_L}{Dt} \right) \qquad (19)$$

where C_{VM} is the virtual mass constant with a value of 0.5. Here the *D/Dt* operators denote the substantial derivatives in the two phases (Deen, 2001).
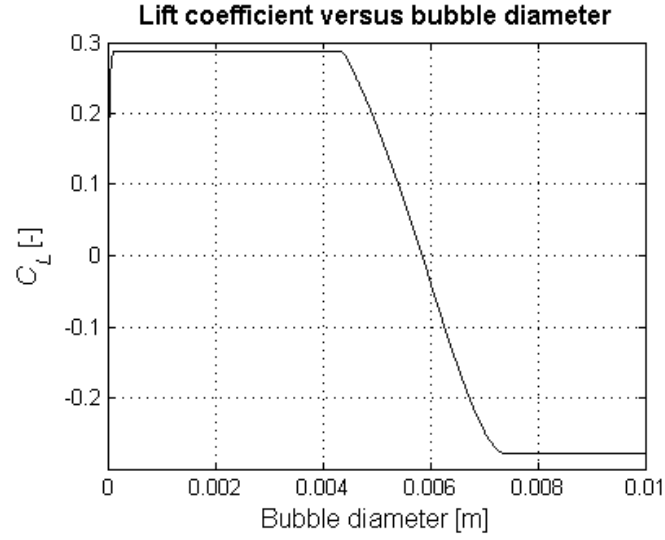
Figure 32   Tomiyama (2004) lift coefficient versus bubble diameter.

3.3.3   Turbulence modelling

The effective viscosity of the liquid phase is modelled with three contributions as in the work of Deen (2001):

$$\mu_{eff,L} = \mu_{Lam,L} + \mu_{t,L} + \mu_{BIT,L} \tag{20}$$

The shear-induced turbulent viscosity $\mu_{t,L}$ is modelled with the LES sub-grid approach proposed by Smagorinsky (1963):

$$\mu_{t,L} = \rho_L \left(C_S \Delta \right)^2 S \tag{21}$$

where C_S is the Smagorinsky coefficient with a value of 0.1 and Δ is the filter width, given by:

$$\Delta = \left(\Delta_x \Delta_y \Delta_z \right)^{1/3} \tag{22}$$

The characteristic filtered rate of strain, S, is given by:

$$|S| = (2S_L : S_L)^{1/2} \tag{23}$$

The bubble induced turbulence is modelled with the proposal from Sato and Sekoguchi (1975):

$$\mu_{BIT,L} = \alpha_G \rho_L C_{BIT} d_B |U_G - U_L| \tag{24}$$

where C_{BIT} is a model constant with a value of 0.6.

The effective gas phase viscosity is calculated from the effective liquid viscosity with the following relation proposed by Jacobsen *et al.* (1997):

$$\mu_{eff,G} = \frac{\rho_G}{\rho_L} \mu_{eff,L} \tag{25}$$

3.4   Bubble size prediction

In the present work the bubble size in the square bubble column is modelled with the One-Group Interfacial Area Concentration Equation (IACE).

3.4.1   Interfacial Area Concentration Equation (IACE)

Reyes (1989) proposed a population balance approach to develop a particle number density transport equation for chemically non-reacting, dispersed, spherical particles, or in this case bubbles. This model was then generalized for the purpose of interfacial area transport by Kocamustafaogullari and Ishii (1995), which lead to the following equation:

$$\frac{\partial f(\bar{x}, V_B, t)}{\partial t} + \nabla \cdot (f(\bar{x}, V_B, t) U_B) = \sum_j S_j(\bar{x}, V_B, t) + \sum_j S_{ph}(\bar{x}, V_B, t) \tag{26}$$

where $f(\bar{x}, V_B, t)$ is the bubble number density distribution function. This function specifies the probable number of bubbles at a given time t, in the

spatial range of $d\bar{x}$ about a position $\bar{x}$, with bubble volumes between V_B and $V_B + dV_B$. $f(\bar{x}, V_B, t)U_B$ is the local time-average velocity of the bubbles, S_{ph} represents the bubble source/sink rate due to phase change and S_j represents the net change of the bubble number density distribution function due to bubble coalescence or breakup. (Wu *et al.*, 1998)

The above equation is however too complicated to use in fluid dynamics because of dependence on the bubble volume. Therefore the integral form of the bubble number density transport equation is used instead:

$$\frac{\partial n(\bar{x},t)}{\partial t} + \nabla \cdot \left(n(\bar{x},t)U_{Bm}(\bar{x},t) \right) = \sum_j S_{n,j}(\bar{x},t) + \sum_j S_{n,ph}(\bar{x},t) \qquad (27)$$

where $n(x,t)$ is the number density of bubbles of all sizes, $U_{Bm}(\bar{x},t)$ is the average local bubble velocity weighed by the bubble number and $S_{n,j}$ and $S_{n,ph}$ are the total bubble number source/sink rate per unit mixture volume (Wu *et al.*, 1998).

The bubble number density, n, has the following geometric relation:

$$n = \frac{\alpha_G}{V_B} = \psi\left(\frac{a_i^3}{\alpha_G^2} \right) \qquad (28)$$

where ψ is a bubble shape factor. For spherical bubbles ψ equals $1/(36\pi)$ and V_B is the average bubble volume. This geometric relation is then used to modify the integral form of the bubble number density transport equation into the one-group interfacial area concentration transport equation:

$$\frac{\partial a_i}{\partial t} + \nabla \cdot \left(a_i U_{i,B} \right) = \frac{1}{3\psi}\left(\frac{\alpha_G}{a_i} \right)^2 \left[\sum_j S_{n,j} + \sum_j S_{n,ph} \right]$$
$$+ \left(\frac{2a_i}{3\alpha_G} \right)\left[\frac{\partial \alpha_G}{\partial t} + \nabla \cdot \left(U_{i,B}\alpha_G \right) \right] \qquad (29)$$

Here the interfacial area concentration a_i is defined as total surface of the dispersed fluid particles per unit mixture volume. $S_{n,j}$ is the source/sink rate for the interfacial area due to coalescence and breakup, $S_{n,ph}$ is the source/sink rate for the interfacial area due to phase change. The second term on the right hand side represents the effects of the variation in bubble volume (Wu *et al.*, 1998).

If the gas phase is considered incompressible without phase change, the IACE transport equation is reduced to:

$$\frac{\partial a_i}{\partial t} + \nabla \cdot \left(a_i U_{i,B} \right) = \frac{1}{3\psi} \left(\frac{\alpha_G}{a_i} \right)^2 \sum_j S_{n,j} \tag{30}$$

The closure, $S_{n,j}$ can be modelled in different ways. Two different closure approaches have been used in the present work. These are presented in the following.

Closure approach by Wu *et al.*

The first approach to model the closure in the IACE transport equation is adopted from the work of Wu *et al.* (1998). The kernels have been developed for one dimensional bubbly flows in vertical round pipes relevant for nuclear engineering. Here the interfacial area and $\sum_j S_{n,j}$ is modelled with the following expression.

$$\frac{\partial a_i}{\partial t} + \nabla \cdot \left(a_i u_{i,B} \right) = \frac{1}{3\psi} \left(\frac{\alpha}{a_i} \right)^2 \left(-S_{n,RC} - S_{n,WE} + S_{n,TI} \right)$$
$$= S_{a,RC} + S_{a,WE} + S_{a,TI} \tag{31}$$

The source terms $S_{a,RC}$, $S_{a,WE}$ and $S_{a,TI}$ are the net rates of change of interfacial area per unit mixture volume, and these three mechanisms are considered to be dominant in one dimensional vertical two-phase bubbly flow (Wu *et al.*, 1998).

$S_{a,RC}$ represents bubble coalescence from random collisions due to turbulence and is given by:

$$S_{a,RC} = -\frac{1}{3\pi} C_{RC} \left(u_f a_i\right)^2 \left[\frac{1}{\alpha_{max}^{1/3}\left(\alpha_{max}^{1/3} - \alpha^{1/3}\right)}\right]$$
$$\cdot \left[1 - exp\left(-C\frac{\alpha_{max}^{1/3}\alpha^{1/3}}{\alpha_{max}^{1/3} - \alpha^{1/3}}\right)\right] \tag{32}$$

where C_{RC} and C are model constants and u_f is the root mean square velocity between two particular bubbles. It is calculated from (Delhaye, 2001):

$$u_f = \varepsilon^{1/3} d_B^{1/3} \tag{33}$$

The turbulent dissipation rate, ε, is approximated with the following relation as proposed by Pope (2000):

$$\varepsilon = \frac{\mu_{eff,L}^3}{\rho_L^3 \left(C_S \Delta\right)^4} \tag{34}$$

where $\mu_{eff,L}$ is the effective dynamic viscosity of the liquid, ρ_L is the liquid density, C_S is the Smagorinsky coefficient and Δ is the filter width.

$S_{a,WE}$ represents bubble coalescence from the wake entrainment process due to relative motions of the bubbles and is given by:

$$S_{a,WE} = -\frac{1}{3\pi} C_{WE} a_i^2 u_{rw} \tag{35}$$

where C_{WE} is a model constant and u_{rw} is the relative velocity averaged over the wake length, which is given by (Delhaye, 2001):

$$u_{rw} = u_r C_d^{1/3} \tag{36}$$

u_r is in turn given by the Ishii-Chawla correlation (Ishii and Chawla, 1979):

$$u_r = \sqrt{\frac{d_B g}{3 C_D} \cdot \frac{\rho_L - \rho_G}{\rho_L}} \tag{37}$$

with the drag coefficient given by:

$$C_D = \frac{24}{Re}\left(1 + 0.1\,Re^{3/4}\right) \tag{38}$$

and *Re* given by:

$$Re = \frac{\rho_L u_r d_B}{\mu_L} \tag{39}$$

$S_{a,TI}$ represents bubble breakup caused by the impact of turbulent eddies and is given by:

$$S_{a,TI} = -\frac{1}{18} C_{TI} u_f \left(\frac{a_i^2}{\alpha}\right)\sqrt{1 - \frac{We_{cr}}{We}} \cdot exp\left(-\frac{We_{cr}}{We}\right), We > We_{cr} \tag{40}$$

where C_{TI} and We_{cr} are model constants and the dimensionless Weber number, *We*, is given by:

$$We = \frac{\rho_L d_B^{5/3} \varepsilon^{2/3}}{\sigma} = \frac{\rho_L u_f^2 d_B}{\sigma} \tag{41}$$

The model constants for this approach are taken from Ishii & Kim (2001): $C_{RC} = 0.004$, $C = 3.0$, $C_{WE} = 0.002$, $C_{TI} = 0.085$, $\alpha_{max} = 0.75$ and $We_{cr} = 6.0$.

Closure approach by Moilanen *et al.*

The second closure approach to model the coalescence/breakup processes is adopted from the work of Moilanen *et al.* (2008). The kernels have been developed for gas-liquid flow in stirred tanks, and are based on the

work by Lane *et al.* (2005). Here the interfacial area and $\sum_j S_{n,j}$ is modelled with the following expression:

$$\frac{\partial a_i}{\partial t} + \nabla \cdot \left(a_i u_{i,B} \right) = \frac{1}{3\psi} \left(\frac{\alpha}{a_i} \right)^2 \left(S_{n,BR} - S_{n,CO} \right) = S_{a,BR} - S_{a,CO} \qquad (42)$$

$S_{a,CO}$ represents the bubble coalescence source term, and is modelled with the following relation:

$$S_{a,CO} = C_{CO} \left(1 - \alpha \right) \eta_{CO} \varepsilon^{1/3} d_B^{7/3} \qquad (43)$$

where the coalescence efficiency, η_{CO}, is modelled with:

$$\eta_{CO} = exp\left(-\sqrt{\frac{We}{8}} \right) \qquad (44)$$

$S_{a,BR}$ represents the bubble breakup sink term, and is modelled with the following relation:

$$S_{a,BR} = C_{BR} \left(1 - \alpha \right) \left(\frac{\varepsilon}{d_B^2} \right)^{1/3} exp\left(\frac{We_{cr}}{We} \right), We > We_{cr} \qquad (45)$$

For both coalescence and breakup, the turbulent dissipation rate, ε, and the Weber number are calculated with Eqs. 34 and 41 respectively. The model constants for this approach are taken from Moilanen *et al.* (2008): $We_{cr} = 1.5$, $C_{CO} = 0.05$ and $C_{BR} = 0.075$.

Bubble diameter

The resulting Sauter mean bubble diameter is then given by:

$$d_{32,B} = \frac{6\alpha_G}{a_i} \qquad (46)$$

Chapter 4

Numerical Simulations of Flow in the Square Bubble Column

4.1 Introduction

In this chapter the numerical simulations of the flow pattern in the square bubble column are presented. Numerical simulations have already been done on the flow pattern in the bubble column by Deen (2001). These simulations were compared with experimental data, and excellent agreement between experiments and simulations was found (Deen, 2001). The purpose of repeating the simulations is to validate the flow model from chapter 3.3, as this flow model forms the basis for all the remaining simulations in this thesis. Also Deen (2001) performed simulations in CFX-4.3, whereas the simulations in this thesis are done in Fluent 6.3.

The simulations with the flow model will be compared with a selected CFX-4.3 simulation by Deen (2001) and the PIV experiments by Deen (2001).

4.2 Simulation settings

In this section the simulation settings for the flow pattern simulations are presented.

4.2.1   Grid and boundary conditions

The grid used in the simulations is a 0.15m x 0.45m x 0.15m square volume meshed with hexahedral cells. The number of cells in the x-, y- and z-direction for case 1 is 32, 45 and 32 respectively, which gives a total of 46080 hexahedral cells. The grid is the same as used by Deen (2001). The geometry with and without mesh can be seen in Figure 33.
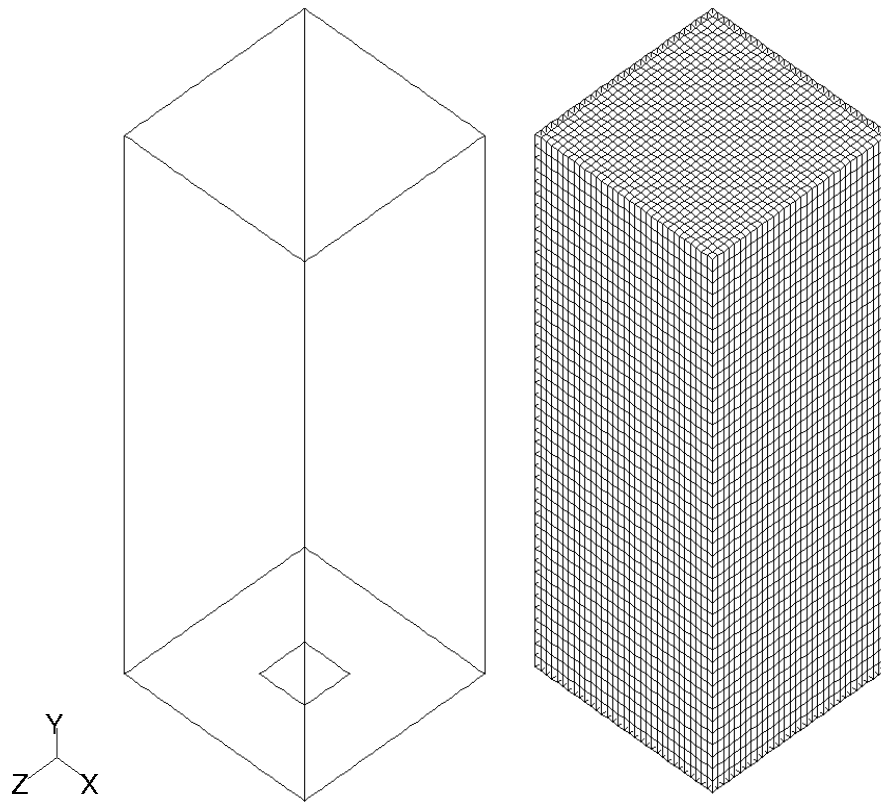

Figure 33   Geometry of the square bubble column with and without mesh.

The inlet of the bubble column is a perforated distributor plate, which has 7 x 7 (49) holes with a diameter of 1mm and a pitch length of 6.75mm. The inlet can either be modelled as a fully open inlet as in the work of Deen (2001) or as a perforated plate like in the work of Bove (2005). Both inlet approaches are tested in this chapter.

Deen inlet

The inlet boundary condition is modelled as a velocity inlet in Fluent 6.3, where the velocity and volume fraction of the fluid are to be specified. The inlet is modelled with 8x8 cells, which gives an inlet area A_{inlet} of 0.0375 x 0.0375m^2. With a superficial gas velocity of 4.9mm/s, the inlet velocity normal to the inlet will be 0.0784m/s with a gas volume fraction of unity. The diameter of gas bubbles is set to 4mm as in the work by Deen (2001).

Bove inlet

Again the inlet boundary condition is modelled as a velocity inlet with 8x8 cells, an inlet area of 0.0375 x 0.0375m^2 and a superficial gas velocity of 4.9mm/s. The diameter of gas bubbles is set to 4mm. The inlet is modelled as a perforated plate. The porosity of the plate is:

$$P = \frac{A_{holes}}{A_{inlet}} = 2.74\% \tag{47}$$

The gas volume fraction $\alpha_{G,inlet}$ is set equal to the porosity P in order to simulate the effect of the perforated distributor plate. The inlet velocity then becomes:

$$u_{in,Bove} = \frac{u_{in,Deen}}{P} = \frac{u_{in,Deen}}{\alpha_{G,inlet}} = 2.86\,\frac{m}{s} \tag{48}$$

Outlet and walls

The outlet is modelled as a pressure outlet in Fluent 6.3, where the air backflow volume fraction is specified to be zero and the walls are modelled as no-slip boundaries for both phases.

4.2.2   Other settings

The simulations are 1st order implicit transient in three dimensions. The time step size is set to 0.005s, and the simulation time is set to 200s with averaging done on the last 150s. Third order spatial discretisation schemes are employed (QUICK). This is done in order to compare with Deen's results. A simulation was typically run on 3 AMD Athlon XP 1.4 GHz nodes and took approximately 8 days.

4.3   Results

In this section the results of the simulations will be presented. The results are compared with the experimental data from Deen (2001) and the simulations by Deen (2001).

This section is divided into two parts. In the first part, the simulations with the Deen inlet conditions ($\alpha_{G,inlet} = 1$) are presented. In the second part the simulations with the Bove inlet ($\alpha_{G,inlet} \neq 1$) are presented.

4.3.1   Deen inlet condition

The simulations with the Deen inlet condition are done in order to compare the results from Fluent 6.3 with the results from Deen (2001), who used CFX-4.3. Simulations with different interfacial forces settings and with or without BIT are run. All simulations are run with the drag model by Ishii & Zuber (1979) and the LES sub-grid approach proposed by Smagorinsky (1963).

Interfacial forces

In the work by Deen (2001) a plot of the different interfacial forces was presented. An exact replica of this can be seen in Figure 34.
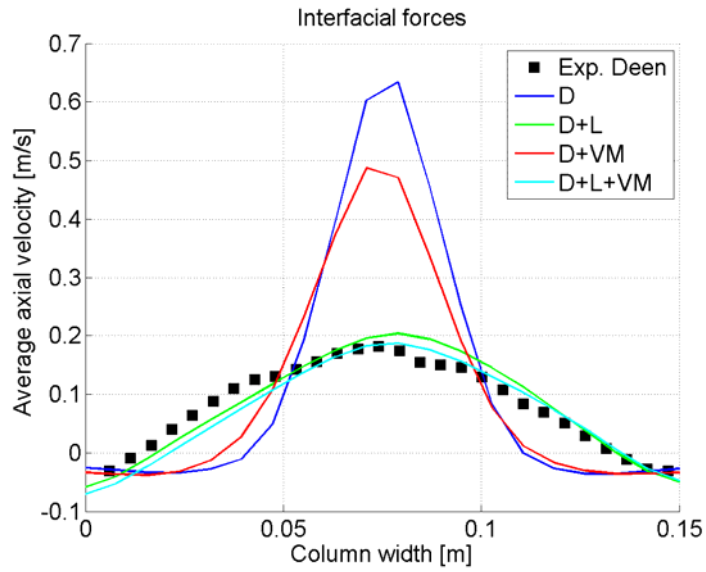
Figure 34 Profiles of time averaged simulated and measured axial liquid velocity for different interfacial forces, at a height of 0.25m and a depth of 0.075m. D: drag force, L: lift force, VM: virtual mass force (from Deen, 2001).

Evidently the lift force is an important interfacial force for capturing the liquid velocity profile.

Drag force only

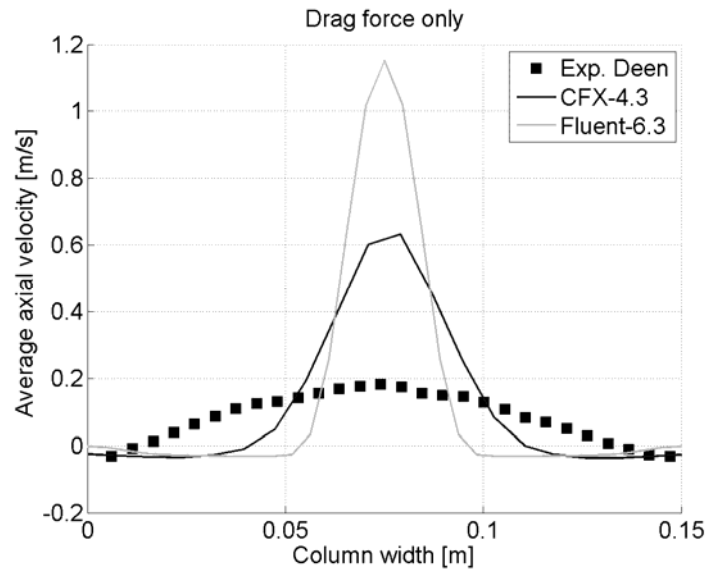A simulation with drag as the only interfacial force has been run in Fluent 6.3, and the result is shown in Figure 35.

Figure 35 Profiles of time averaged simulated and measured axial liquid velocity at a height of y = 0.25m and a depth of z = 0.075m. Drag force is the only interfacial force employed. Experimental data is from Deen (2001).

It is evident that the drag force alone is not able to capture the liquid velocity profile. The bubble plume is not fluctuating radially, when only using drag to describe the interfacial forces, as can be seen in Figure 36. In the following, the lift force is therefore always included in the simulations.
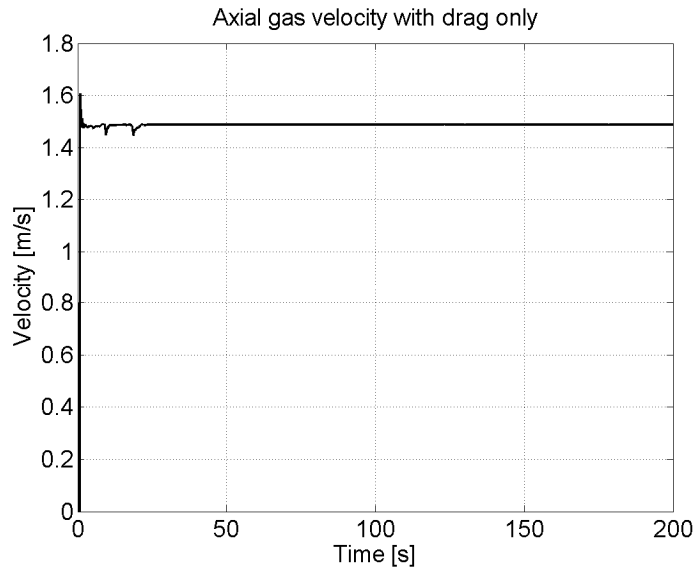
Figure 36   Axial gas velocity versus time in a point in the bubble column at a height of 0.25m, a depth of 0.075m and a width of 0.075m. Drag force is the only interfacial force employed.

Parameter study with different interfacial forces

In Table 5 the different interfacial forces simulations are listed.

Table 5   Overview of Deen inlet simulations

Case	Δt	M_I	μ_{eff}
D-D+L	0.005	Drag, lift	LES, BIT
D-D+TL	0.005	Drag, Tomiyama lift	LES, BIT
D-D+L+VM	0.005	Drag, lift, virtual mass	LES, BIT
D-D+L-BIT	0.005	Drag, lift	LES
D-D+L+VM-BIT	0.005	Drag, lift, virtual mass	LES

Before comparing the simulations in Table 5, a few plots of the flow pattern in the bubble column are presented.

In Figure 37 instantaneous water velocity vectors coloured by axial velocity are shown.
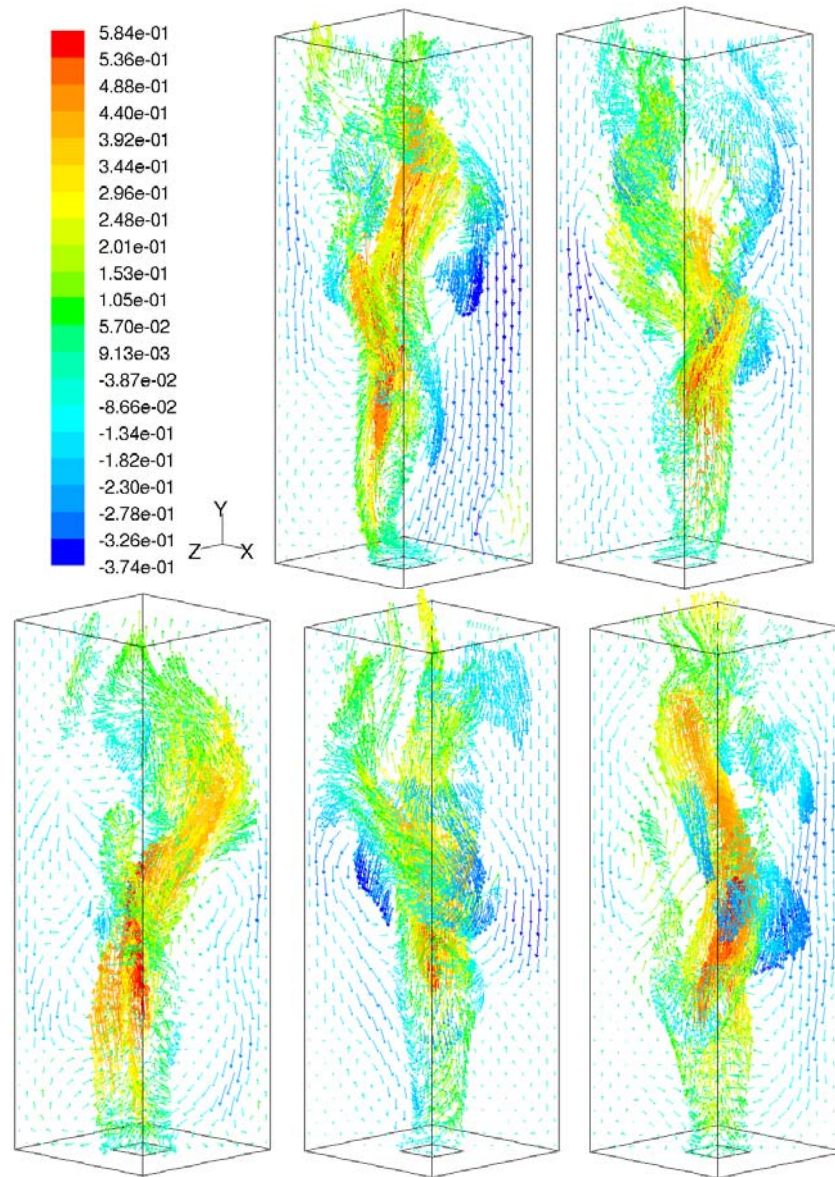
Figure 37 Instantaneous velocity vectors of water coloured with magnitude of axial velocity at 10s intervals from 160s to 200s. The vectors are plotted in a diagonal cut plane and an iso-surface of $\alpha_G = 0.04$. Case D-D+L.

In Figure 38, a time series of contour plots showing instantaneous gas volume fraction in a diagonal cut plane is shown.
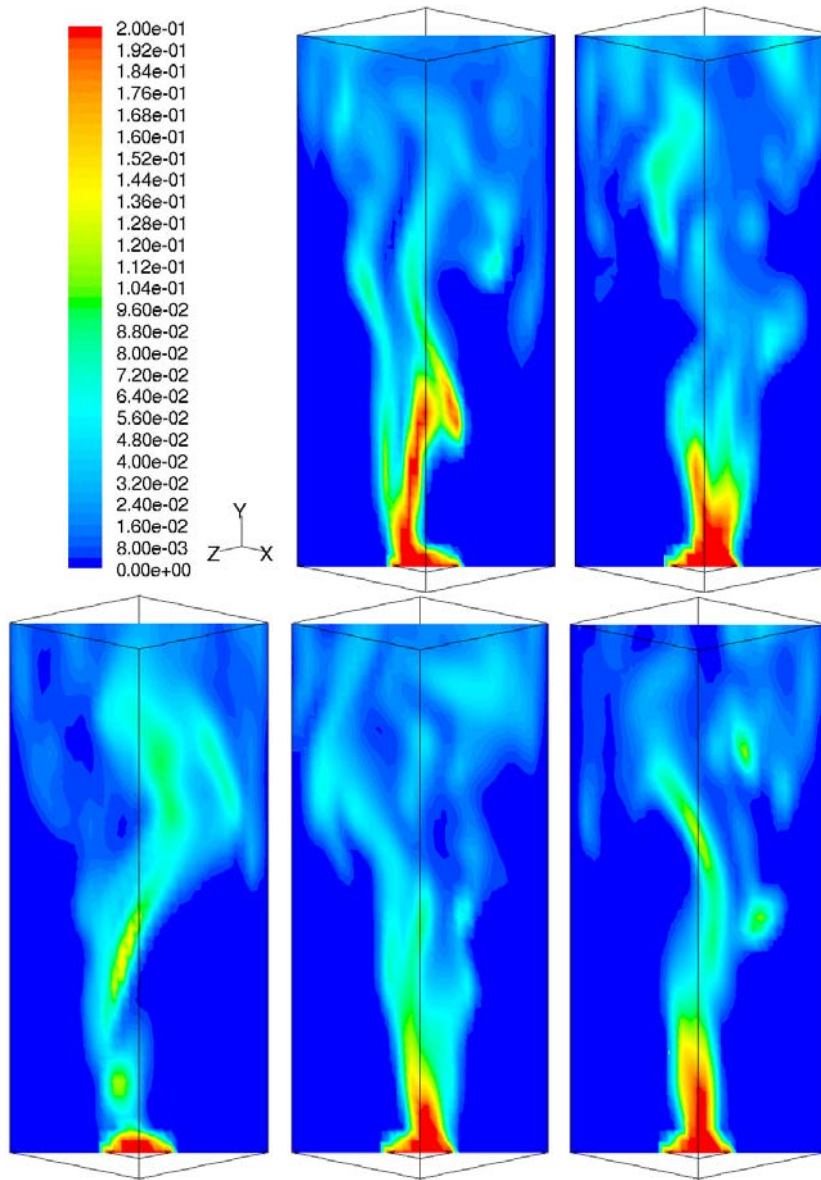
Figure 38 Contour plots of the instantaneous volume fraction of gas in a diagonal cut plane at 10s intervals from 160s to 200s. Case D-D+L.

Figure 37 and Figure 38 show that the bubble plume fluctuates in the radial direction. The added lift force is responsible for this. This fluctuating behaviour was also observed during the experiments. Figure

39 shows a time series of the simulated axial gas velocity in a point in the middle of the bubble column at a height of 0.25m.
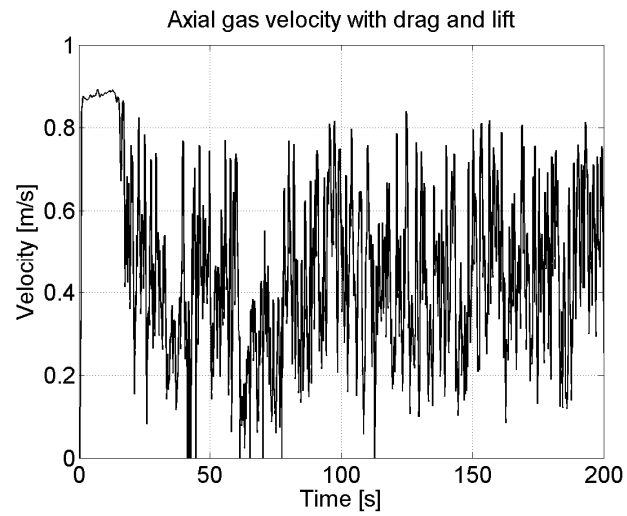
Figure 39   Axial gas velocity versus time for case D-D+L at a height of 0.25m, a depth of 0.075m and a width of 0.075m.

In Figure 40 a FFT of the axial gas velocity is presented.
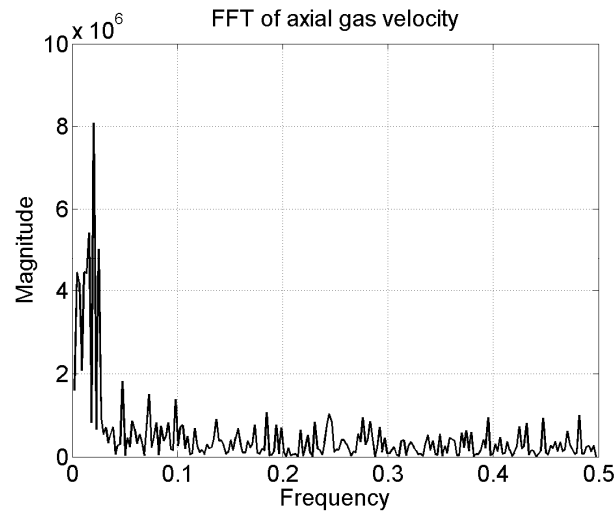
Figure 40   FFT of axial gas velocity history for case D-D+L at a height of 0.25m, a depth of 0.075m and a width of 0.075m.

The highest magnitude of the signals corresponds to a frequency of 0.0206 Hz or a period of 48.5 seconds. This period must be large scale fluctuations that cannot be determined from looking at Figure 39.

Profiles of time averaged axial liquid velocity are shown in Figure 41 for the simulations in Table 5. Also the experimental PIV data and a simulation from Deen (2001) are included.
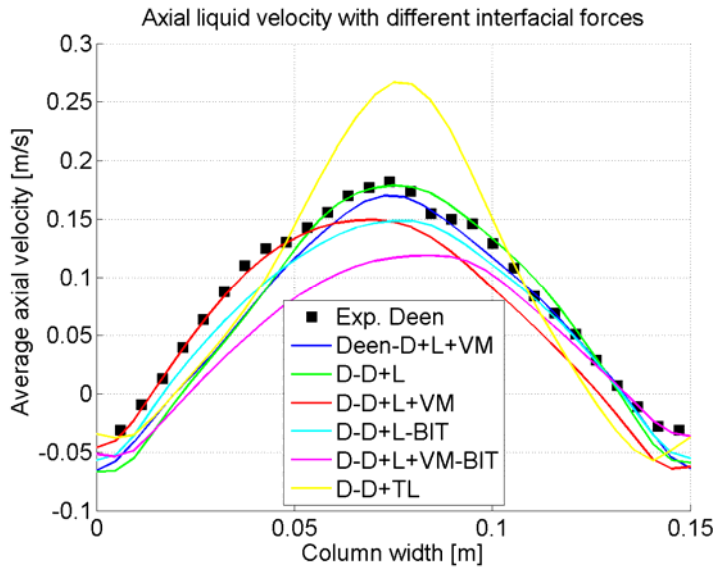
Figure 41   Profiles of time averaged simulated and measured axial liquid velocity for different interfacial forces, at a height of 0.25m and a depth of 0.075m. Experimental data and Deen-D+L+VM simulation data is from Deen (2001).

From Figure 41 it is evident that the core velocity is simulated satisfactorily with drag and lift force ($C_L = 0.5$). Addition of virtual mass force and removal of BIT lowers the core velocity prediction. The addition of the Tomiyama lift coefficient results in a severe over prediction of the core velocity.

Profiles of time averaged axial gas velocity are shown in Figure 42 for the simulations in Table 5. Also the experimental data and a simulation from Deen (2001) are included.
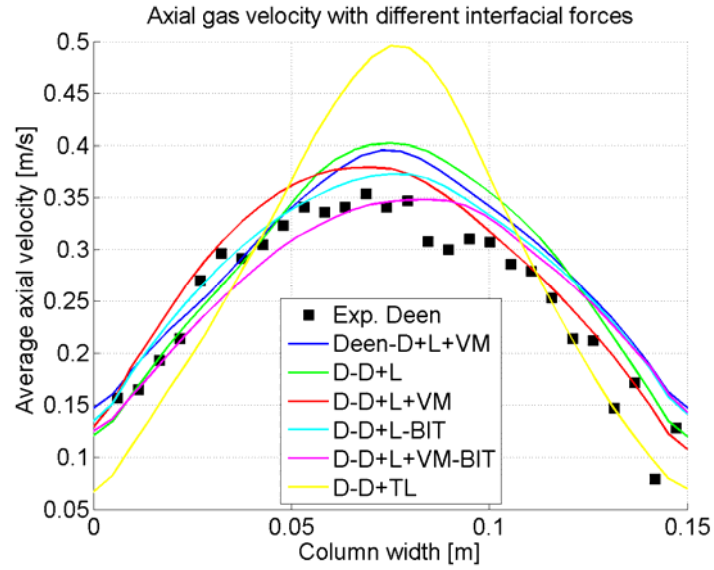
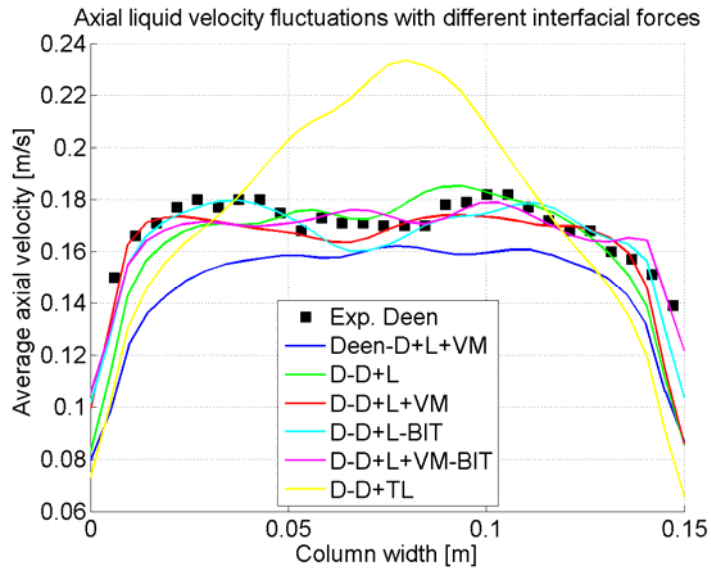*Figure 42   Profiles of time averaged simulated and measured axial gas velocity for different interfacial forces, at a height of 0.25m and a depth of 0.075m. Experimental data and Deen-D+L+VM simulation data is from Deen (2001).*

From Figure 42 it is evident that the core velocity is simulated satisfactorily with drag, lift force ($C_L = 0.5$), virtual mass force and no BIT. All other cases over predict the core velocity. Again the addition of the Tomiyama lift coefficient results in a severe over prediction of the core velocity.

Profiles of time averaged axial liquid velocity fluctuations are shown in Figure 43 for the simulations in Table 5. Also the experimental data and a simulation from Deen (2001) are included.
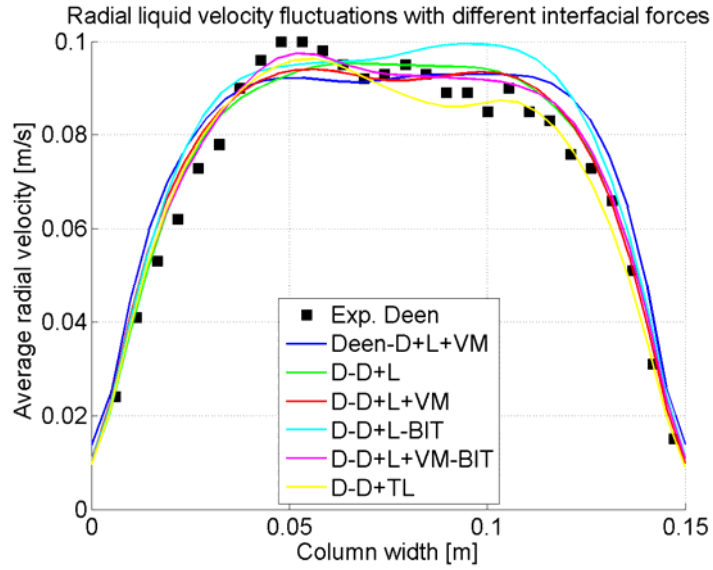
Figure 43 Simulated and measured profiles of axial liquid velocity fluctuations for different interfacial forces, at a height of 0.25m and a depth of 0.075m. Experimental data and Deen-D+L+VM simulation data is from Deen (2001).

From Figure 43 it is observed that all the different cases capture the fluctuations satisfactorily except for case D-D+TL.

Profiles of time averaged radial liquid velocity fluctuations are shown in Figure 44 for the simulations in Table 5. Also the experimental data and a simulation from Deen (2001) are included.
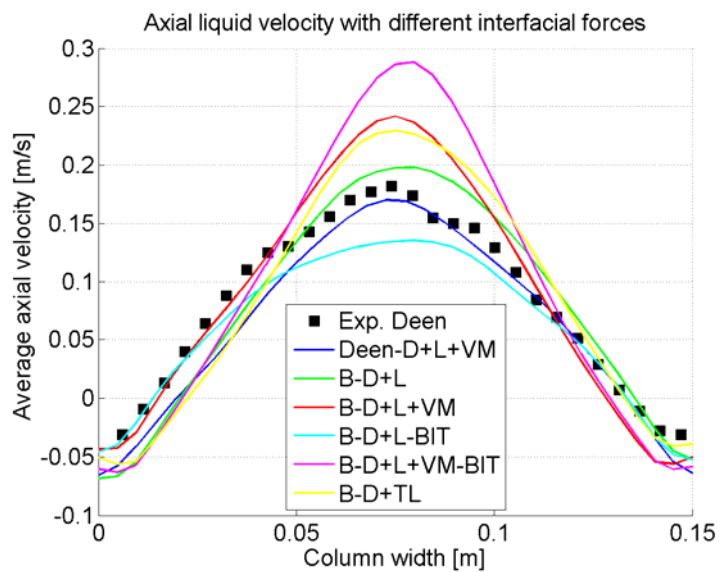
Figure 44 Profiles of time averaged simulated and measured radial liquid velocity fluctuations for different interfacial forces, at a height of 0.25m and a depth of 0.075m. Experimental data and Deen-D+L+VM simulation data is from Deen (2001).

From Figure 44 it is observed that all cases show very good agreement with the experimental data.

4.3.2   Bove inlet condition

The simulations with the Bove inlet condition are run because of the need to use an inlet with $\alpha_{G,inlet} \neq 1$ for the bubble size prediction simulations later in this thesis. The simulations will be compared with the results from Deen (2001). As in the latter chapter, simulations with different interfacial forces settings and with or without BIT are run. Again all simulations are run with the drag model by Ishii & Zuber (1979) and the LES sub-grid approach proposed by Smagorinsky (1963).

In Table 6 the simulations with different interfacial forces are listed.

Table 6   Overview of Bove inlet simulations

Name	Δt	M_I	μ_{eff}
B-D+L	0.005	Drag, lift	LES, BIT
B-D+TL	0.005	Drag, Tomiyama lift	LES, BIT
B-D+L+VM	0.005	Drag, lift, virtual mass	LES, BIT
B-D+L-BIT	0.005	Drag, lift	LES
B-D+L+VM-BIT	0.005	Drag, lift, virtual mass	LES

Profiles of time averaged axial liquid velocity are shown in Figure 45 for the simulations in Table 6. Also the experimental data and a simulation from Deen (2001) are included.

Figure 45   Simulated and measured axial liquid velocity profiles for different interfacial forces, at a height of 0.25m and a depth of 0.075m. Experimental data and Deen-D+L+VM simulation data is from Deen (2001).

Figure 45 shows that case B-D+L is closest to the experimental data. The interesting thing here is however that added virtual mass force results in severe over prediction of the core velocity. This was exactly the opposite for the Deen inlet simulations, where added virtual mass force resulted in severe under prediction of the core velocity.

In Figure 46, profiles of time averaged axial gas velocity are shown for the cases in Table 6. Furthermore the experimental data and a simulation from Deen (2001) are included for comparison.
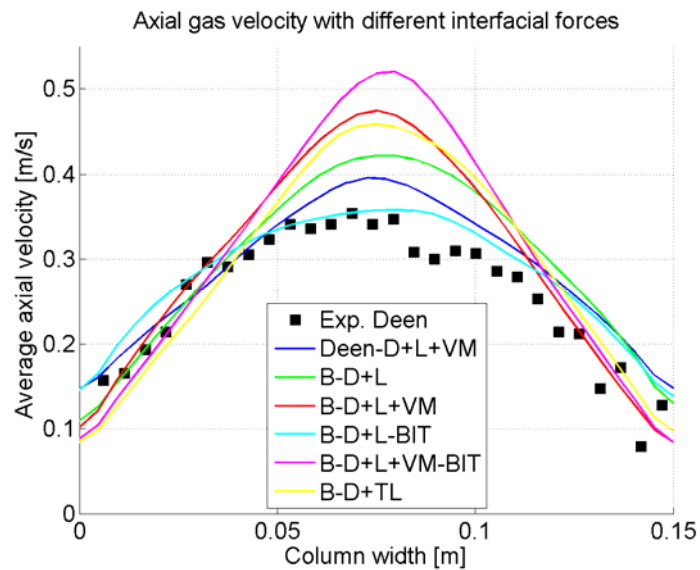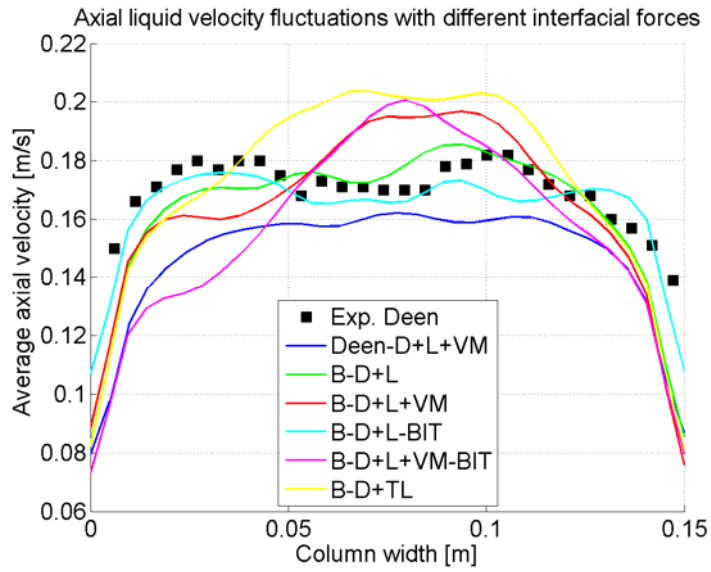

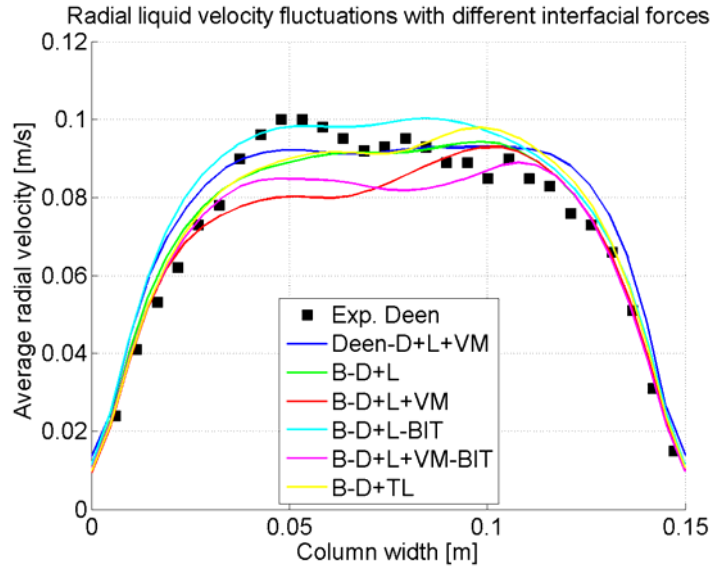*Figure 46   Profiles of time averaged simulated and measured axial gas velocity for different interfacial forces, at a height of 0.25m and a depth of 0.075m. Experimental data and Deen-D+L+VM simulation data is from Deen (2001).*

From Figure 46 it is evident that case B-D+L-BIT is predicting the gas velocity satisfactorily. All other cases over predict the core velocity quite severely. Again the added virtual mass force results in the most severe over prediction.

Profiles of time averaged axial liquid velocity fluctuations are shown in Figure 47 for the simulations in Table 6. Also the experimental data and a simulation from Deen (2001) are included.

*Figure 47   Profiles of time averaged simulated and experimental axial
liquid velocity fluctuations for different interfacial forces, at
a height of 0.25m and a depth of 0.075m. Experimental data
and Deen-D+L+VM simulation data is from Deen (2001).*

It is evident from Figure 47 that the cases B-D+L and D-D+L-BIT
capture the axial liquid fluctuations satisfactorily. All other cases show
too high core fluctuations

In Figure 48 profiles of time averaged radial liquid velocity fluctuations
are shown for the cases in Table 6. Furthermore the experimental data
and a simulation from Deen (2001) are included for comparison.

Figure 48   Simulated and measured profiles of radial liquid velocity fluctuations for different interfacial forces, at a height of 0.25m and a depth of 0.075m. Experimental data and Deen-D+L+VM simulation data is from Deen (2001).

From Figure 48 it is observed the added virtual mass cases under predict the radial liquid velocity fluctuations a bit. All other cases show excellent agreement with the experimental data.

4.4   Summary

In this chapter the flow pattern in the bubble column has been modelled with different interfacial forces along with two different inlet boundary conditions.

It has been shown that the flow pattern in the bubble column can be modelled satisfactorily with the distorted drag model by Ishii & Zuber (1979), LES sub-grid approach as proposed by Smagorinsky (1963), a constant lift force with $C_L = 0.5$ and bubble induced turbulence (BIT) as proposed by Sato and Sekoguchi (1975). The added virtual mass force and especially the Tomiyama lift coefficient (Tomiyama, 2004) failed to

predict the flow pattern satisfactorily for both inlet boundary conditions, especially the core velocity was either severely under- or over predicted. In the work of Zhang (2007) the same problem with the Tomiyama lift coefficient was observed in the square bubble column.

When looking ahead in this thesis, the results from the Deen inlet simulations are not that interesting, as the inlet boundary condition for the coming bubble size predictions demand that $\alpha_{G,inlet} \neq 1$. The Deen inlet simulations were included in this thesis to show that it was possible to reproduce the simulations by Deen (2001) in Fluent 6.3.

The Bove inlet simulations are however essential for the further work in this thesis, as they form a basis for the bubble size predictions in the next chapter. It has been shown in this chapter that the choice of interfacial forces and turbulence model is essential for correct prediction of the flow pattern in the bubble column.

On the basis of the observations done in this chapter, it is concluded that case B-D+L-BIT should form the base case for bubble size predictions, as this case captures the axial gas velocity and the liquid fluctuations satisfactorily in the bubble column when comparing with the experimental data by Deen (2001).

It should be noted that Zhang (2007) reported the following:

"Recent Front Tracking results by Dijkhuizen et al. (2007) reveals that the lift coefficient also depends on the shear rate in the liquid phase, which may vary as a function of applied column geometry"

This could explain why simulations the Tomiyama lift coefficient is not predicting the velocity profile satisfactorily. However a varying bubble size will probably have some effect on the flow pattern. The Tomiyama lift coefficient should therefore not be ignored as it is sensitive to bubble size. Also the viscosity will change with varying bubble diameter when employing BIT.

Chapter 5

Numerical Simulations of Bubble Size in the Square Bubble Column with the IACE Model

5.1 Introduction

In this chapter, numerical simulations of bubble size in the square bubble column are presented for three superficial gas velocities. The bubble size is calculated with the interfacial area concentration equation (IACE) presented in Chapter 3.4. Two different kernels for coalescence and breakup are used in the simulations, which gives a total of six different base case simulations.

In the first part of this chapter the simulation settings for the six base case simulations are presented.

In the second part of this chapter the results from two base case simulations with a superficial velocity of 4.9 mm/s are presented. The cases are set up with the recommendations from Chapter 4 and the two different IACE closure approaches presented in Chapter 3.4.

In the third part of this chapter the results from the remaining four base case simulations are presented.

In the last part of this chapter a parameter study on the six base cases are presented.

All simulations are compared with experimental IPI data, PIV data by Deen (2001) and interpolated PIV data from Chapter 2.6.

5.2   Simulation settings

In this section the simulation settings for the six base case bubble size simulations on the square bubble column with the IACE model are presented.

5.2.1   Grid and boundary conditions

The grid used in the simulations is a 0.15m x 0.45m x 0.15m square volume meshed with hexahedral cells. The number of cells in the x-, y- and z-direction are 32, 45 and 32 respectively, which gives a total of 46080 hexahedral cells. The geometry with and without mesh can be seen in Figure 33.

Inlet

The inlet of the bubble column is modelled as a velocity inlet with 8 x 8 cells, an area of 0.0375 x 0.0375m^2 at superficial gas velocities of 3.2, 4.9 and 6.6mm/s like in the work of Bove (2005). α_G is set to 0.0274.

The initial diameter of the bubbles is to be determined. In an article by Bhavaraju (1978), a number of different calculation methods have been found. A relation by Davidson & Schuler (1960) suggests the following:

$$d_B = 1.11 \frac{Q_{G,o}^{2/5}}{g^{1/5}}, \; Q_{G,o} < 3 \cdot 10^{-6} \frac{m^3}{s} \tag{49}$$

Where $Q_{G,o}$ is the gas rate per orifice. With a superficial gas velocity of 4.9mm/s, the gas rate per orifice becomes 2.25e-6m^3/s, and d_B is 3.9mm.

A different approach is given by Bhavaraju (1978):

$$d_B = 3.23\, Re_{L,o}^{-0.1}\, Fr_o^{0.21}\, d_o \qquad (50)$$

where $Re_{L,o}$ is the orifice liquid Reynolds number:

$$Re_{L,o} = \frac{4\rho_L Q_{G,o}}{\pi d_o \mu_L} \qquad (51)$$

and Fr_o is the orifice Froude number:

$$Fr_o = \frac{Q_{G,o}^2}{d_o^5 g} \qquad (52)$$

With a superficial gas velocity of 4.9 mm/s, the gas rate per orifice becomes 2.25e-6 m^3/s, $Re_{L,o}$ is 2853, Fr_o equals 516 and d_B is 5.4mm.

As the bubble column is designed with the purpose of yielding 4mm bubbles (Deen, 2001), it is chosen to set the inlet bubble size to 4mm in the base case simulations.

Outlet and walls

The outlet is modelled as a pressure outlet in Fluent 6.3, where the air backflow volume fraction is zero. The walls are modelled as no-slip boundaries for both phases.

5.2.2   Turbulence modelling

All simulations are run with the LES sub-grid approach proposed by Smagorinsky (1963). In Chapter 4.4 it was concluded that BIT should not be included when modelling the flow in the square bubble column. However since BIT will introduce a change in the contribution to the viscosity with varying bubble size, BIT should be tested.

5.2.3   Interface models

In Chapter 4.4 it was concluded that case D_D+L-BIT was the better choice when modelling the flow in the square bubble column. Therefore the following interfacial forces are included in the base case: distorted bubble drag model by Ishii & Zuber (1979), constant lift ($C_L = 0.5$) and no added virtual mass. It should be noted that since the lift coefficient proposed by Tomiyama (2004) will vary with varying bubble size it should be tested, as the lift coefficient has a great influence on the overall flow pattern.

5.2.4   Bubble size prediction

The simulations are run with two different models for coalescence and breakup. The kernel proposed by Wu *et al.* (1998) and the kernel proposed by Moilanen *et al.* (2008). Both are described in detail in Chapter 3.4.

5.2.5   Other settings

The simulations are 1st order implicit transient in three dimensions. The time step size is set to 0.0025s, and the simulation time is set to 200s with averaging done on the last 150s. The time step is halved compared to the flow simulations in Chapter 4 because of convergence problems with the IACE model. Third order spatial discretisation schemes are employed (QUICK). A typical simulation was run on 4 AMD Athlon XP 1.4 GHz nodes and took approximately 12 days.

5.3   Base case simulation results with $u_{G, sup}$ 4.9 mm/s

In this section the results from two of the six base case simulations are presented. The simulation settings, which are similar for both simulations are shown in Table 7.

Table 7   Simulation settings for both IACE closure approaches.

Parameter	Value
Superficial gas velocity, $u_{G,sup}$	4.9mm/s
Time step size, Δt	0.0025s
Inlet gas volume fraction, α_G	0.0274
Inlet gas velocity, $u_{G,inlet}$	2.86m/s
Inlet bubble diameter, d_B	4mm
Drag coefficient, C_D	Eq. 11
Lift coefficient, C_L	0.5
Added virtual mass, C_{VM}	None
Turbulence	Eqs. 20 and 25
Bubble induced turbulence	None

The presentation of results from these two simulations is done in the same manner so that it is possible to compare the two simulations.

5.3.1   Results with the Wu *et al.* IACE kernels

Contour plots of instantaneous Sauter mean diameter, d_{32}, are shown in Figure 49. It is observed that the Sauter mean diameter is observed to be very high in the lower third of the column just above the gas inlet.

Contour plots of instantaneous gas volume fraction, α_G, are shown in Figure 50. The contour plots of α_G are very similar to the contour plots of d_{32} in Figure 49, which is to a certain degree expected as the bubble diameter is only dependant on α_G and interfacial area.
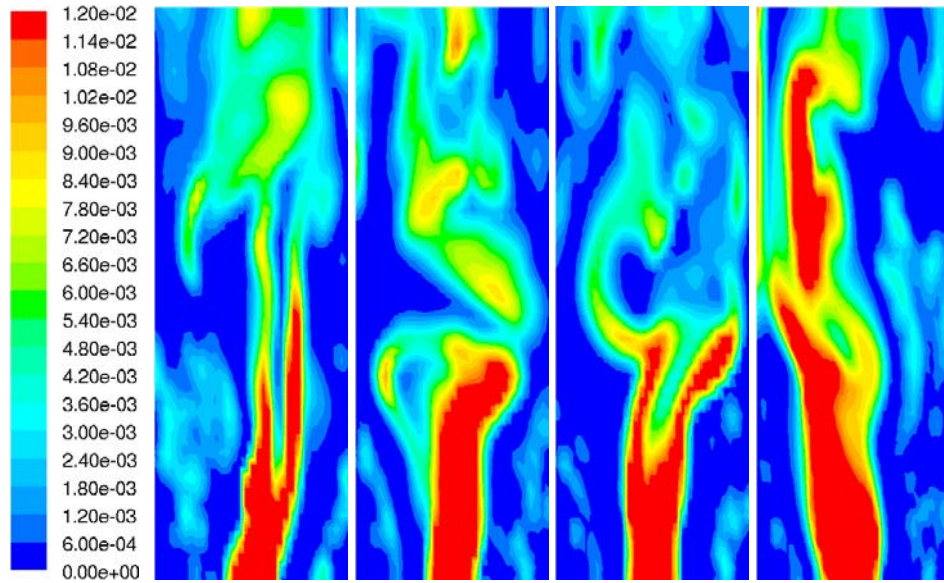
Figure 49   Contour plots of instantaneous Sauter mean diameter in a z-plane (z = 0.075m) at 10s intervals from 170s to 200s.
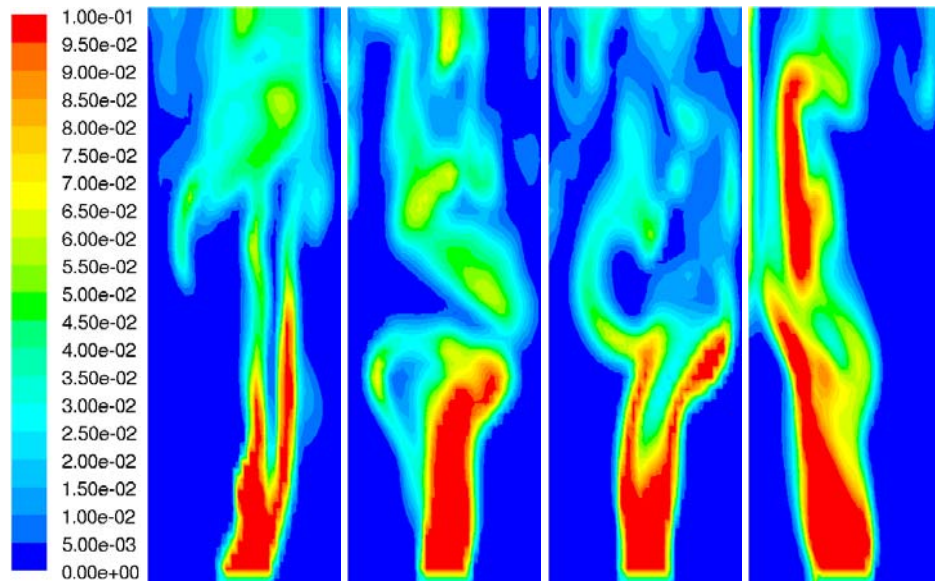
Figure 50   Contour plots of instantaneous gas volume fraction in a z-plane where z = 0.075m at 10s intervals from 170s to 200s.

Contours of instantaneous interfacial area, a_i, are shown in Figure 51. Note the range of the scalar bar. It is observed that the change in a_i is very small, which explains why the contour plots of d_{32} and α_G are so similar.
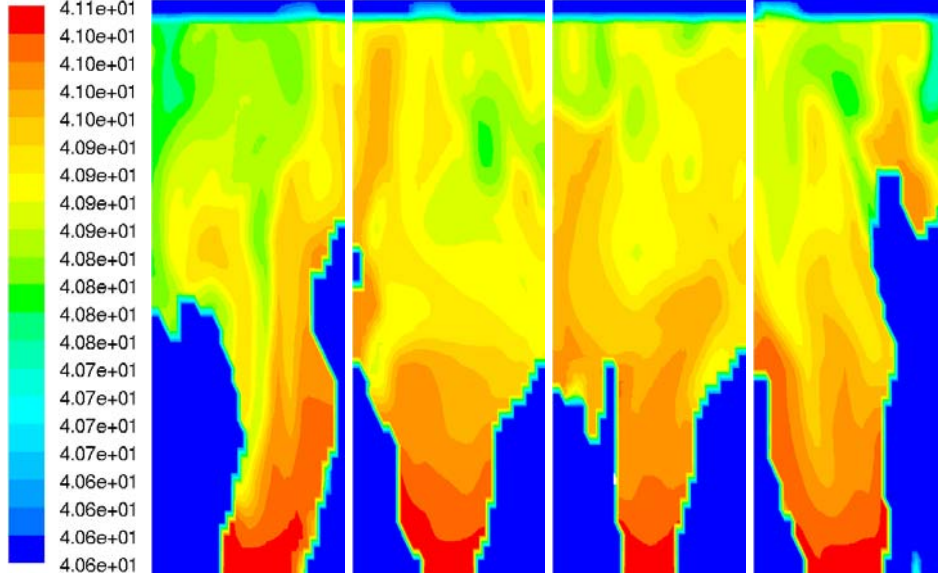
Figure 51   Contour plots of instantaneous interfacial area in a z-plane where z = 0.075m at 10s intervals from 170s to 200s.

The change in a_i is due to coalescence and breakage. Contour plots of coalescence source terms, S_{RC} and S_{WE}, are shown in Figure 52 and contour plots of breakage source term, S_{TI}, and Weber number, We, are shown in Figure 53. It is observed that the coalescence source terms are quite small, which explains the small decrease in a_i through the column. Furthermore it is observed that the breakage source term is zero in the plane of view. This is due to We being less than the critical Weber number, We_{cr}, of 6.0 in the plane of view.
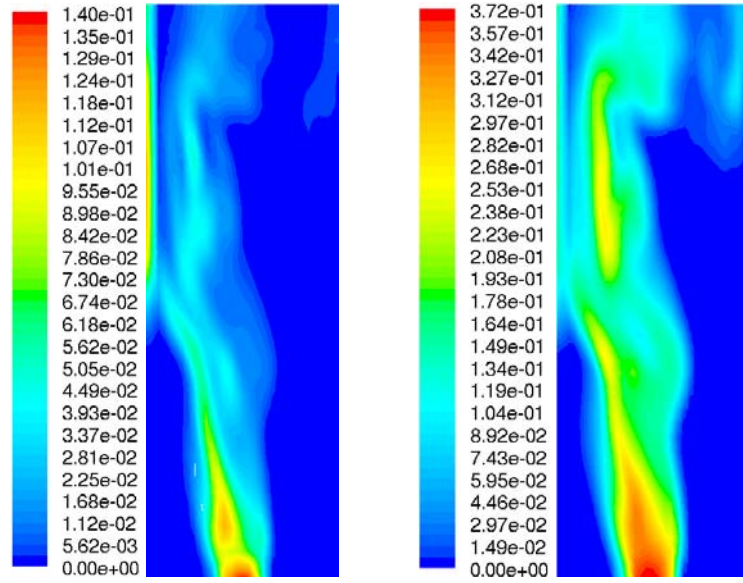
*Figure 52   Contour plots of instantaneous coalescence source terms S_{RC}
(left) and S_{WE} (right) in a z-plane (z = 0.075m) at t = 200s.*
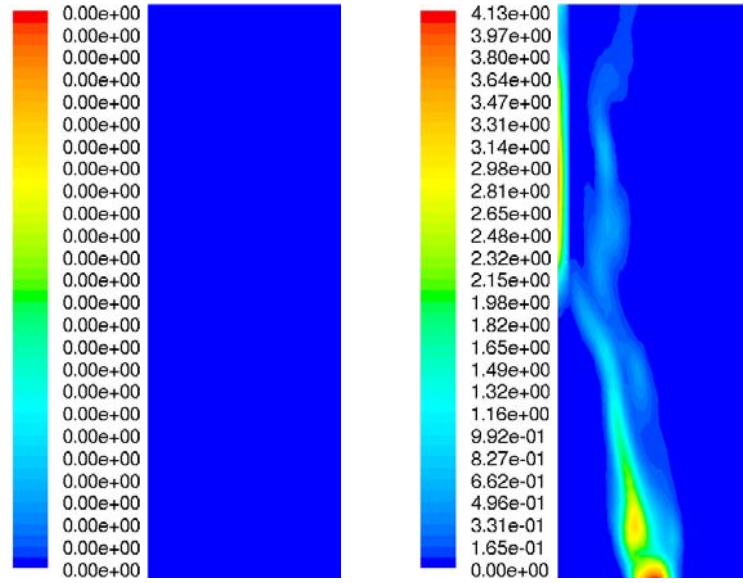
*Figure 53   Contour plot of instantaneous breakage source term S_{TI} (left)
and We (right) in a z-plane (z = 0.075m) at t = 200s.*

In Figure 54 contour plots of time averaged d_{32} and α_G are shown. Again, the contour plots are noted to be very similar.
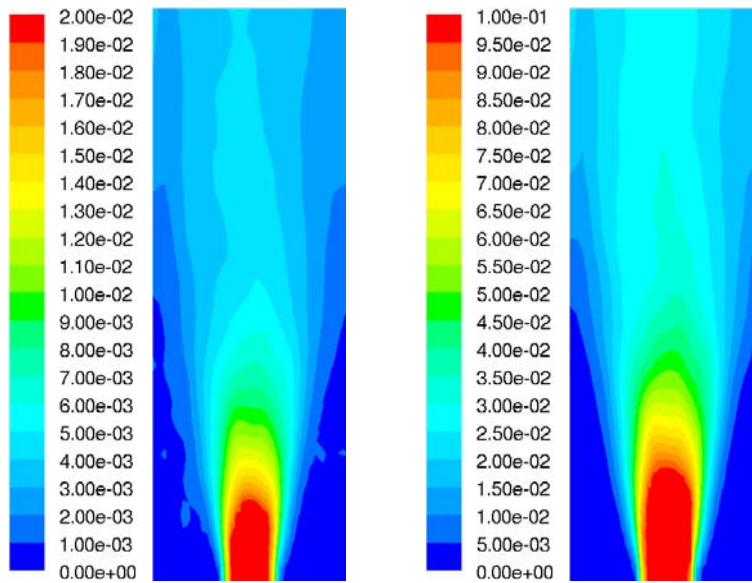
Figure 54 Contour plot of average d_{32} (left) and average α_G (right) in a z-plane (z = 0.075m) at t = 200s.

In Figure 55 and Figure 56 the axial and radial profiles of simulated time averaged d_{32} are compared with the experimental IPI data.
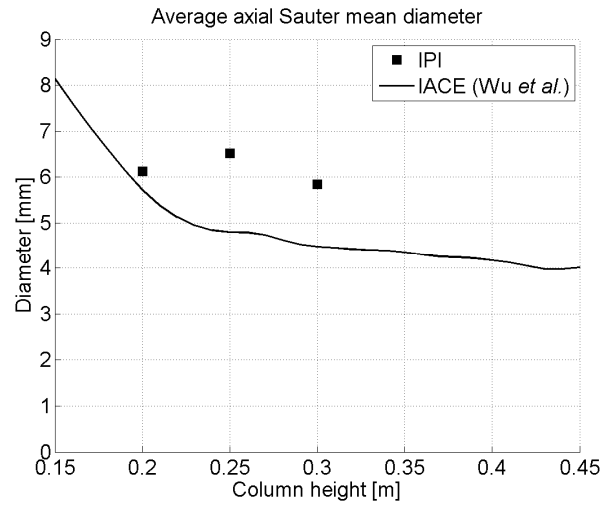
Figure 55   Simulated and measured axial profiles of time averaged d_{32}
           along the axial centreline.

It is observed that the simulated time averaged d_{32} is decreasing with
increasing column height, whereas the measured time averaged d_{32} is
fairly constant. It is also noticed that the simulated time averaged d_{32} is
smaller than the experimental value.
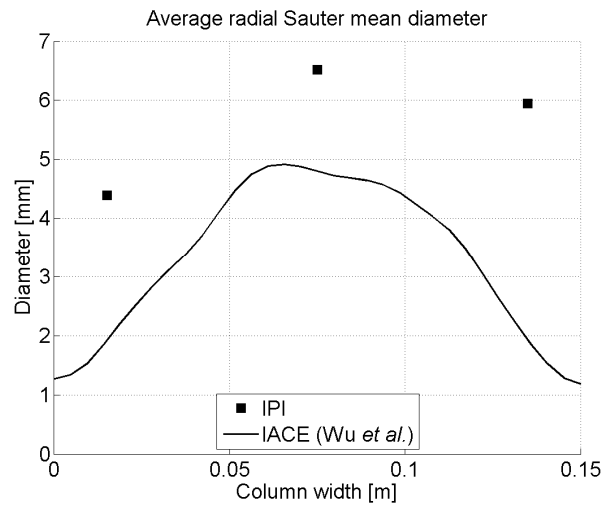
Figure 56   Simulated and measured radial profiles of time averaged d_{32}
           at a height of 0.25 and a depth of 0.075m.

It is observed that the simulated time averaged d_{32} is decreasing toward the walls, a trend that is supported by the IPI measurements. Again the simulated time averaged d_{32} is smaller than the experimental average d_{32}.

In Figure 57 and Figure 58 velocity profiles of time averaged axial gas and average liquid velocity are shown.
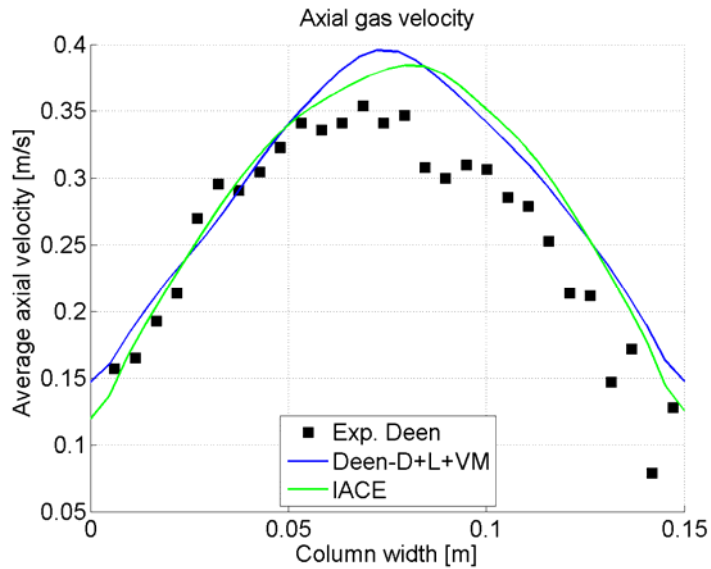
Figure 57   Profiles of average simulated and experimental axial gas velocity at a height of 0.25m and a depth of 0.075m. Experimental data and Deen-D+L+VM simulation data is from Deen (2001).

It is observed that the velocity profiles are in good agreement with the experimental PIV data. This was expected as the lift constant is held constant and BIT is not employed.
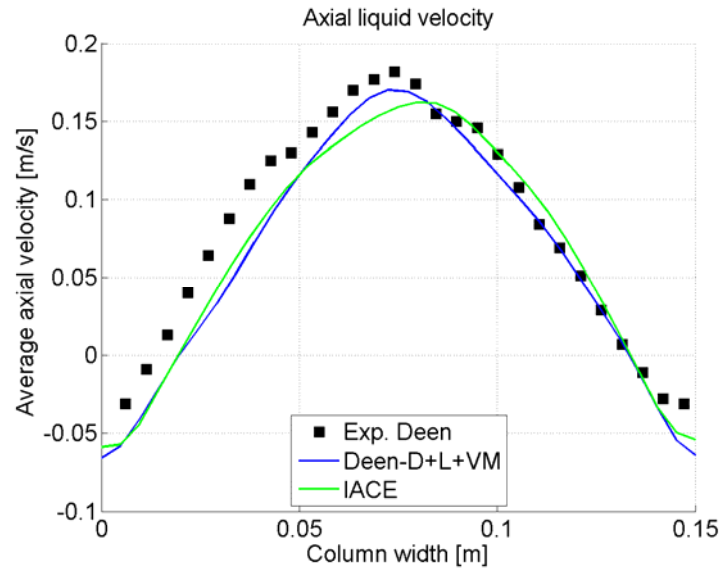
Figure 58 Profiles of time averaged simulated and measured axial liquid velocity at a height of 0.25m and a depth of 0.075m. Experimental data and Deen-D+L+VM simulation data is from Deen (2001).

In Figure 59 and Figure 60 velocity profiles of time averaged axial and average radial velocity fluctuations are shown. It is observed that the profiles of velocity fluctuations are in good agreement with the experimental PIV data.
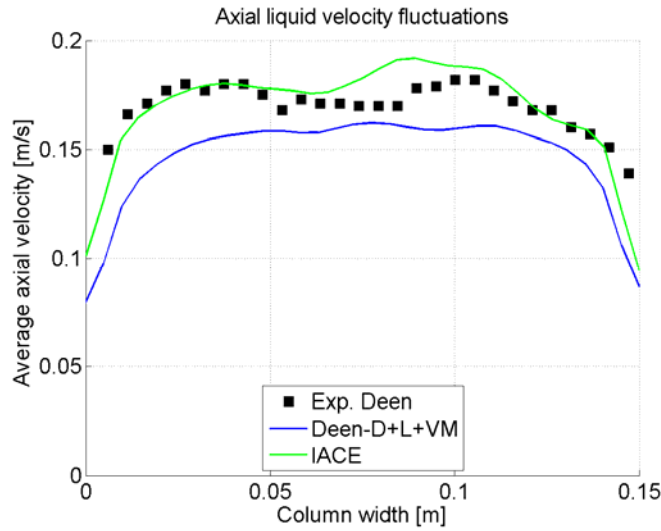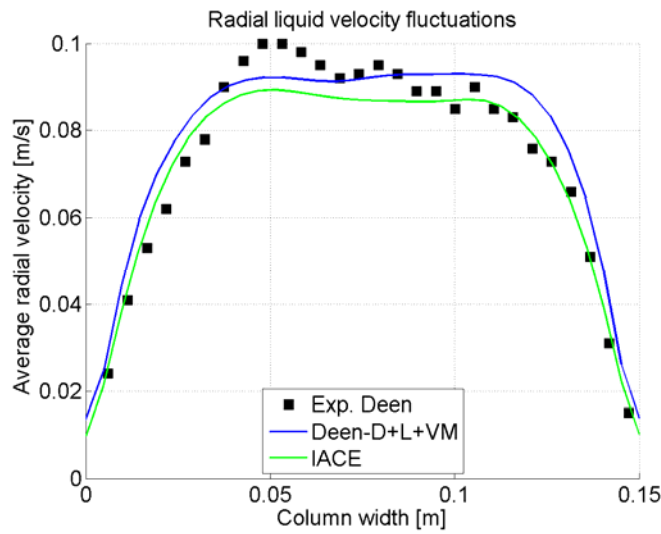
Figure 59 Profiles of time averaged simulated and measured axial liquid velocity fluctuations at a height of 0.25m and a depth of 0.075m. Experimental data and Deen-D+L+VM simulation data is from Deen (2001).

Figure 60 Profiles of time averaged simulated and measured radial liquid velocity fluctuations at a height of 0.25m and a depth of 0.075m. Experimental data and Deen-D+L+VM simulation data is from Deen (2001).

5.3.2   Results with the Moilanen *et al.* IACE kernels

In Figure 61 contour plots of instantaneous Sauter mean diameter, d_{32}, are shown. It is observed that d_{32} is very high not only above the gas inlet but also in the top half of the column when compared to the results with the Wu *et al.* closure approach.
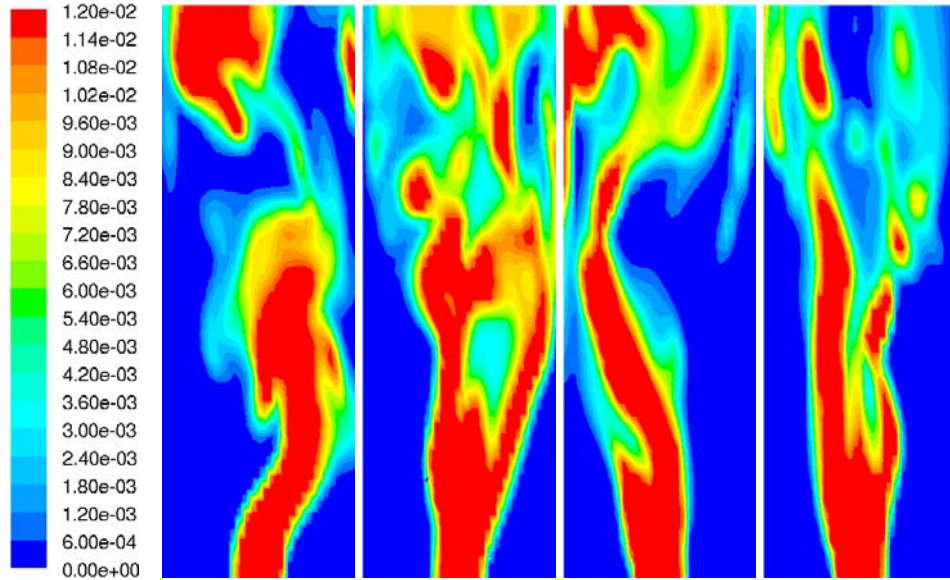
Figure 61   Contour plots of instantaneous d_{32} in a z-plane (z = 0.075m) at 10s intervals from 170s to 200s.

In Figure 62 contour plots of instantaneous gas volume fraction, α_G, are shown. As with the Wu *et al.* closure approach the contour plots of α_G are quite similar to the contour plots of d_{32} in Figure 61. However when looking at contour plots of instantaneous interfacial area, a_i, in Figure 63 it is evident that the change in a_i is much larger than with the Wu *et al.* closure approach. Note the range of the scalar bar.
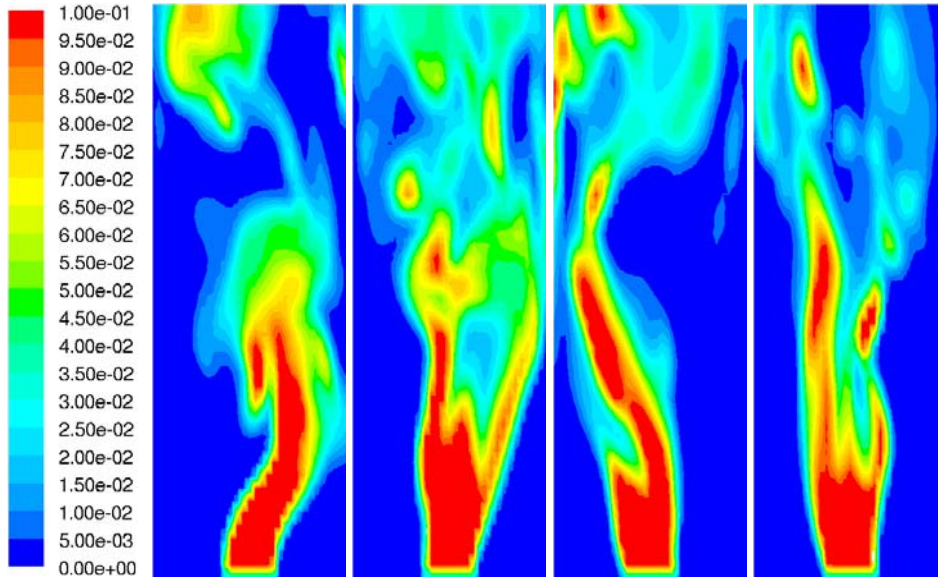
Figure 62   Contour plots of instantaneous α_G in a z-plane (z = 0.075m) at 10s intervals from 170s to 200s.
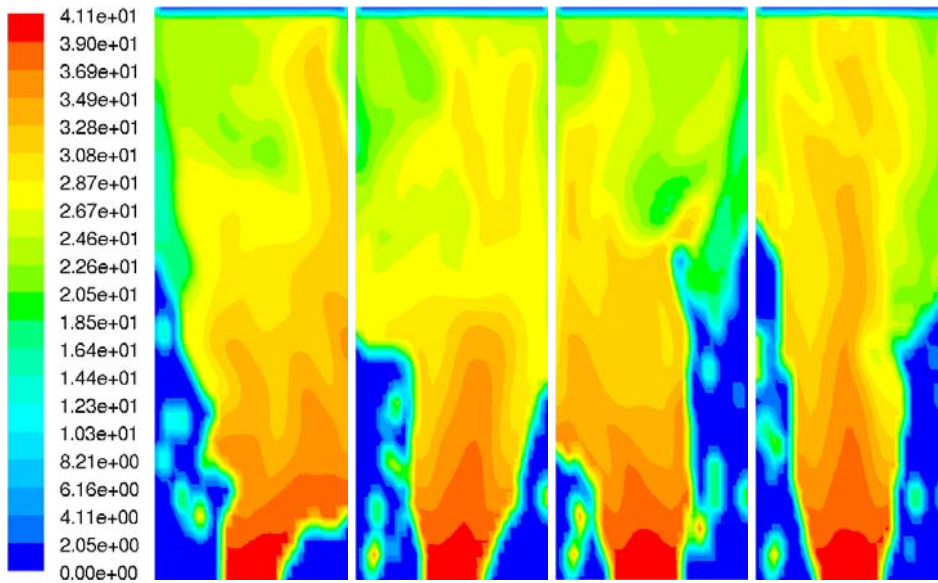

Figure 63   Contour plots of instantaneous a_i in a z-plane (z = 0.075m) at 10s intervals from 170s to 200s.

Instantaneous contour plots of coalescence source term, S_{CO} and breakage source term, S_{BR}, are shown in Figure 64. It is observed that the coalescence is much higher (approximately a factor of 100) than when compared to the results with the Wu *et al.* closure approach. Also it is observed that breakage occur in a few small areas in the plane of view.
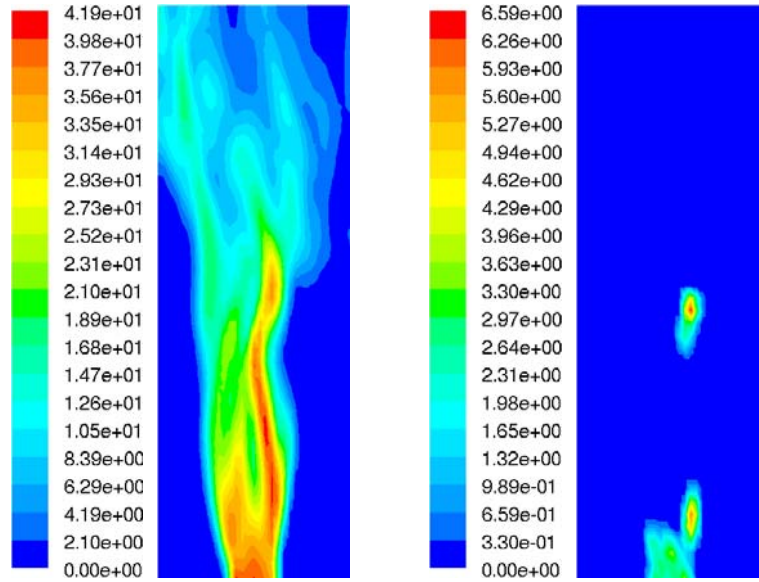

Figure 64   Contour plots of instantaneous S_{CO} (left) and S_{BR} (right) in a z-plane (z = 0.075m) at t = 200s.

In Figure 65 contour plots of instantaneous Weber number are shown. In the right plot the areas which are not turquoise coloured represent a Weber number above 1.5, which is the threshold for breakage to occur.

In Figure 66 contour plots of time averaged d_{32} and α_G are shown. The plots are very similar, which is also expected.
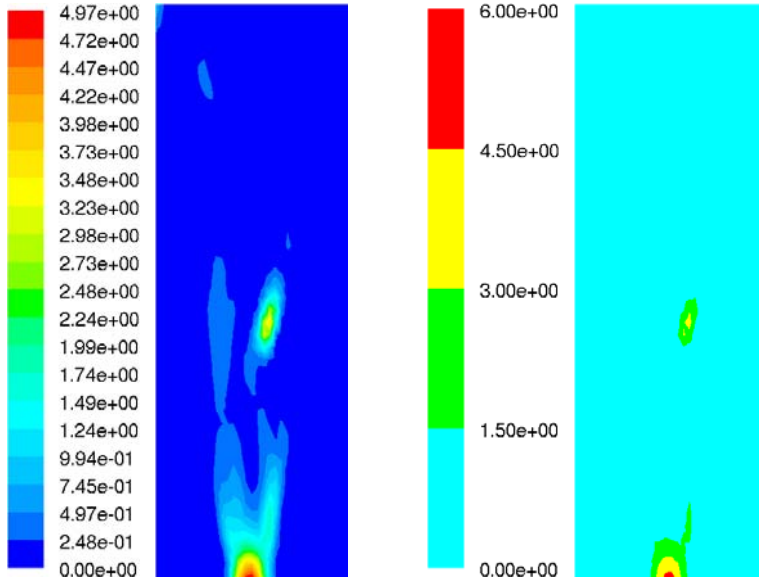
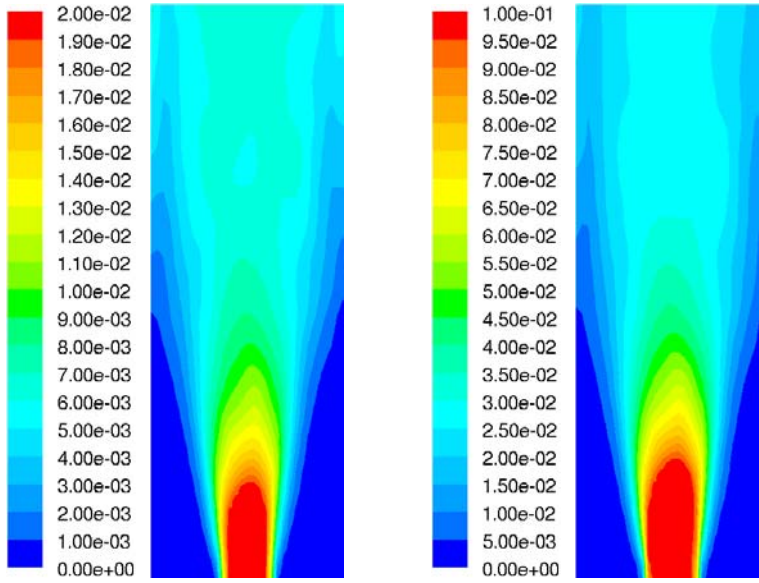*Figure 65   Contour plots of instantaneous We in a z-plane (z = 0.075m) at t = 200s.*

Figure 66   Contour plot of time averaged d_{32} (left) and average α_G (right) in a z-plane (z = 0.075m) at t = 200s.

The time averaged interfacial area and coalescence and breakage source terms are shown in Figure 67. It is observed that S_{CO} is much larger than S_{BR} and that significant breakage is only located just above the inlet in the bottom third of the bubble column.
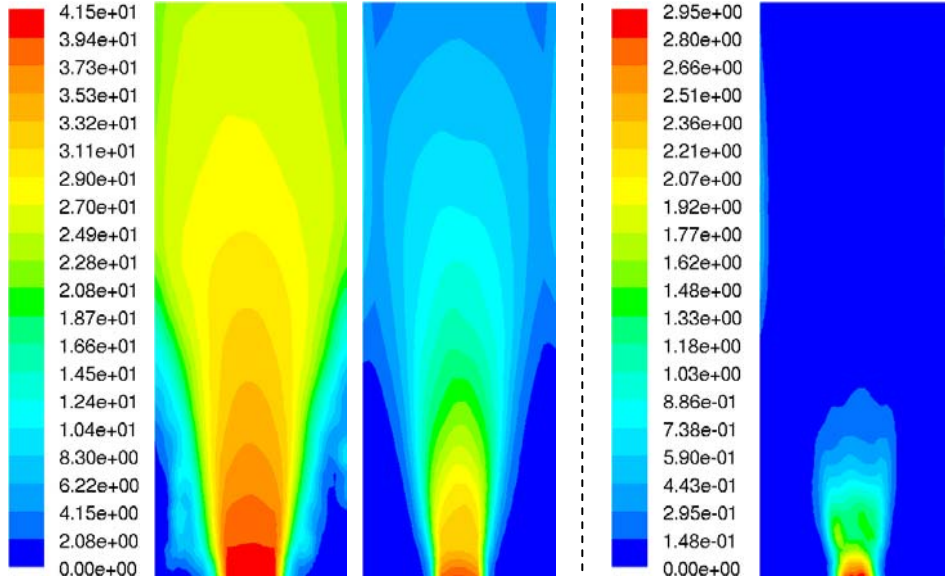

Figure 67   Contour plots of time averaged a_i (left), S_{CO} (middle) and S_{BR} (right) in a z-plane (z = 0.075m) at t = 200s. Note the different scalar bars.

In Figure 68 and Figure 69 simulated axial and radial profiles of time averaged d_{32} are shown and compared with experimental IPI data. It is observed that the simulated average axial d_{32} is decreasing with increasing column height until approximately 0.33m. From then on the d_{32} is more or less constant. It is also noticed that the simulated d_{32} fits the experimental d_{32} quite well except at the point y = 0.2 m. It is noticed that the simulated radial d_{32} is decreasing toward the walls. Although the simulated d_{32} is larger than the experimental value in x = 0.075m, the simulated values near the walls are more than 50% smaller than the experimental values.
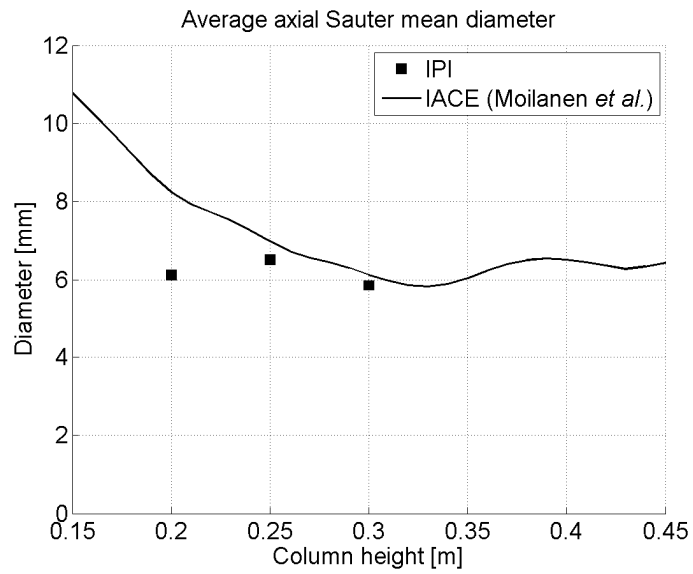
Figure 68 Axial profiles of simulated and measured time averaged d_{32} along the axial centreline.
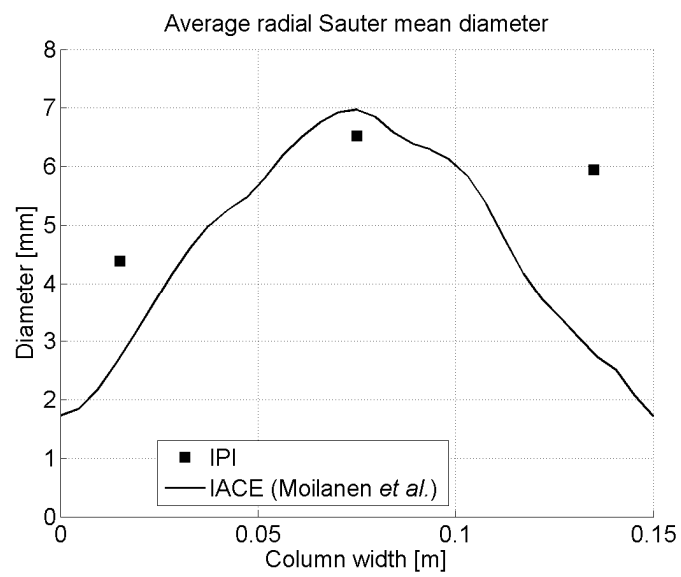

Figure 69 Axial profiles of simulated and measured time averaged d_{32} at a height of 0.25m and a depth of 0.075m.

In Figure 70 profiles of time averaged simulated axial gas velocity are shown.
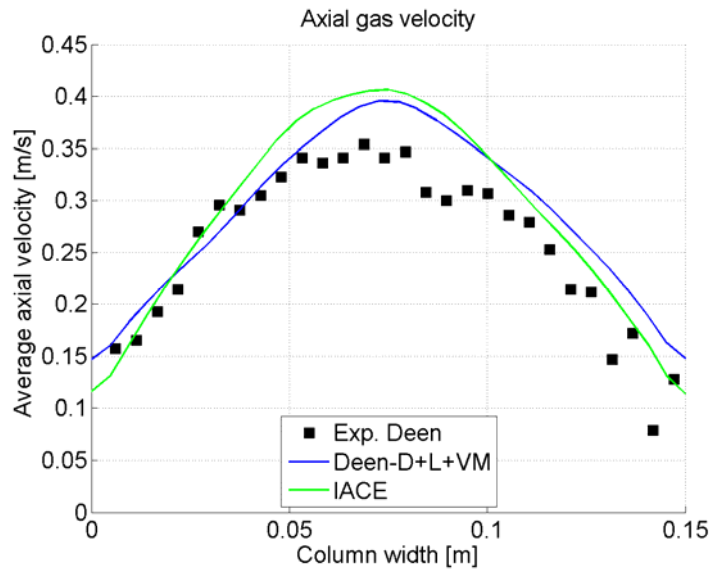

Figure 70   Profiles of time averaged simulated and measured axial gas velocity at a height of 0.25m and a depth of 0.075m. Experimental data and Deen-D+L+VM simulation data is from Deen (2001).

It is observed that the velocity profiles are in good agreement with the experimental PIV data as was also seen with the Wu *et al.* kernels in the latter section.

In Figure 71 profiles of time averaged simulated axial liquid velocity are shown. Again, it is observed that the liquid velocity profile is in good agreement with the experimental PIV data.
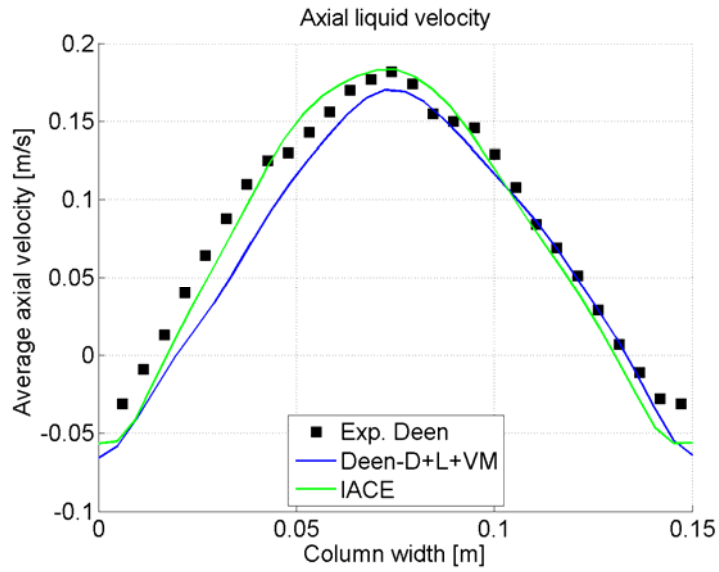
Figure 71 Profiles of time averaged simulated and experimental axial liquid velocity at a height of 0.25m and a depth of 0.075m. Experimental data and Deen-D+L+VM simulation data is from Deen (2001).

In Figure 72 profiles of time averaged simulated axial liquid velocity fluctuations are shown and compared with experimental data. It is observed that the simulated time averaged fluctuations are in good agreement with the experimental data. This is also the case for the time averaged simulated radial liquid velocity fluctuations, which are shown in Figure 73 and compared with experimental data
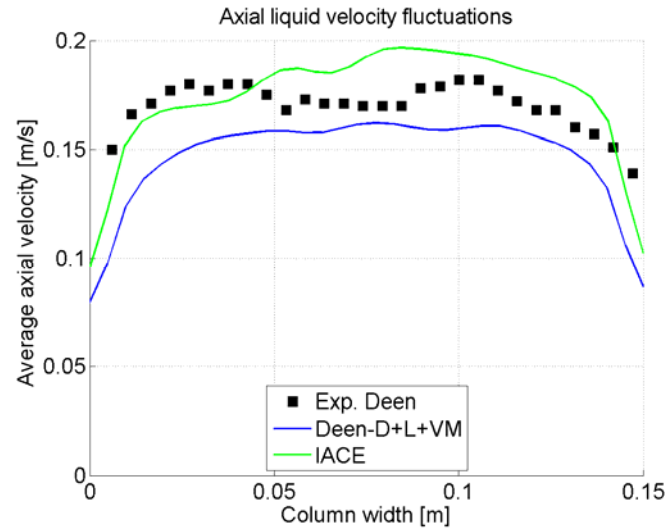
Figure 72 Profiles of time averaged simulated and measured axial liquid velocity fluctuations at a height of 0.25m and a depth of 0.075m. Experimental data and Deen-D+L+VM simulation data is from Deen (2001).
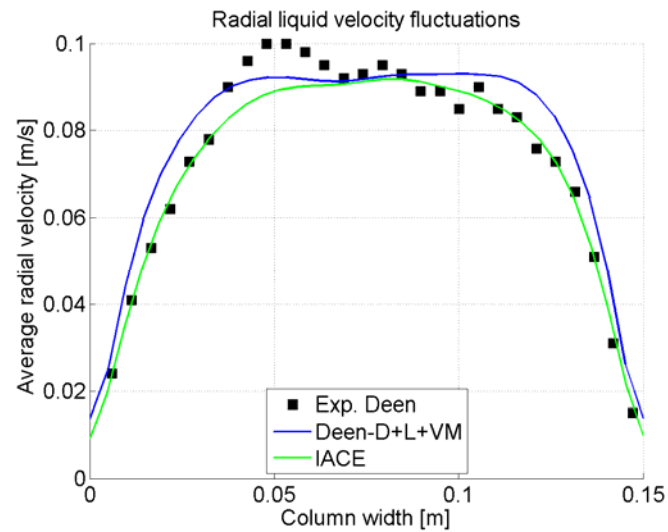

Figure 73 Profiles of time averaged simulated and measured radial liquid velocity fluctuations at a height of 0.25m and a depth of 0.075m. Experimental data and Deen-D+L+VM simulation data is from Deen (2001).

5.4　Results with a superficial gas velocity of 3.2 mm/s

In this section the results from the two base case simulations with a superficial gas velocity of 3.2 mm/s are presented and compared with experimental IPI data and interpolated PIV data from Chapter 2.6.

5.4.1　Bubble size

In Figure 74, both predictions of axial profiles of time-averaged d_{32} are compared with experimental IPI data.
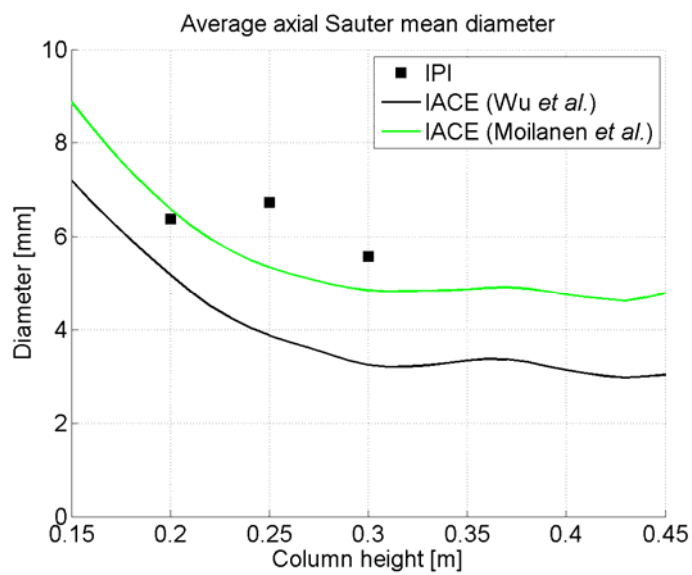

Figure 74 Axial profiles of simulated time averaged d_{32} versus experimental d_{32} along the axial centreline.

It is observed that the time averaged d_{32} is decreasing with increasing column height until y = 0.3m, where the d_{32} becomes more or less constant. This trend was also observed with $u_{G,sup}$ 4.9 mm/s. It is also evident that the simulation with Wu *et al.* kernels predicts a too low average d_{32} when compared to the IPI data. The simulation with kernels by Moilanen *et al.* gives a better prediction of d_{32} even though it may be a bit low compared to the IPI data.

In Figure 75 both predictions of radial profiles of time averaged d_{32} are compared with experimental IPI data.
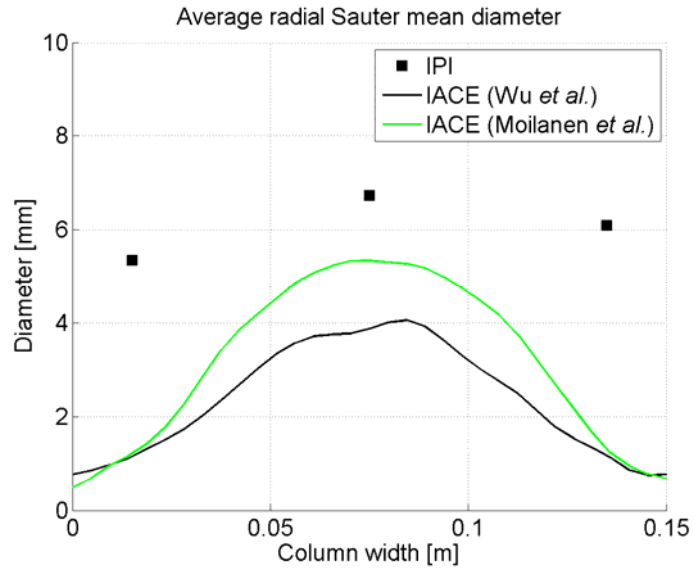

Figure 75   Radial   profiles   of   simulated   time   averaged   d$_{32}$ versus experimental d$_{32}$ at a height of 0.25 and a depth of 0.075m.

It is observed that both simulations yield too low average d_{32} values when compared with the IPI data, especially toward the walls. The simulation with Moilanen *et al.* kernels however does a better prediction of the average d_{32} than the simulation with Wu *et al.* kernels.

5.4.2   Velocity

Profiles of simulated time averaged axial gas velocity and axial liquid velocity are shown in Figure 76 and Figure 77 respectively. It is noticed that the simulations are in good agreement with the interpolated PIV data except for the prediction of axial gas velocity with kernels by Moilanen *et al.*, where the core velocity is slightly over predicted.

In Figure 78 and Figure 79 profiles of simulated time averaged axial and radial liquid fluctuations are shown respectively.
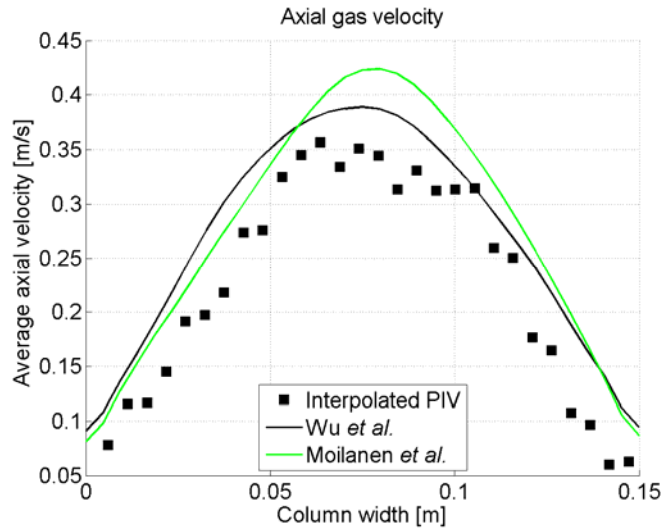
Figure 76 Profiles of time averaged simulated axial gas velocity at a height of 0.25m and a depth of 0.075m. Experimental PIV data is interpolated from Deen (2001).

Figure 77 Profiles of time averaged simulated axial liquid velocity at a height of 0.25m and a depth of 0.075m. Experimental PIV data is interpolated from Deen (2001).

Figure 78 Profiles of time averaged simulated axial liquid velocity fluctuations at a height of 0.25m and a depth of 0.075m. Experimental PIV data is interpolated from Deen (2001).
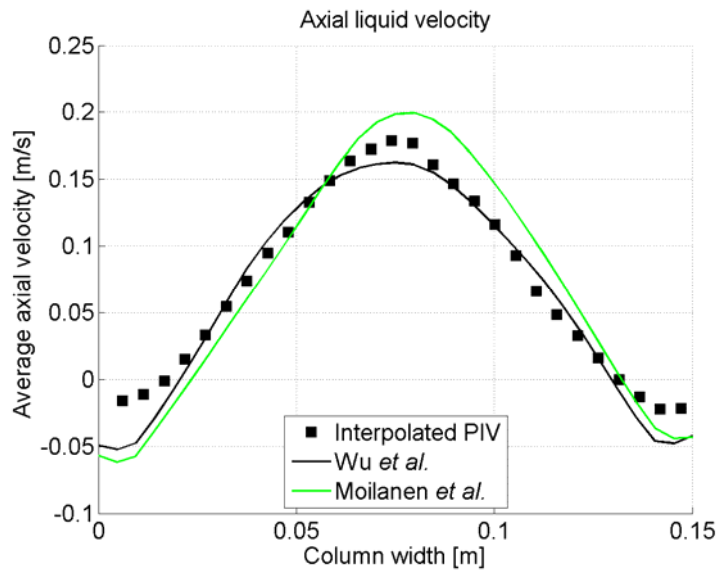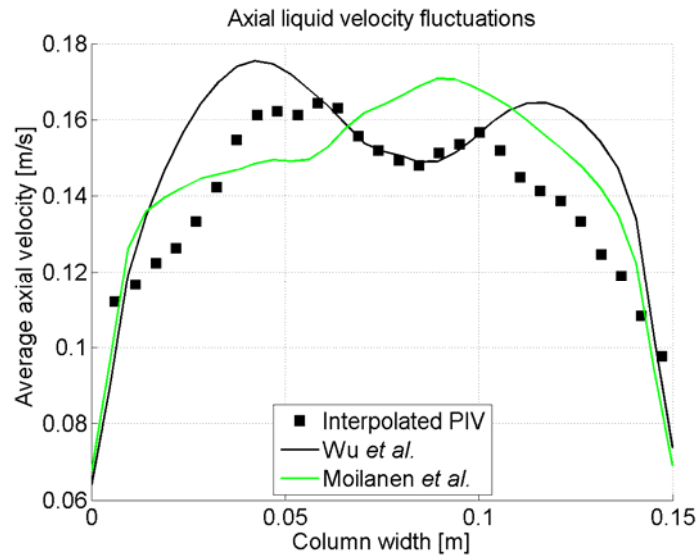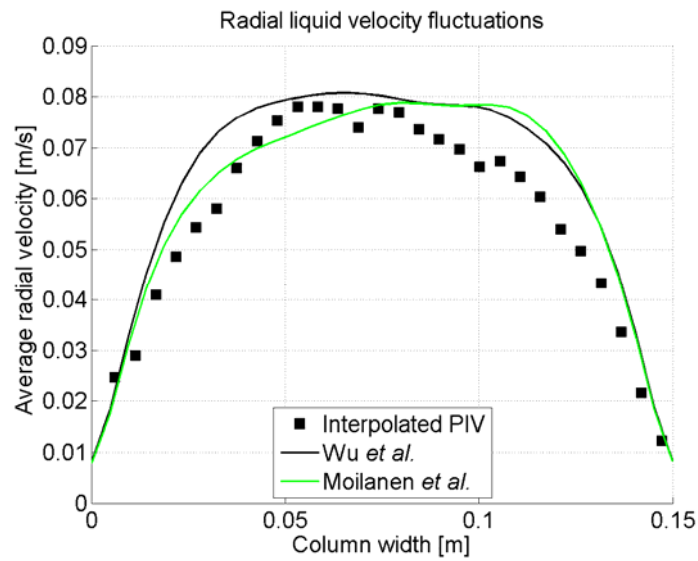

Figure 79 Profiles of time averaged simulated radial liquid velocity fluctuations at a height of 0.25m and a depth of 0.075m. Experimental PIV data is interpolated from Deen (2001).

It is observed that the velocity fluctuation profiles for both simulations show good agreement with the interpolated PIV data.

5.5   Results with a superficial gas velocity of 6.6 mm/s

In this section the results from the two base case simulations with a superficial gas velocity of 6.6 mm/s are presented and compared with experimental IPI data and interpolated PIV data from Chapter 2.6.

5.5.1   Bubble size

In Figure 80 axial profiles of time averaged d_{32} for both simulations are compared with experimental IPI data, and in Figure 81 radial profiles of time averaged d_{32} for both simulations are compared with experimental IPI data.
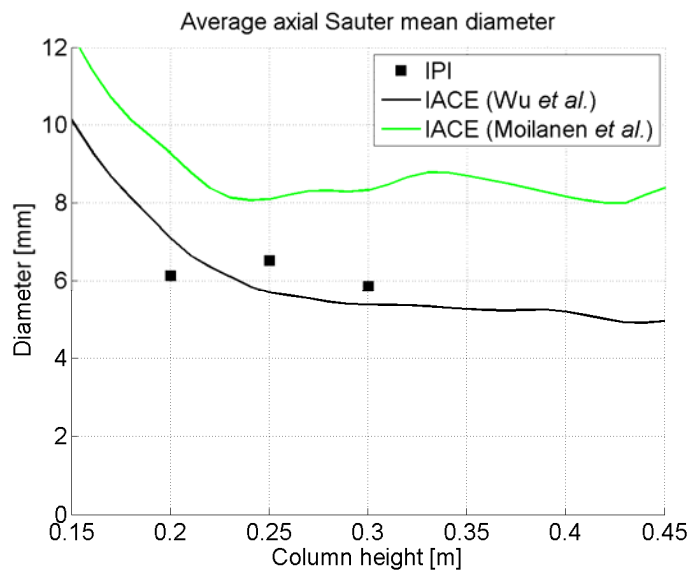

Figure 80   Axial   profiles   of   simulated   time   averaged d_{32} versus experimental d_{32} along the axial centreline.

It is noticed that the simulated average d_{32} with the Wu *et al.* kernels is in good agreement with the experimental data.
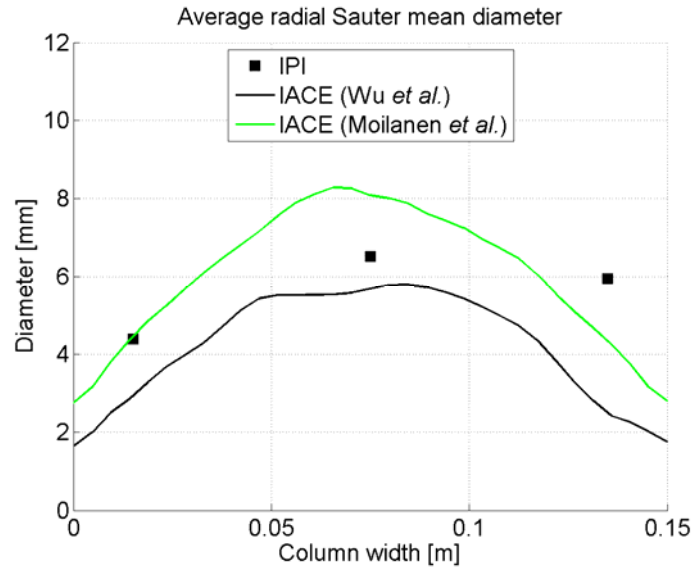
Figure 81   Radial   profiles   of   simulated   time   averaged d_{32} versus experimental d_{32} along the axial centreline.

It is observed that the simulations again predict the maximum average d_{32} in the core and a lower average d_{32} toward the walls as is the case for the IPI results. Both simulations are in somewhat agreement with the IPI data.

5.5.2   Velocity

Profiles of simulated time averaged axial gas velocity and axial liquid velocity are shown in Figure 82 and Figure 83 respectively for both base cases. The simulated profiles are compared with interpolated PIV data. It is observed that the simulation with the Moilanen *et al.* kernels is in better agreement with the axial gas and liquid velocity profiles.

Figure 82   Profiles of time averaged simulated axial gas velocity at a height of 0.25m and a depth of 0.075m. Experimental PIV data is interpolated from Deen (2001).

Figure 83   Profiles of time averaged simulated axial liquid velocity at a height of 0.25m and a depth of 0.075m. Experimental PIV data is interpolated from Deen (2001).

Figure 84   Profiles of time averaged simulated axial liquid velocity fluctuations at a height of 0.25m and a depth of 0.075m. Experimental PIV data is interpolated from Deen (2001).

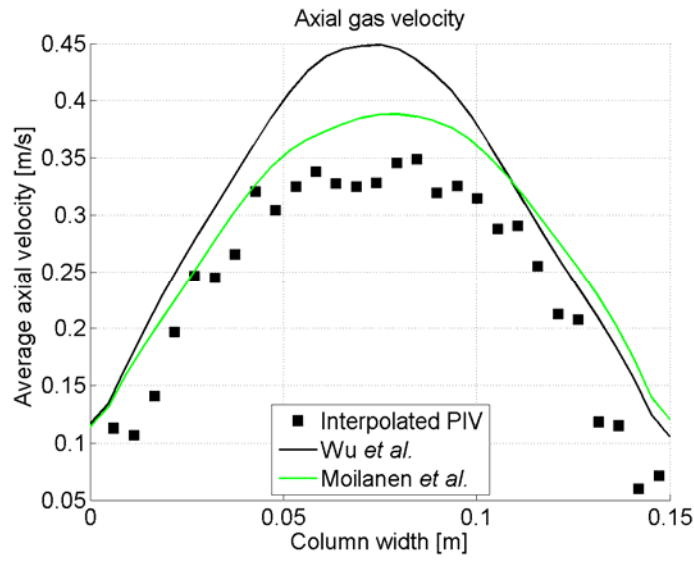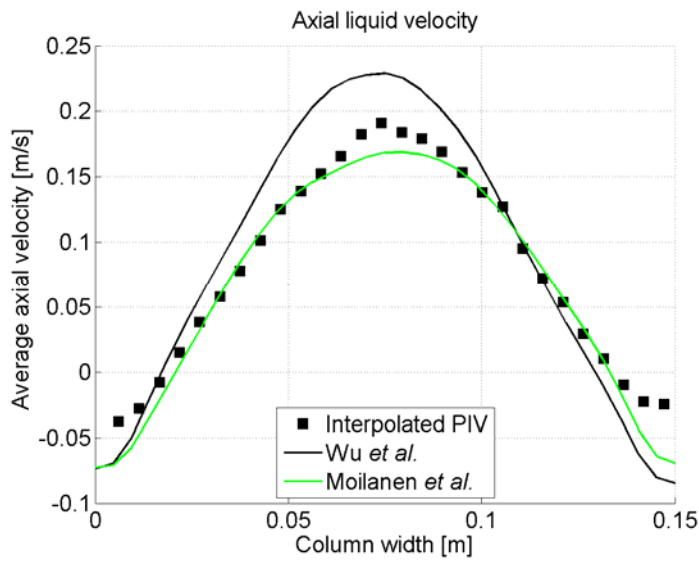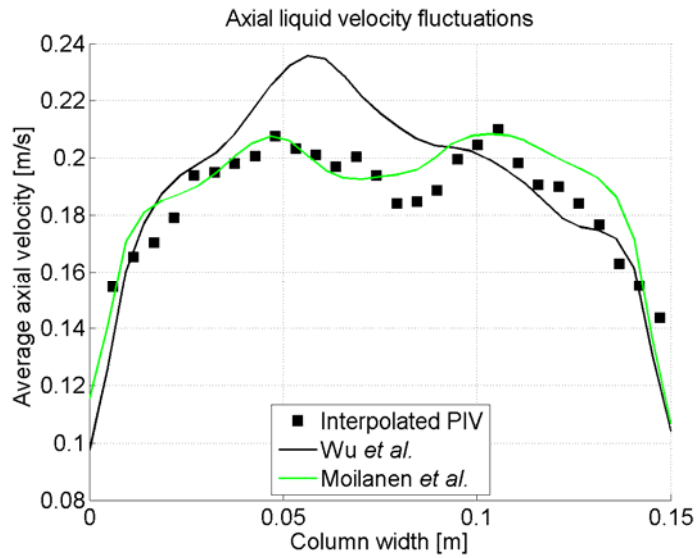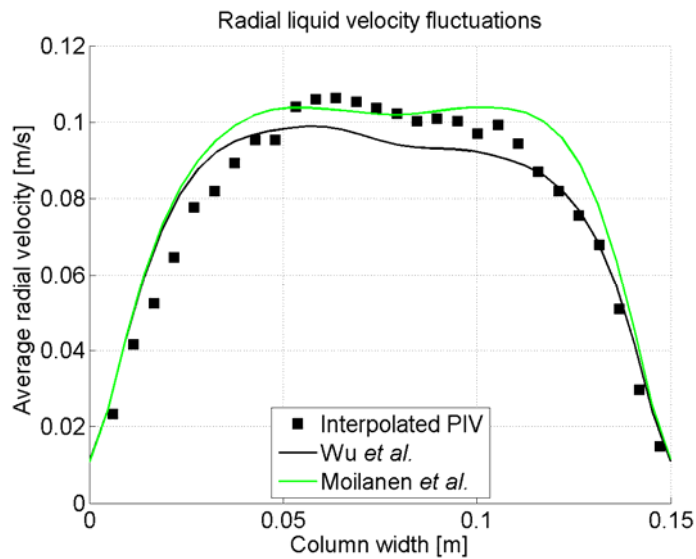

Figure 85   Profiles of time averaged simulated radial liquid velocity fluctuations at a height of 0.25m and a depth of 0.075m. Experimental PIV data is interpolated from Deen (2001).

Profiles of simulated time averaged axial and radial liquid velocity fluctuations are shown in Figure 84 and Figure 85 respectively. It is again observed that the simulation with the Moilanen *et al.* kernels is in better agreement with the interpolated PIV data.

5.6 Parameter study on the six base cases

In this section a parameter study is performed on all six base case simulations. The changes relative to the base cases are listed in Table 8.

Table 8   Cases for the parameter study

Case	Change compared to the base case
Base case	No change
2mm	Inlet diameter is set to 2mm
6mm	Inlet diameter is set to 6mm
8mm	Inlet diameter is set to 8mm
NGV	The gas phase viscosity is laminar
VM	Added virtual mass is included (Eq. 19)
TL	The Tomiyama lift coefficient is included (Eq. 14)
BIT	Bubble induced turbulence is included (Eq. 24)

It was observed in Chapter 4.3 that simulations with the Tomiyama lift coefficient from Eq. 14 predict a too high core velocity in the column. This is also the case for the IACE simulations, which can be seen in Figure 86.

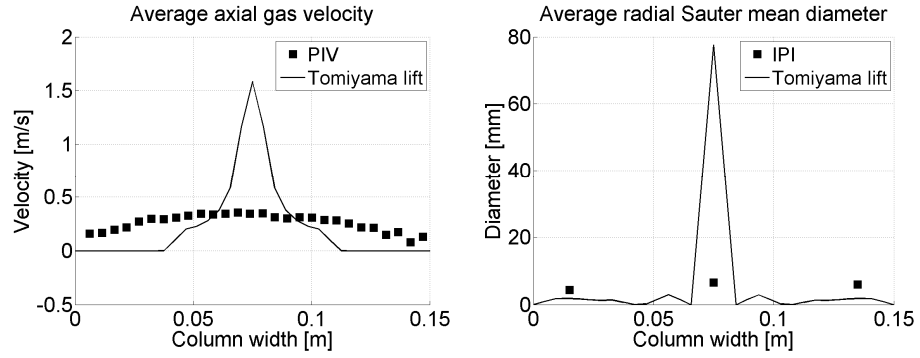*Figure 86   Profile of simulated time averaged axial gas velocity versus*
PIV data (left) and plot of simulated time averaged radial d_{32}
versus IPI data (left) at a height of 0.25m and a depth of
0.075m. Superficial gas velocity 4.9 mm/s. IACE kernels by
Wu et al (1998).

It is observed that the simulated average radial d_{32} is severely over
predicted in the middle of the column and severely under predicted
toward the walls. This behaviour is observed in all the simulations.
Therefore the simulations with the Tomiyama lift coefficient are not
reported in this parameter study.

In Chapter 4.4 it was chosen not to include BIT in the base case flow
model. In Figure 87 it is shown what generally happens when including
BIT in the simulations.

The simulated time averaged d_{32} in the radial direction is severely over
predicted in the core region of the bubble column. This results in an over
prediction of the time averaged axial gas velocity in the core region. It
was observed that the simulations with BIT showed an erratic behaviour,
which resulted in random crashes. With a simulation time of 14 days per
simulation it was not possible to gain usable results for this parameter
study. The simulations with BIT are therefore not reported in this
parameter study.
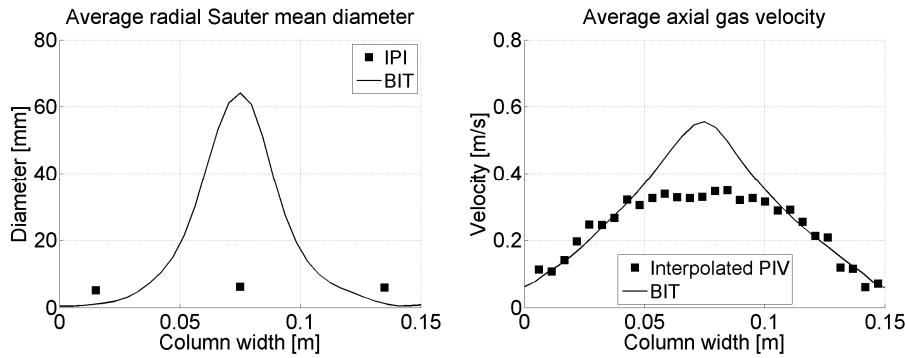
Figure 87   Plot of simulated time averaged radial d_{32} versus IPI data (left) and profile of simulated time averaged axial gas velocity versus interpolated PIV data (right) at a height of 0.25m and a depth of 0.075m. Superficial gas velocity 6.6 mm/s. IACE kernels by Wu et al (1998).

5.6.1   Superficial gas velocity 4.9 mm/s

In this section a parameter study with a superficial velocity of 4.9 mm/s is presented.

Predictions of axial and radial profiles of time averaged d_{32} are compared with experimental IPI data in Figure 88 and Figure 89.

Predictions of profiles of axial time averaged gas and liquid velocities are compared with experimental PIV data in Figure 90 and Figure 91.

Predictions of time averaged axial and radial liquid velocity fluctuations are compared with experimental PIV data in Figure 92 and Figure 93.
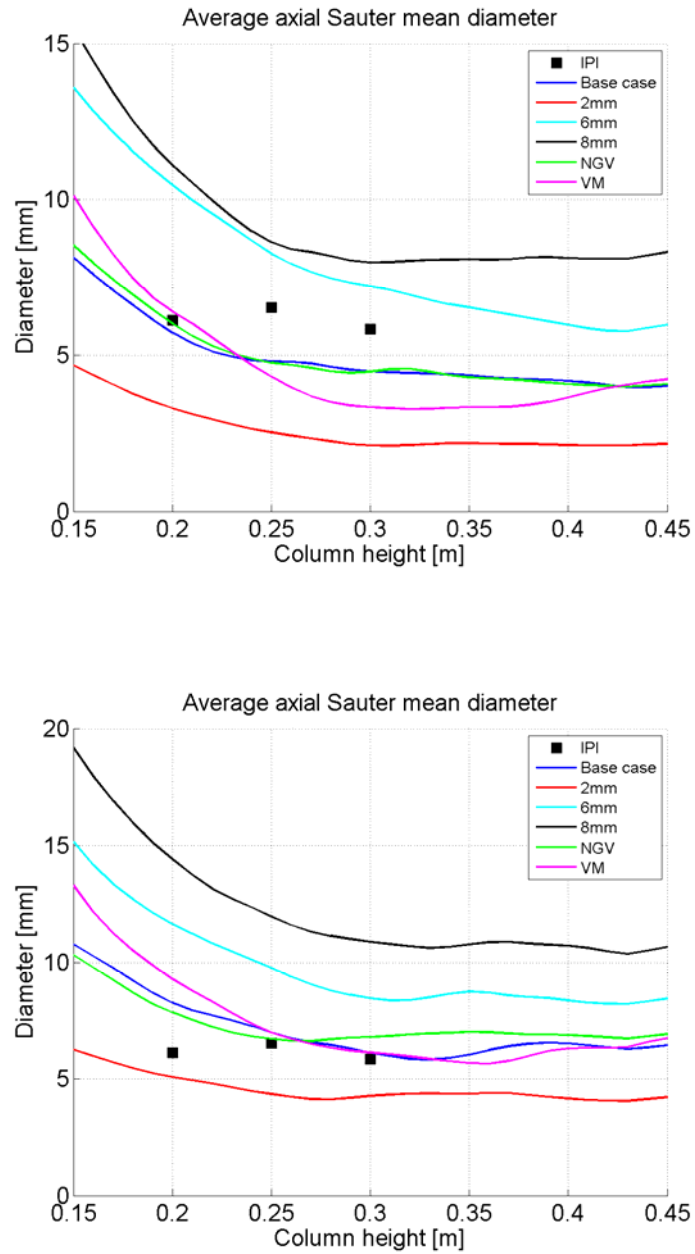
Figure 88 Profiles of time averaged axial d_{32} versus IPI data at the axial centreline. Wu et al. kernels (top) and Moilanen et al. kernels (bottom).

Figure 89 Profiles of time averaged radial d_{32} versus IPI data at a height of 0.25m and a depth of 0.075m. Wu et al. kernels (top) and Moilanen et al. kernels (bottom).

*Figure 90   Profiles of time averaged axial gas velocity versus PIV data
            at a height of 0.25m and a depth of 0.075m. Wu et al. kernels
            (top) and Moilanen et al. kernels (bottom). PIV data is from
            Deen (2001).*

Figure 91 Profiles of time averaged axial liquid velocity versus PIV data at a height of 0.25m and a depth of 0.075m. Wu et al. kernels (top) and Moilanen et al. kernels (bottom). PIV data is from Deen (2001).

Figure 92   Profiles of time averaged axial liquid velocity fluctuations versus PIV data at a height of 0.25m and a depth of 0.075m. Wu et al. kernels (top) and Moilanen et al. kernels (bottom). PIV data is from Deen (2001).

Figure 93   Profiles of time averaged radial liquid velocity fluctuations versus PIV data at a height of 0.25m and a depth of 0.075m. Wu et al. kernels (top) and Moilanen et al. kernels (bottom). PIV data is from Deen (2001).

From the figures in this section it is observed that the velocity profiles for all cases are quite similar and in good agreement with experimental PIV data. The significant difference between the cases is seen in the prediction of average d_{32}. Here the average d_{32} predicted by cases "Base case", "VM" and "NGV" is quite similar, but when changing the inlet diameter the average d_{32} changes dramatically. The trend in both axial and radial direction in the column is however the same in all cases with different $d_{B,inlet}$.

5.6.2   Superficial gas velocity 3.2 mm/s

In this section the parameter studies with a superficial velocity of 3.2 mm/s are presented.

Predictions of axial and radial profiles of time averaged d_{32} are compared with experimental IPI data in Figure 94 and Figure 95.

Predictions of profiles of axial time averaged gas and liquid velocities are compared with interpolated PIV data in Figure 96 and Figure 97.

Predictions of time averaged axial and radial liquid velocity fluctuations are compared with experimental PIV data in Figure 98 and Figure 99.

From the figures in this section it is observed that the velocity profiles for all cases are quite similar and in good agreement with interpolated PIV data except for the "VM" case with the Moilanen *et al.* kernels, which is slightly over predicting the average axial gas and liquid core velocity, while slightly under predicting the average radial liquid fluctuations. The significant difference between the cases is again seen in the prediction of average d_{32}. The average d_{32} predicted by cases "Base case", "VM" and "NGV" is quite similar, although the average d_{32} in the core region is a little higher with the "VM" case. Again, when changing the inlet diameter the average d_{32} changes significantly. The trend in both axial and radial direction in the column is again the same in all cases with different $d_{B,inlet}$.

Figure 94 *Profiles of time averaged axial d₃₂ versus IPI data at the axial centreline. Wu et al. kernels (top) and Moilanen et al. kernels (bottom).*

Figure 95 Profiles of time averaged radial d_{32} versus IPI data at the axial centreline. Wu et al. kernels (top) and Moilanen et al. kernels (bottom).
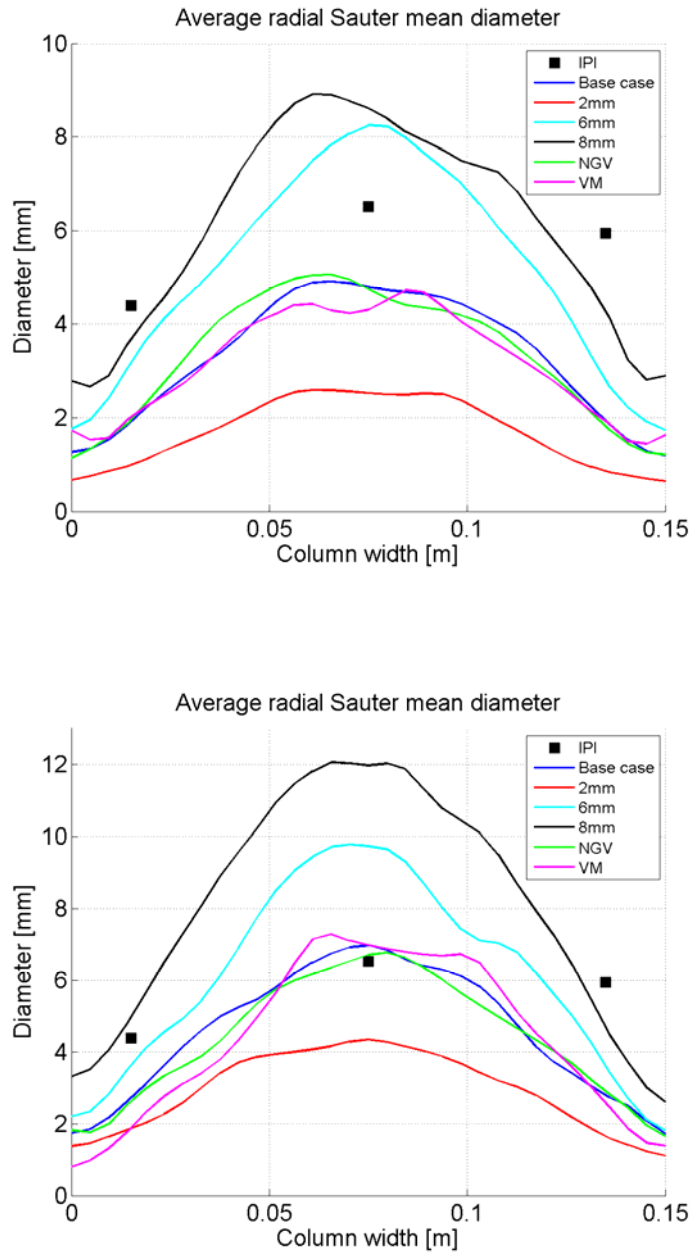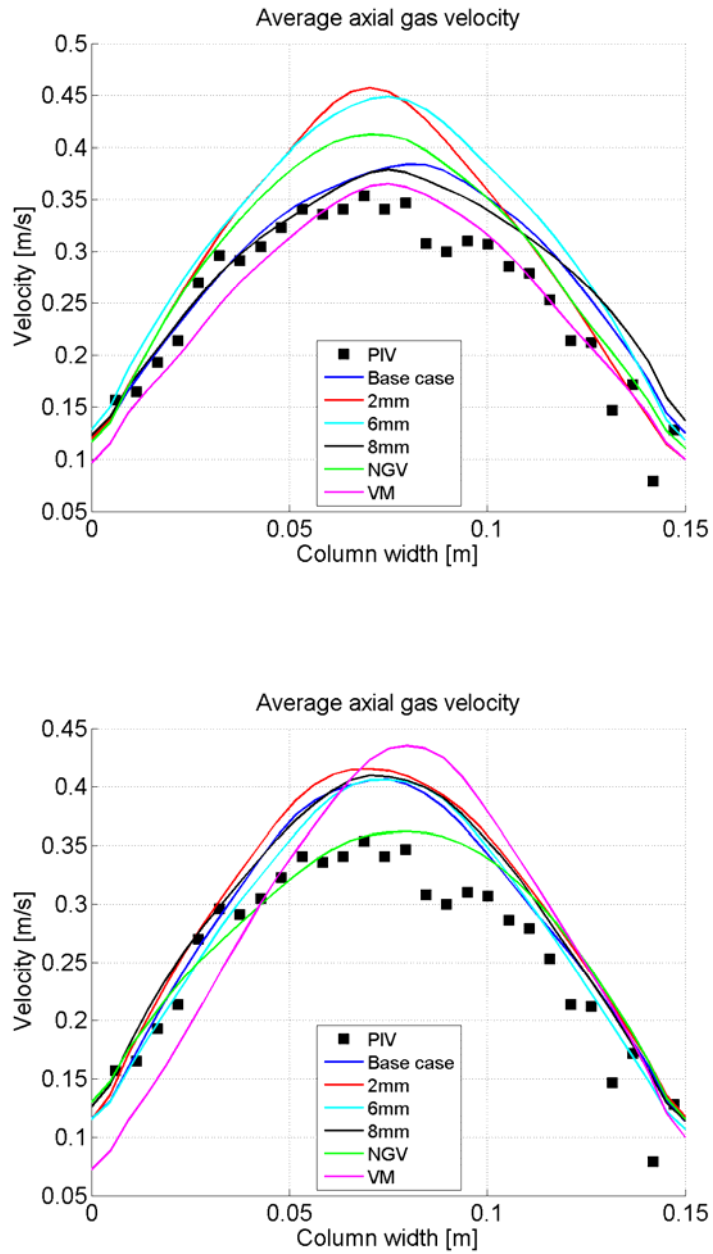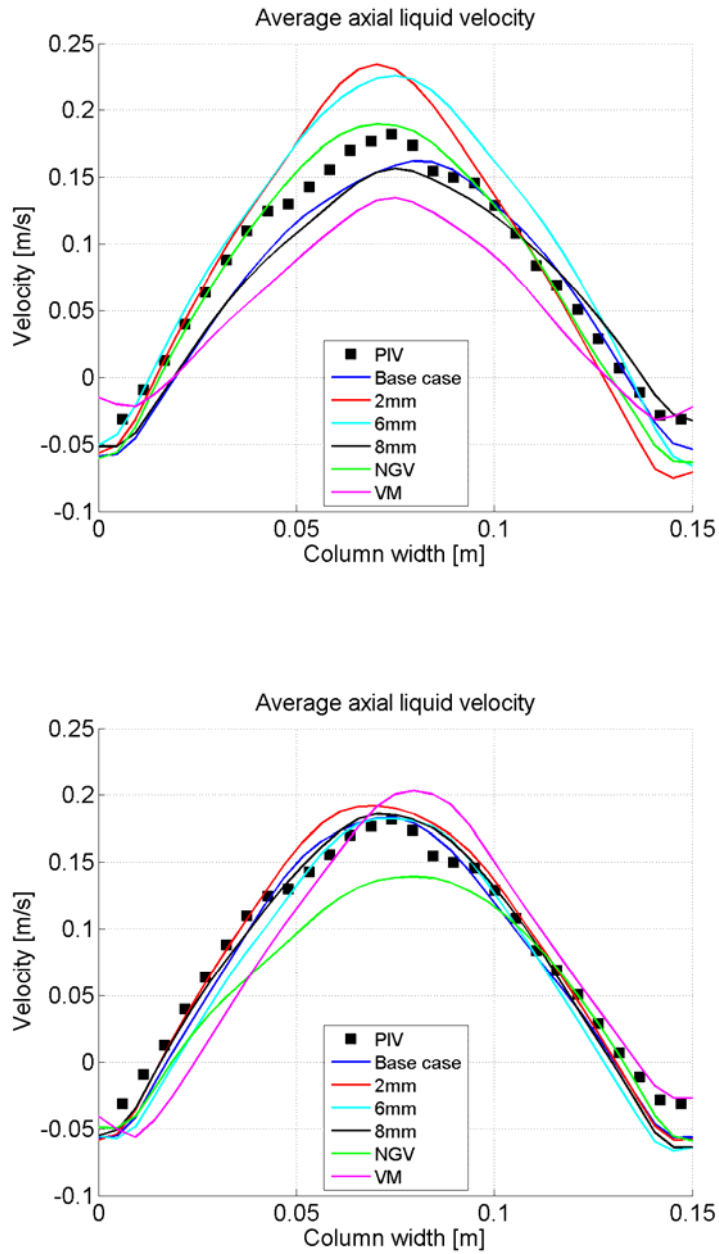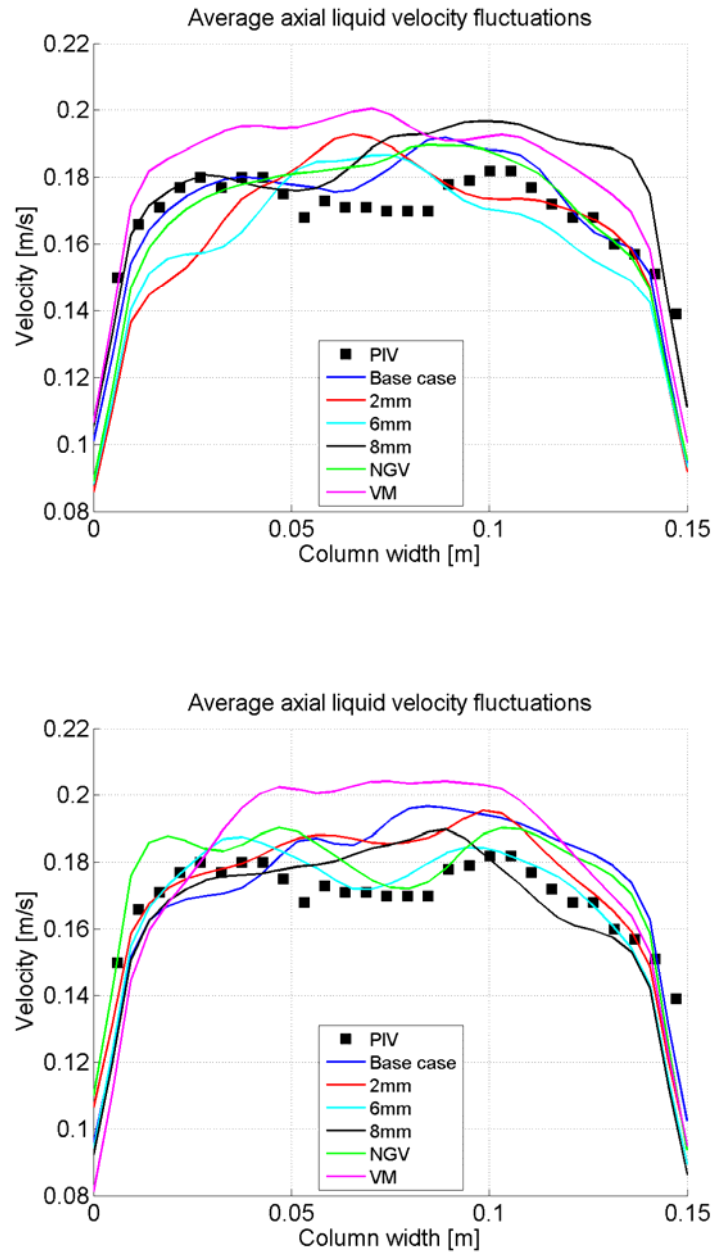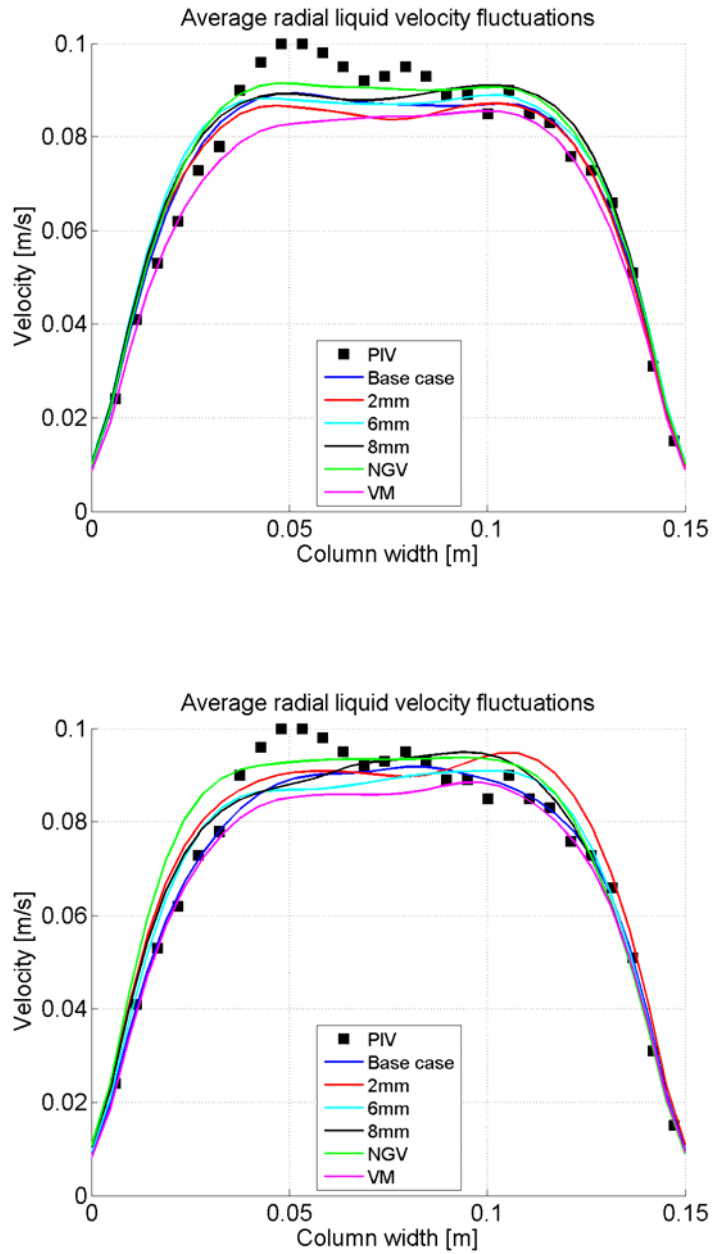
Figure 96 Profiles of time averaged axial gas velocity versus interpolated PIV data at a height of 0.25m and a depth of 0.075m. Wu et al. kernels (top) and Moilanen et al. kernels (bottom).

Figure 97 Profiles of time averaged axial liquid velocity versus interpolated PIV data at a height of 0.25m and a depth of 0.075m. Wu et al. kernels (top) and Moilanen et al. kernels (bottom).

Figure 98 Profiles of time averaged axial liquid velocity fluctuations versus interpolated PIV data at a height of 0.25m and a depth of 0.075m. Wu et al. kernels (top) and Moilanen et al. kernels (bottom).
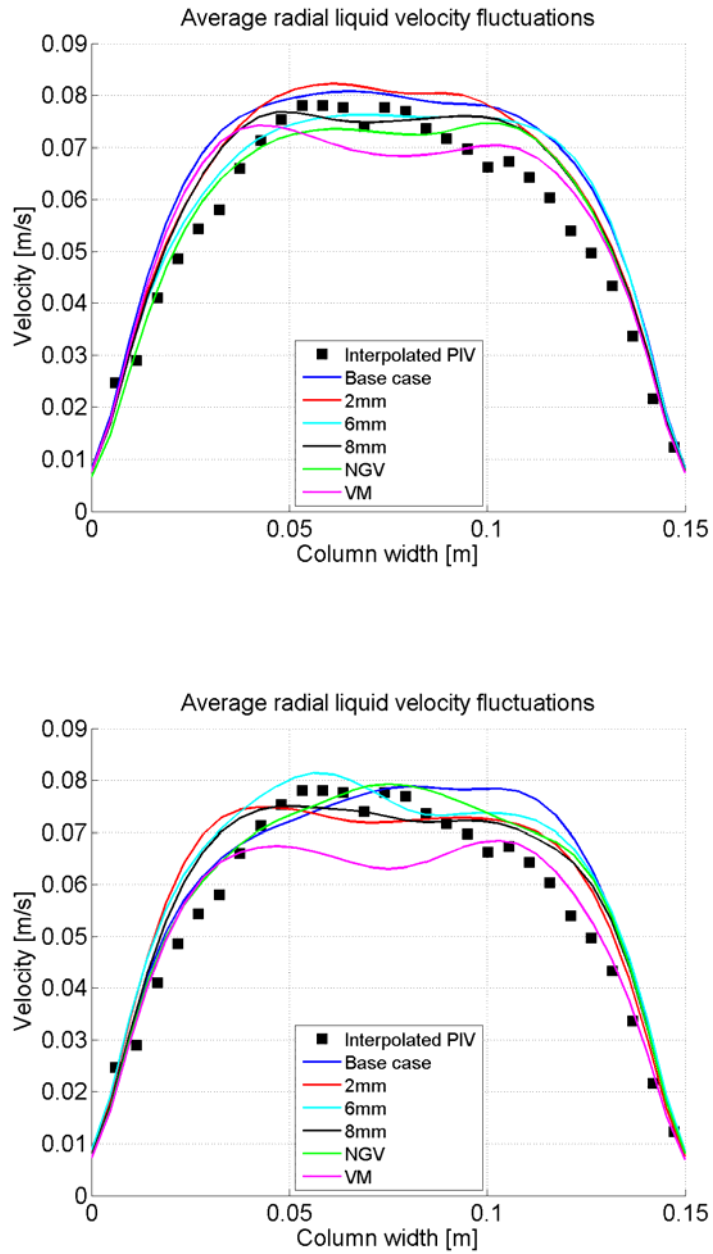
Figure 99 Profiles of time averaged radial liquid velocity fluctuations versus interpolated PIV data at a height of 0.25m and a depth of 0.075m. Wu et al. kernels (top) and Moilanen et al. kernels (bottom).

5.6.3 Superficial gas velocity 6.6 mm/s

In this section the parameter studies with a superficial velocity of 6.6 mm/s are presented.

Predictions of axial and radial profiles of time averaged d_{32} are compared with experimental IPI data in Figure 100 and Figure 101.

Predictions of profiles of axial time averaged gas and liquid velocities are compared with interpolated PIV data in Figure 102 and Figure 103.

Predictions of time averaged axial and radial liquid velocity fluctuations are compared with experimental PIV data in Figure 104 and Figure 105.

From the figures in this section it is observed that the velocity profiles for all cases are quite similar and in good agreement with interpolated PIV data except for the axial gas velocity for most of the cases. The average d_{32} predicted by cases "Base case", "VM" and "NGV" is quite similar. Note that case "NGV" with kernels by Wu *et al.* is not reported due to convergence problems. Again, when changing the inlet diameter the average d_{32} changes significantly, but the trend in both axial and radial direction in the column is again the same in all cases with different $d_{B,inlet}$.
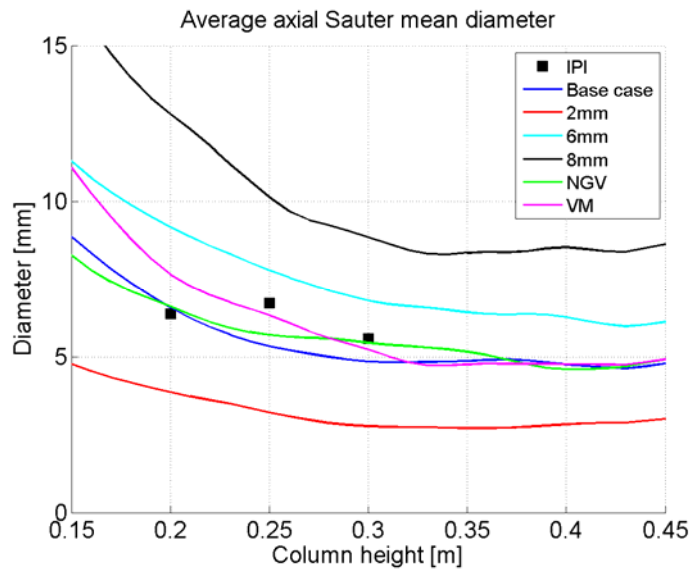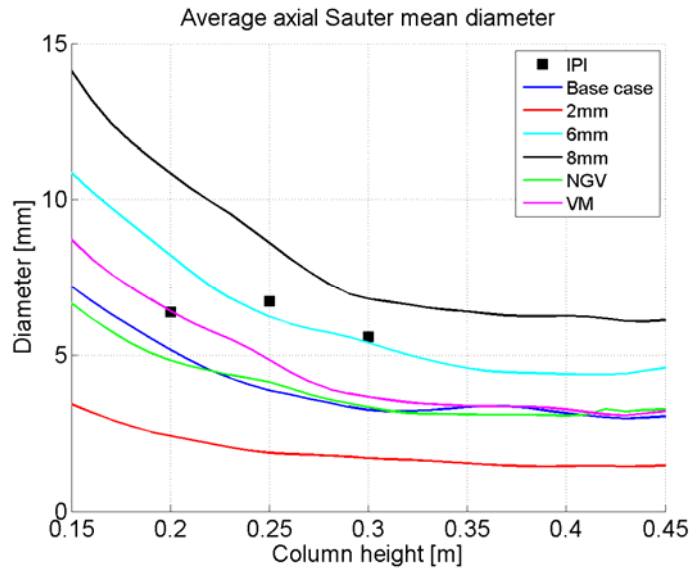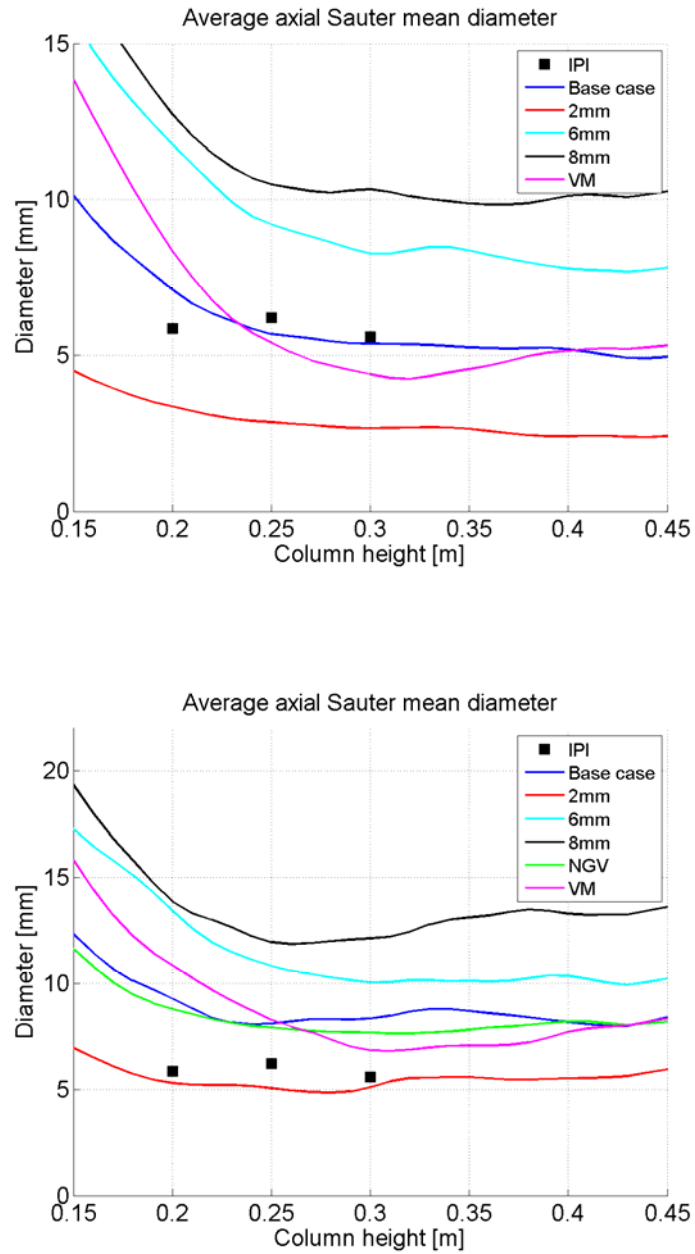
Figure 100 Profiles of time averaged axial d_{32} versus IPI data at the axial centreline. Wu et al. kernels (top) and Moilanen et al. kernels (bottom).
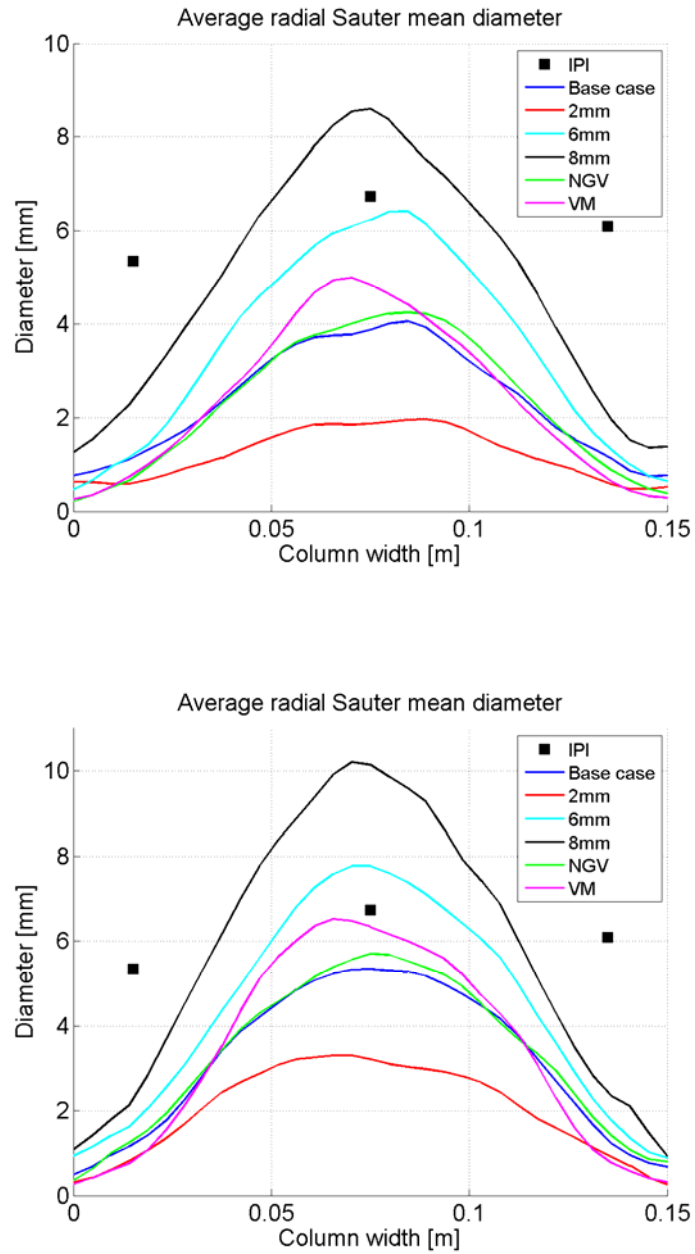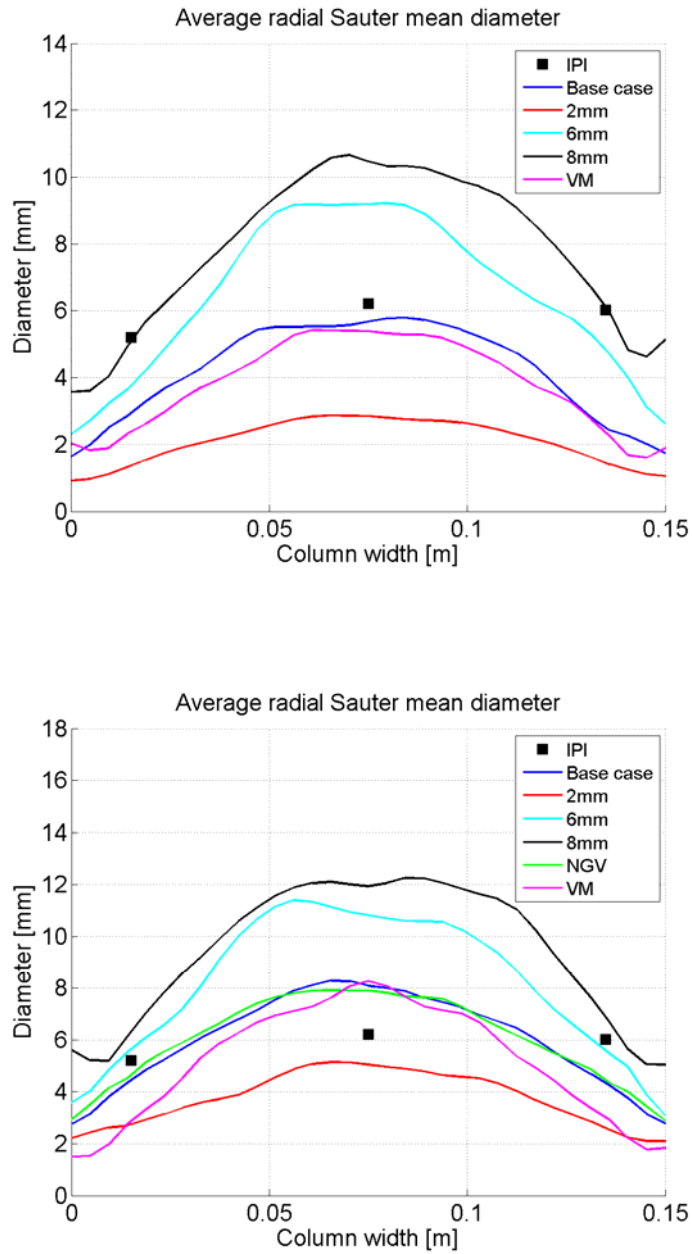
Figure 101 Profiles of time averaged radial d_{32} versus IPI data at the axial centreline. Wu et al. kernels (top) and Moilanen et al. kernels (bottom).
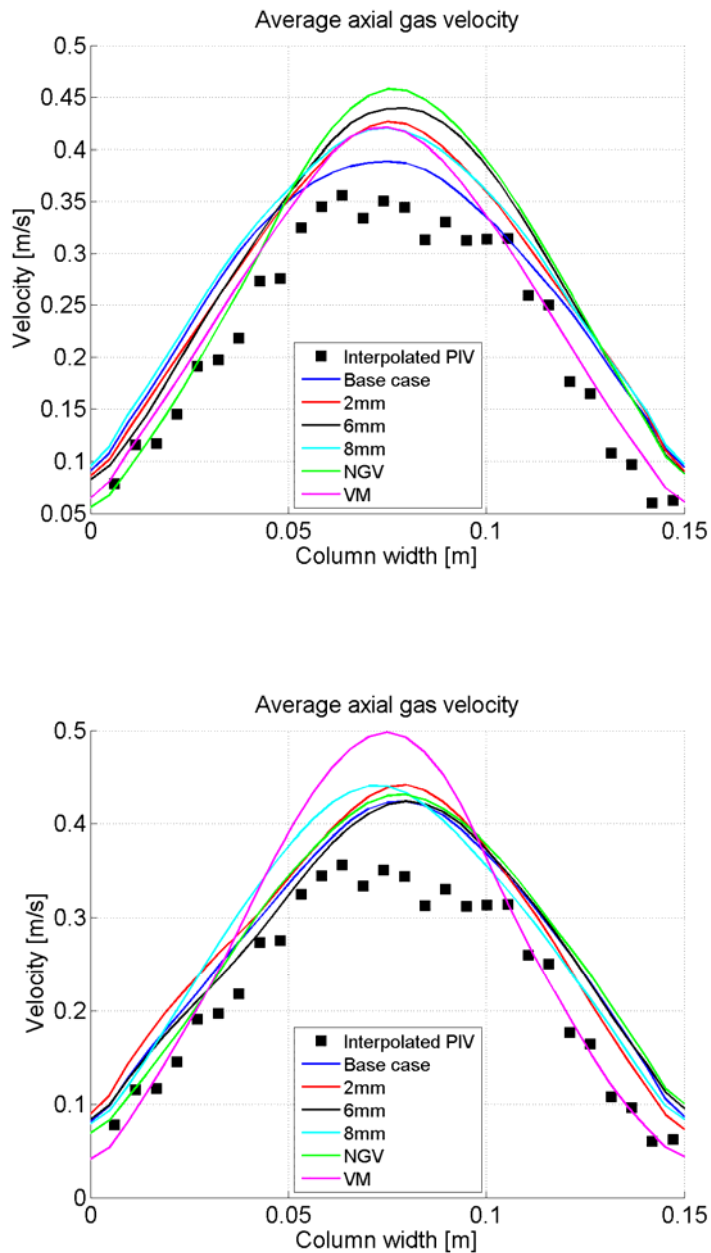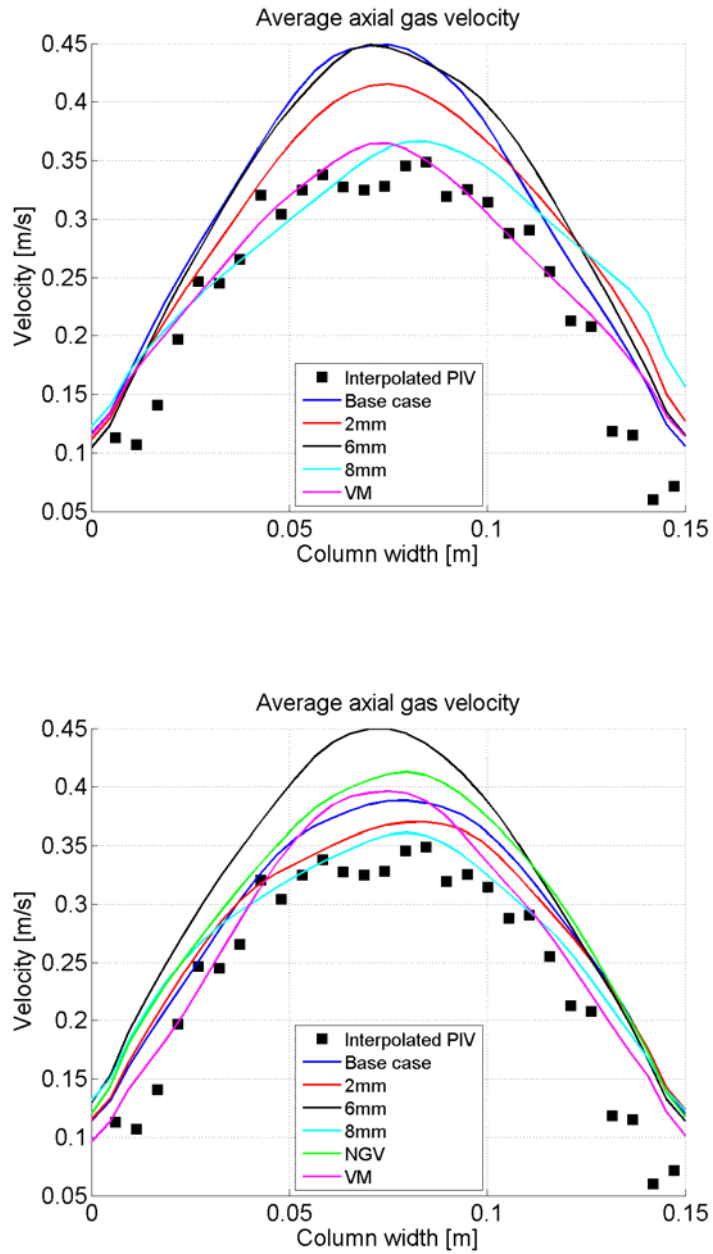
Figure 102 Profiles of time averaged axial gas velocity versus interpolated PIV data at a height of 0.25m and a depth of 0.075m. Wu et al. kernels (top) and Moilanen et al. kernels (bottom).
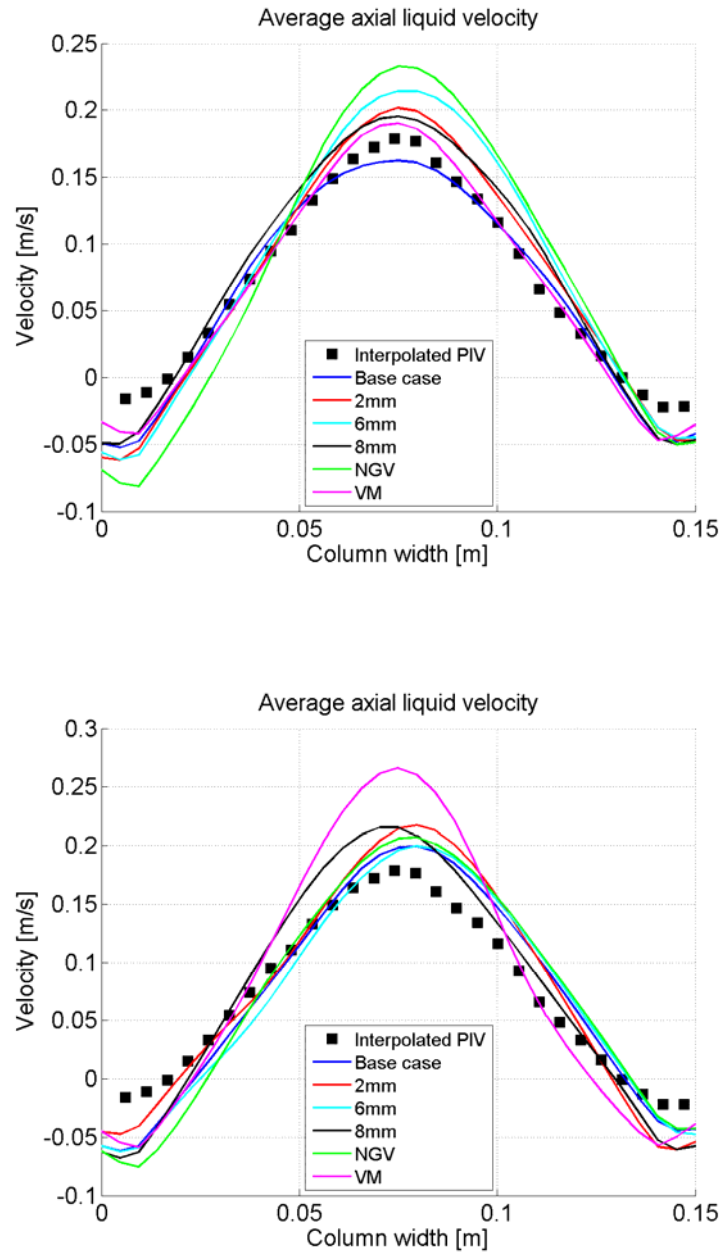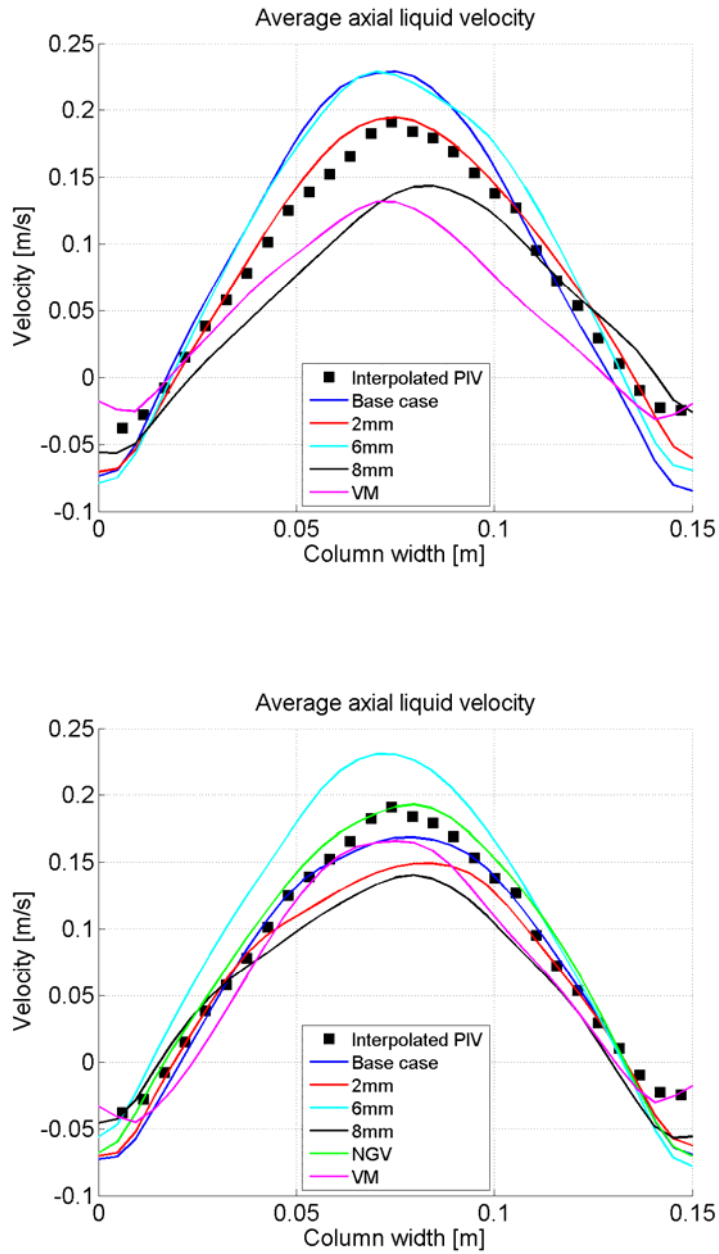
Figure 103 Profiles of time averaged axial liquid velocity versus interpolated PIV data at a height of 0.25m and a depth of 0.075m. Wu et al. kernels (top) and Moilanen et al. kernels (bottom).
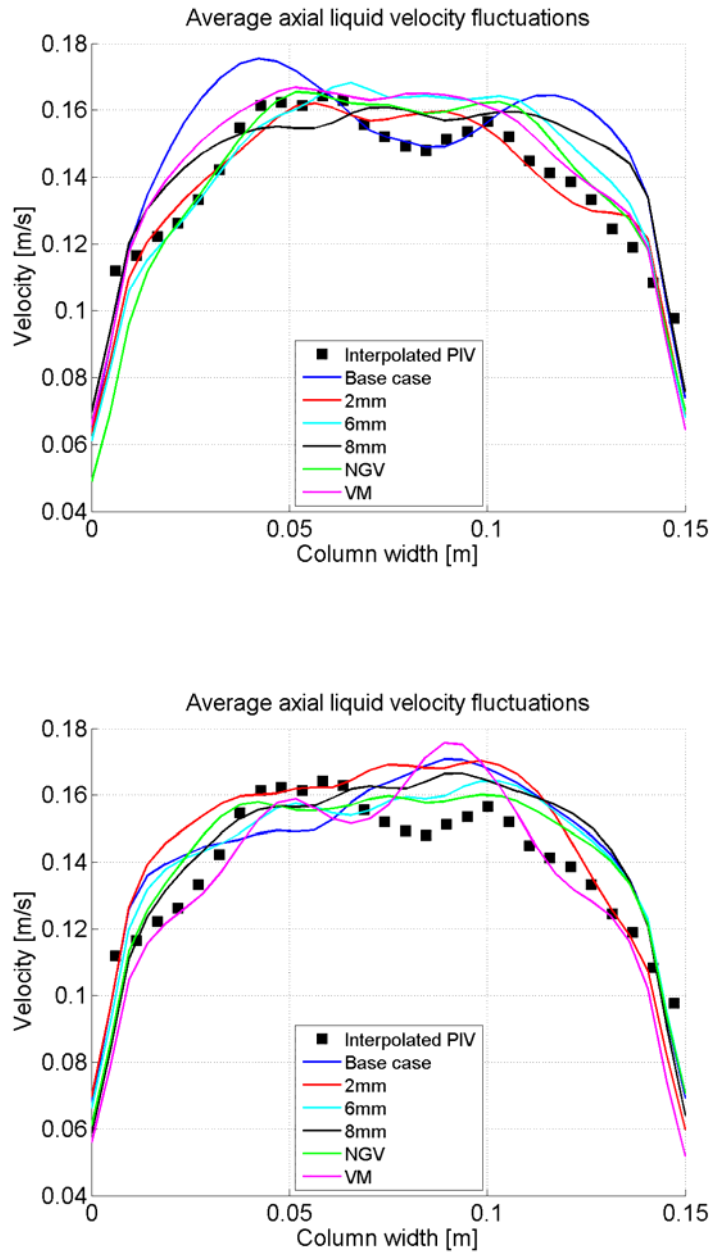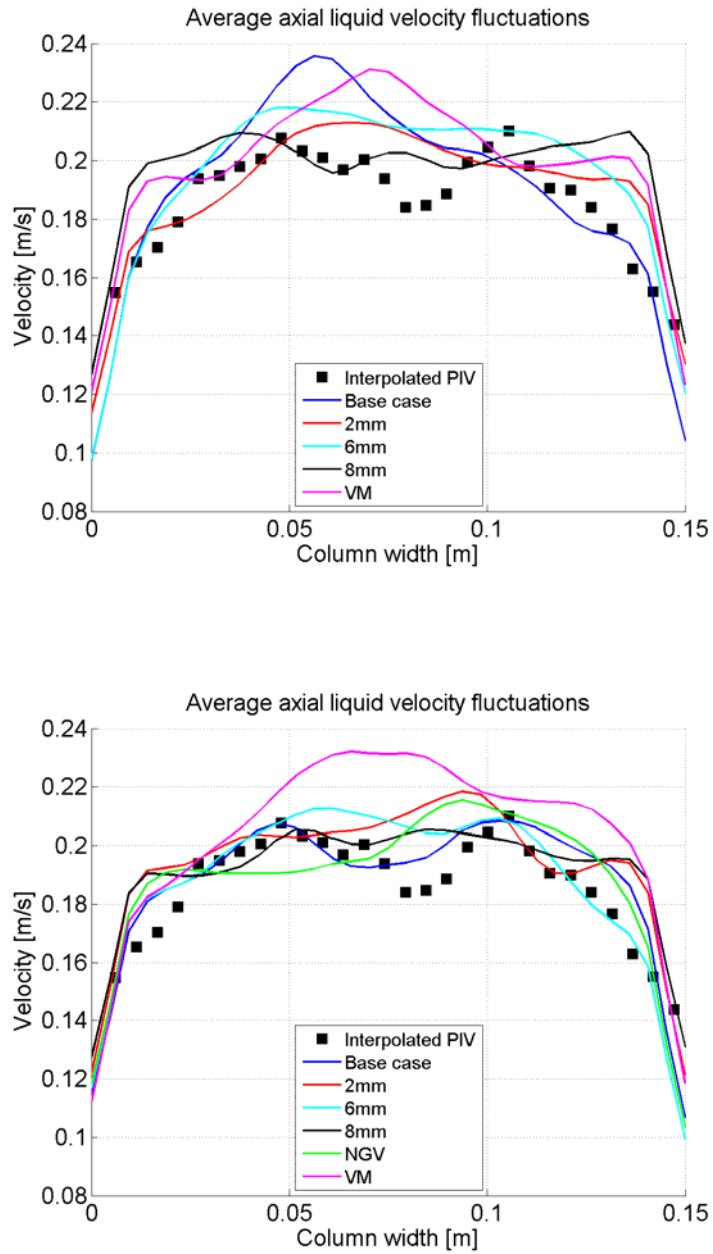
Figure 104 Profiles of time averaged axial liquid velocity fluctuations versus interpolated PIV data at a height of 0.25m and a depth of 0.075m. Wu et al. kernels (top) and Moilanen et al. kernels (bottom).
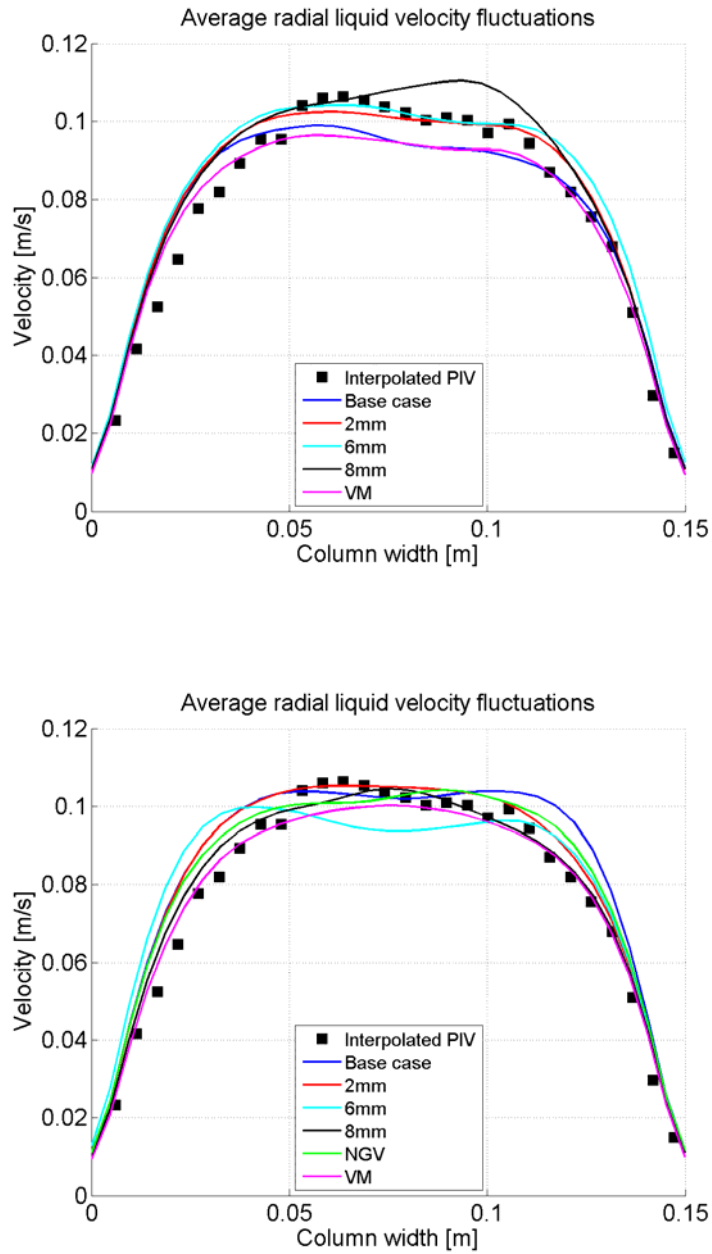
Figure 105 Profiles of time averaged radial liquid velocity fluctuations versus interpolated PIV data at a height of 0.25m and a depth of 0.075m. Wu et al. kernels (top) and Moilanen et al. kernels (bottom).

5.7   Summary

In this chapter numerical simulations of bubble size in the square bubble column have been presented for three superficial gas velocities and two different sets of kernels for coalescence and breakup.

Base case simulations with a superficial gas velocity 4.9 mm/s

The results for two base case IACE simulations with a superficial velocity of 4.9 mm/s have been presented and compared with experimental IPI data and PIV data by Deen (2001).

The simulation with kernels by Moilanen *et al.* (2008) performed better than the simulation with kernels by Wu *et al.* (1998) regarding the prediction of bubble size when compared to the experimental IPI data in the axial direction.

In the radial direction both simulations are under predicting the time averaged d_{32} near the walls quite severely compared to the experimental data. It is observed visually during the experiments that the bubbles form a plume, which fluctuates from left to right quite randomly. In this plume the majority of the bubbles are present. This fluctuating behaviour and plume forming is also observed in the simulations. The averaging of simulated d_{32} is done for every time step in every cell of the computational domain. This is probably not a problem when averaging the simulated d_{32} along the axial centreline of the column as the bubble plume is located in the axial centreline or passing the axial centreline of the column most of the time. It is probably a significant problem when averaging d_{32} in the cells near the walls, as the bubble plume is present quite rarely near the walls compared to the axial centreline. Therefore it would be a good idea to introduce conditional averaging, where the averaging of d_{32} in a cell is only done, when a condition is satisfied. This condition could in this case be a volume fraction threshold, which would be the natural choice for determining when the bubble plume is present in a computational cell.

The change in interfacial area was seen to be minimal for the simulation with the Wu *et al.* (1998) kernels, as the coalescence source terms and especially the breakup source term were very small compared to the simulation with the kernels by Moilanen *et al.* (2008). The breakup source term for the simulation with the Wu *et al.* (1998) kernel was observed to be zero in the plane of view due to low Weber numbers, which are used as a threshold for breakage to occur. The velocity profiles for both cases were in good agreement with the experimental PIV data by Deen (2001) as was expected since the lift coefficient was constant and bubble induced turbulence (BIT) was not employed.

Simulations with superficial gas velocity of 3.2 and 6.6 mm/s

The results from the remaining four base cases with superficial gas velocities of 3.2 m/s and 6.6 m/s have been presented and compared with experimental IPI data and interpolated PIV data from Deen (2001). It was observed that the simulated time averaged d_{32} is very sensitive to superficial gas velocity. The simulated average d_{32} was increasing with increasing superficial velocity as can be seen from Figure 106.
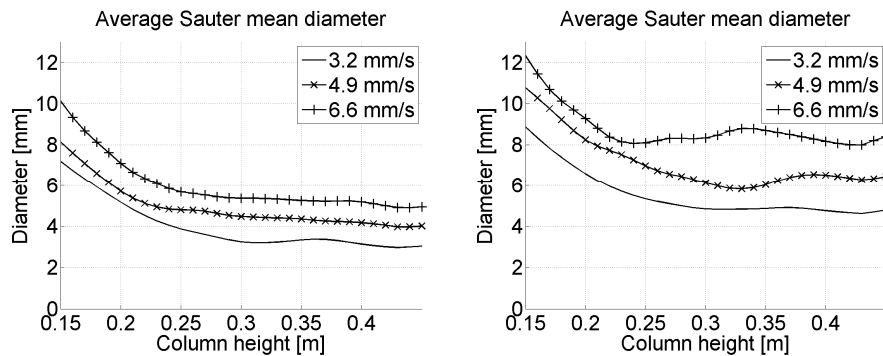
Figure 106 Profiles of simulated time averaged axial d_{32} for different superficial gas velocities with the Wu et al. kernel (left) and the Moilanen et al. kernel (right) in the axial centreline.

This trend was not observed in the experimental IPI data, where the bubble diameter seemed constant.

It was also observed that the velocity profiles for all four remaining base cases were in good agreement with the interpolated PIV data from Deen (2001).

Parameter study

A parameter study on the six base cases has been presented and compared with experimental IPI data and PIV data by Deen (2001).

It was observed that the introduction of a varying lift coefficient (Tomiyama, 2004) did not yield good results both regarding simulated average d_{32} and velocity profiles. The simulated average d_{32} along the axial centreline and the simulated average axial velocity in the core region were severely over predicted. It was quite surprising that the introduction of the varying lift coefficient would result in such a poor prediction, since the varying lift coefficient introduces a physically correct behaviour in the sense that small bubbles migrate toward the walls and larger bubbles migrate toward the centre or core of the column as was observed by Tomiyama (2004). The failure is probably due to the high values of d_{32} observed in the bottom of the column just above the inlet. The lift coefficient in this region is negative, which means that the simulated bubbles in that region migrate toward the centre of the column and introduce a high axial gas velocity in the core region. The IACE kernels especially the breakup kernels are probably not tuned for handling this region with high values of d_{32} just above the inlet and a jet-like flow in the middle of the column occurs.

It was also observed that bubble induced turbulence (BIT) introduced an over prediction of the core velocity and core d_{32} in most of the simulations. In other cases the simulations grew unstable because of added BIT and crashed randomly. The simulations with BIT were therefore not reported in the parameter study.

The parameter study revealed that predictions of average d_{32} from the simulations with added virtual mass (VM) or laminar gas viscosity (NGV) were very similar to the predictions with the base case simulations.

A significant change in the simulated average d_{32} is however observed when changing the inlet bubble diameter. The inlet bubble diameter was set to 2mm, 4mm (base case), 6mm or 8mm. It was observed that the trend of the d_{32} line plots both axially and radially was similar for all simulations with different inlet diameter for all three superficial gas velocities. However the steepness of the curves was growing with increasing inlet diameter axially and toward the walls radially. It is noticed that the difference in average d_{32} in the middle of the column at a height of 0.25m is almost the same as in the inlet for all superficial gas velocities.

The simulated velocity profiles from all cases in the parameter study were in good agreement with experimental PIV data by Deen (2001) and interpolated PIV data. Especially the simulated axial and liquid velocity fluctuations were in excellent agreement with the experimental data. Also the simulated axial liquid velocity was in good agreement with the experimental data. However the simulated axial gas velocity was slightly over predicted by almost every case in the parameter study.

It is noticed that the velocity profiles from the cases with different inlet bubble diameter are not the same. This is a bit strange, as the flow field should be completely decoupled from the bubble size, since varying lift force and BIT is not included.

Chapter 6

Numerical Simulations of Bubble Size in a Pseudo-2D Bubble Column with the IACE Model

6.1   Introduction

In this chapter additional bubble size simulations on a flat pseudo 2D bubble column with the IACE model are compared with experimental data by van den Hengel (2004).

6.2   Simulation settings

In this section the simulation settings for the bubble size simulations on the pseudo 2D bubble column with the IACE model are presented.

6.2.1   Grid and boundary conditions

The grid used in the simulations is a 0.20m x 1.40m x 0.03m square volume meshed with hexahedral cells. The number of cells in the x-, y- and z-direction are 40, 140 and 8 respectively, which gives a total of 44800 hexahedral cells. The geometry with and without mesh can be seen in Figure 107.

135
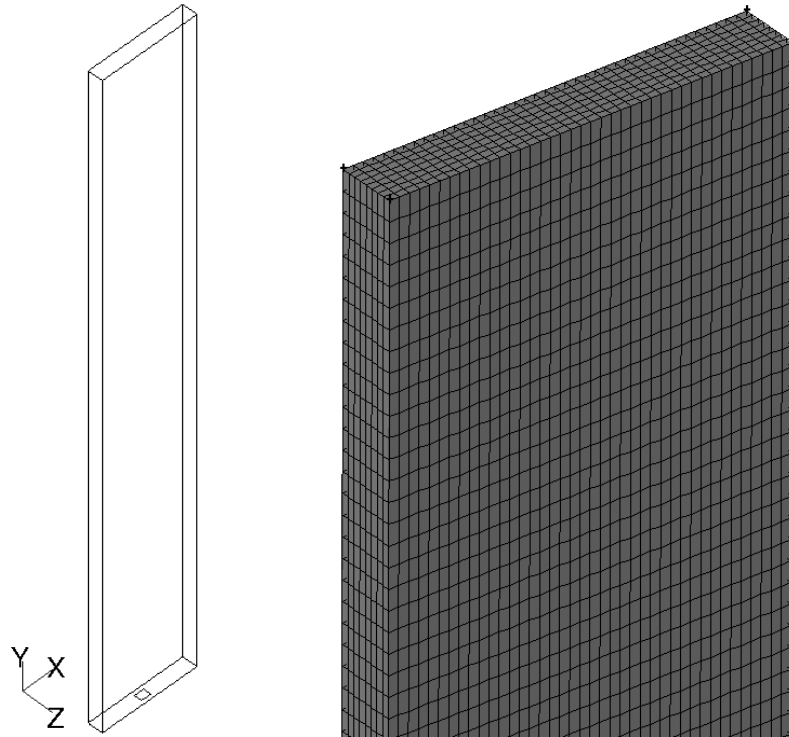
Figure 107 Sketch of the pseudo 2D column with and without mesh.

Inlet

The inlet of the bubble column is modelled as a velocity inlet with 4x4 cells, an area of 0.02 x 0.015m^2 and a superficial gas velocity of 5.56mm/s. The porosity of the distributor is set to 50%, which gives an inlet velocity of 0.22m/s. The diameter of the initial bubbles is set to 2mm as in the work by Bove (2005).

Outlet and walls

The outlet is modelled as a pressure outlet in Fluent 6.3, where the air backflow volume fraction is specified to be zero. The walls are modelled as no-slip boundaries for both phases.

6.2.2 Turbulence modelling

The simulations are run with the LES sub-grid approach proposed by Smagorinsky (1963). Bubble induced turbulence is not employed.

6.2.3 Interface models

The following interfacial forces are employed: distorted bubble drag model by Ishii & Zuber (1979), constant lift ($C_L = 0.5$) or varying lift coefficient proposed by Tomiyama (2004). Added virtual mass is not employed.

6.2.4 Bubble size prediction

The simulations are run with the two different models for coalescence and breakup described in Chapter 3.4.

6.2.5 Conditional averaging

In Chapter 5 it was concluded that it would be a good idea to introduce conditional averaging in the simulations because of the fluctuating movement of the bubble plume. It was proposed that the averaging should be dependent on the volume fraction, since this would be a good measure of the presence of a bubble plume. An initial simulation was run, and the time history of α_G at a height of 0.5m can be seen in Figure 108.
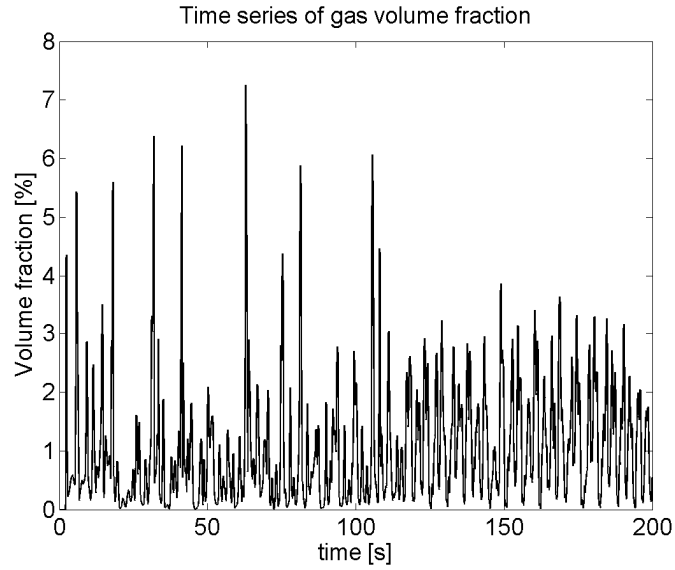
*Figure 108 Time series of simulated gas volume fraction at the axial
           centreline at the height of 0.5m. The simulation is run with
           constant lift ($C_L = 0.5$), $d_{B,inlet}$ = 2mm and kernels for the
           IACE model by Moilanen et al. (2008).*

It is observed that the highest gas volume fraction peaks are
approximately in the range 4% to 7% and the majority of peaks are
approximately in the range 1.5% to 3%. The simulated average gas
volume fraction is predicted to be 0.85%. In Figure 109 a look at the last
20 seconds from Figure 108 is shown. Note the scale on the y-axis.

It is observed that the low local minima of the gas volume fraction range
from close to zero to approximately 0.4%.

From these observations it is chosen to set the threshold of α_G to 0.5%.
This means that averaging of d_{32} is only done when $\alpha_G > 0.5\%$. This
threshold is approximately one tenth of the maximum α_G values observed
at the sampling location.
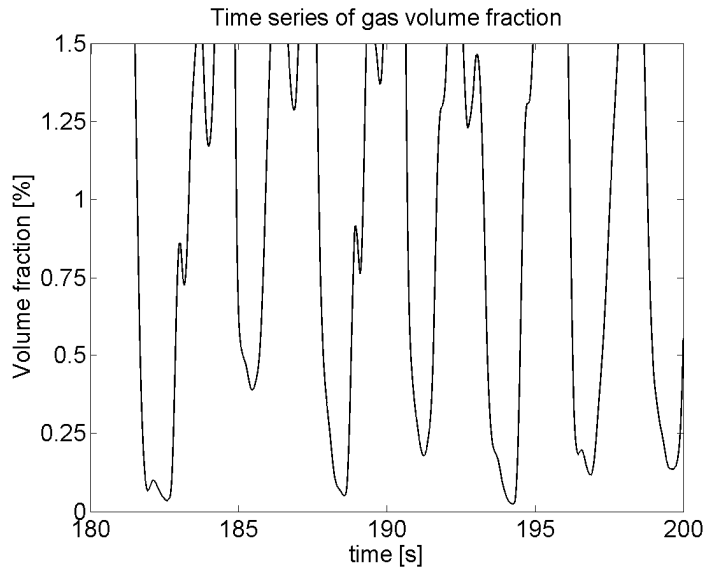
Figure 109 The last 20 seconds from Figure 108. Note the scale on the y-axis.

6.2.6 Other settings

The simulations are 1st order implicit transient in three dimensions. The time step size is set to 0.0025s, and the simulation time is set to 200s with (conditional) averaging done on the last 150s exactly as for the IACE simulations on the square bubble column. Third order spatial discretisation schemes are employed (QUICK). A typical simulation was run on 4 AMD Athlon XP 1.4 GHz nodes and took approximately 14 days.

6.3 Results

In this section the results from the IACE simulations on the pseudo 2D column are presented and compared with the experimental shadow imaging data by van den Hengel (2004). Since van den Hengel (2004)

only measured the bubble size, no velocity data is available only bubble size data.

6.3.1   Simulation with Wu *et al.* kernels

In Figure 110 the simulated conditional time averaged d_{32} is compared with experimental data by van den Hengel (2004) along the axial centreline.

Figure 110 Axial profiles of simulated conditional time averaged d_{32} versus experimental data by van den Hengel (2004) along the axial centreline of the column. The Wu et al. kernels are employed.

It is observed that the simulated conditional time averaged d_{32} along the axial centreline is decreasing rapidly within the first 15cm above the inlet. Through the remaining part of the column the simulated average d_{32} is more or less steady at 0.1mm. The simulated average d_{32} does not fit the experimental data at all.

6.3.2 Simulation with Moilanen *et al.* kernels

In Figure 111 simulated average d_{32} along the axial centreline for different cases is presented. The cases are listed in Table 9.

Table 9   Simulations with the Moilanen et al. kernels.

Case	$d_{B,inlet}$	C_L	μ_{eff}	VM
CL	2mm	0.5	$\mu_{lam}+\mu_t$	no
TL	2mm	Tomiyama (2004)	$\mu_{lam}+\mu_t$	no
4mm+CL	4mm	0.5	$\mu_{lam}+\mu_t$	no
4mm+TL	4mm	Tomiyama (2004)	$\mu_{lam}+\mu_t$	no
BIT+CL	2mm	0.5	$\mu_{lam}+\mu_t+\mu_{BIT}$	no
BIT+TL	2mm	Tomiyama (2004)	$\mu_{lam}+\mu_t+\mu_{BIT}$	no

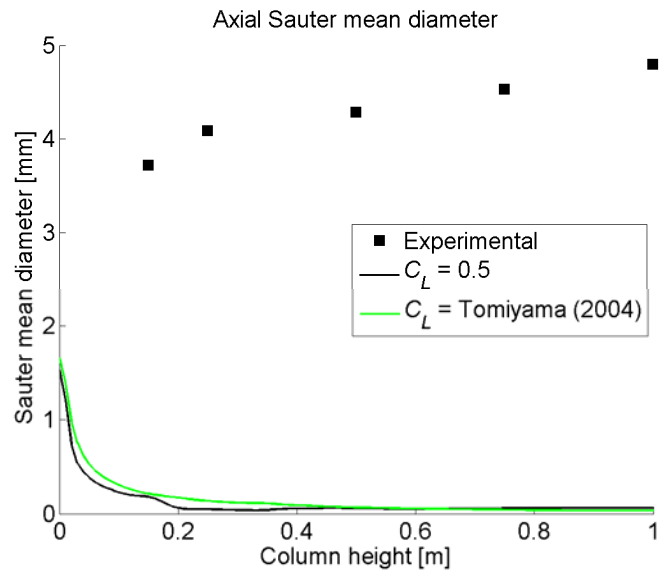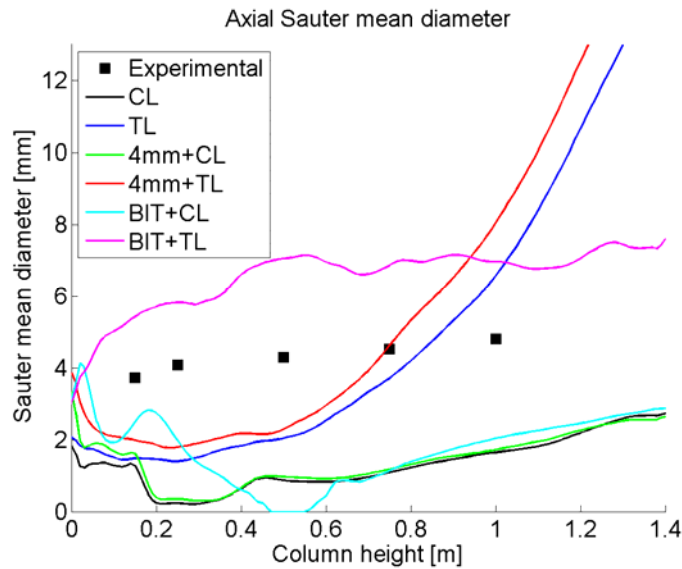*Figure 111 Plots of simulated average d_{32} versus experimental data by van den Hengel (2004) in the axial centreline of the column. The Moilanen et al. kernels are employed.*

It is observed that none of the simulations are in excellent agreement with the experimental data. The simulated average d_{32} is lower than the

experimental data for all simulations in the lower half of the column except for case BIT+TL. In the upper half of the column the simulations with the Tomiyama lift coefficient predict a higher average d_{32} than the experimental values.

It is noticed that the simulated profiles of d_{32} with constant lift have the same slope as the experimental data in the upper part of the column. This is not the case for the simulations with the Tomiyama lift coefficient.

When employing BIT the trend of the curves changes quite dramatically. The case BIT+TL is the only case that shows an increasing average d_{32} up through the column. The trend of the experimental data also seems to be captured with BIT+TL. Case BIT+TL seems to be in better agreement with the experimental data.

Contour plots of conditional time averaged d_{32}, α_G, a_i and $u_{G,axial}$ are shown for the cases "CL" and "TL" in Figure 112. It is observed that the flow is almost channelling for the case "TL", and more spread toward the walls for the case "CL". This is probably due to the magnitude of the lift coefficient in the two cases.
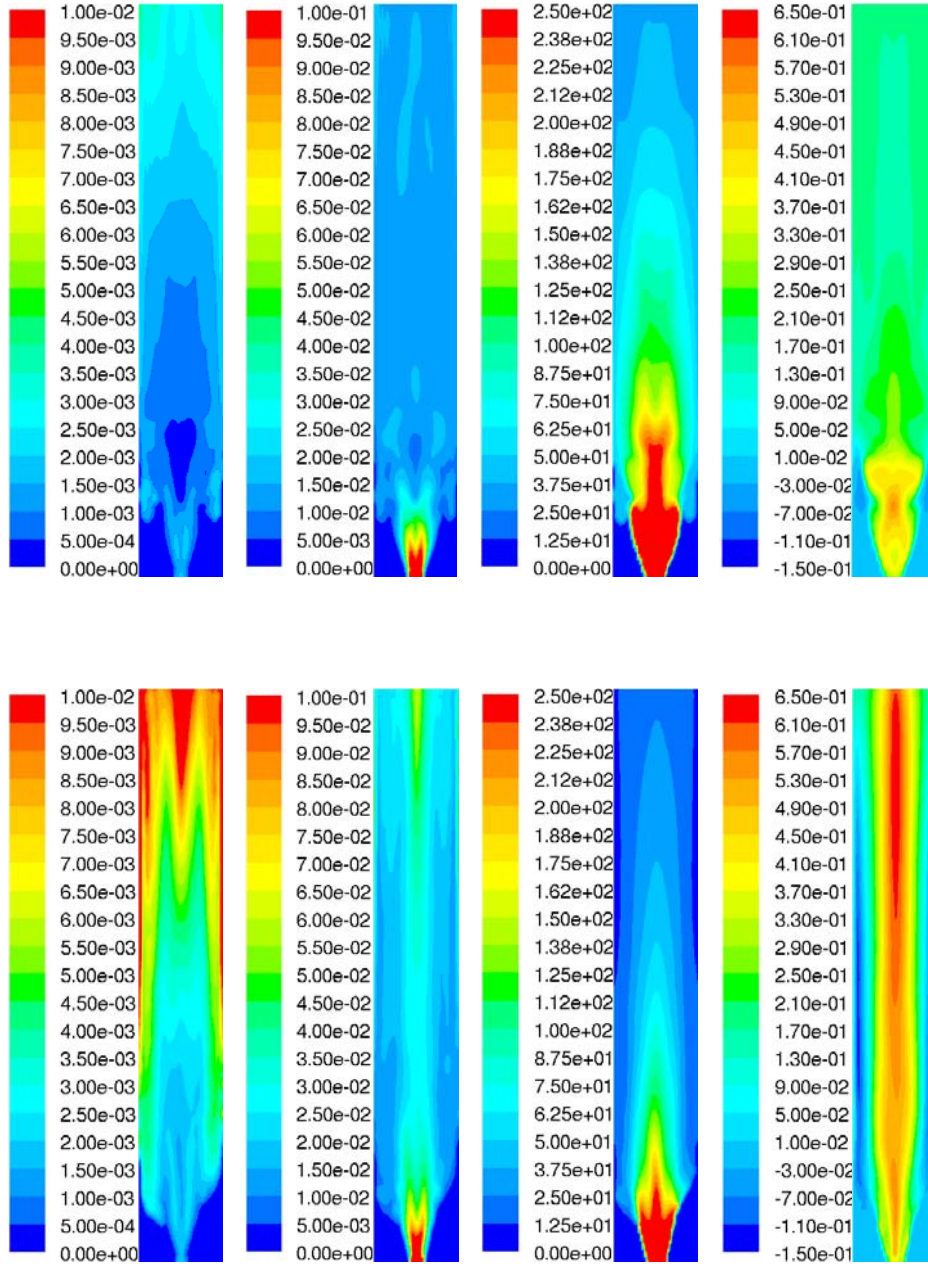
Figure 112 Contour plots of conditional time averaged d_{32}, α_G, a_i and $u_{G,axial}$ (left to right) for the cases "CL" (top) and "TL" (bottom) in the z-plane at a depth of 0.015m.

Even though the flow is almost channelling for the case "TL", the conditional time averaged d_{32} in the radial direction is not decreasing as expected when the Tomiyama lift coefficient is applied. It is observed from Figure 113 that the instantaneous d_{32} for case "TL" is seldom above 4.4mm, which is the approximate threshold, where the Tomiyama lift coefficient decreases from a constant value of 0.29 towards zero and further on toward a negative value for $d_{32} > 5.8$mm (Figure 32).
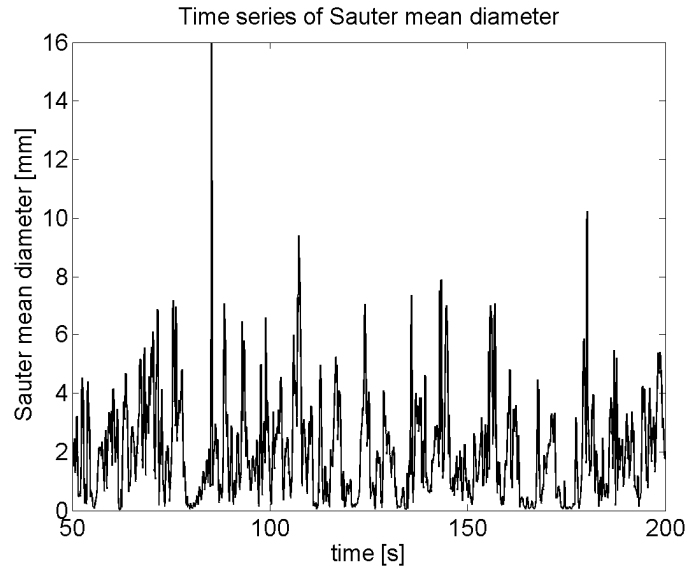
Figure 113 Time series of simulated d_{32} for case "TL" in the axial centreline at a height of 0.5m.

Since the instantaneous d_{32} is below 5.8mm most of the time, the lift force is positive, and all the bubbles are sent toward the walls.

Effect of conditional averaging

The effect of conditional averaging is shown in Figure 114. It is observed that the difference in d_{32} along the axial centreline is rather small when changing the threshold for conditional averaging. In the radial direction the difference is much more significant toward the walls.
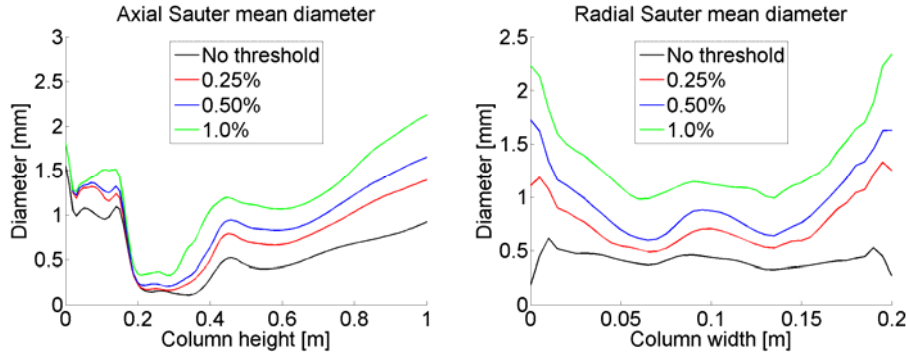
Figure 114 Profiles of simulated conditional time averaged d_{32} with different thresholds for case "CL". Left: Axial profiles along the axial centreline. Right: Radial profiles at a height of 0.5m and a depth of 0.015m.

6.4   Summary

In this chapter the IACE model with kernels by Wu *et al.* and Moilanen *et al.* has been employed to simulate the bubble size distribution in a flat pseudo 2D column. The results have been compared to the experimental data by van den Hengel (2004).

The simulations with the Wu *et al.* kernels under predicted the conditional time averaged d_{32} severely and the trend of the experimental data along the axial centreline was not captured. It was observed that d_{32} was decreasing along the axial centreline with increasing height. The experimental data show the exact opposite.

The simulations with the Moilanen *et al.* kernels under predicted the conditional time averaged d_{32} except for the simulation with BIT and Tomiyama lift, which over predicted d_{32}. It was observed that the trend of the experimental data along the axial centreline from a height of 0.5m and upwards was captured when employing a constant lift force of 0.5. When employing a varying lift force as proposed by Tomiyama (2004) without BIT, the increase in d_{32} was very steep compared to the experimental data. The simulation with BIT and Tomiyama lift showed an increasing average d_{32} along the axial centreline, and the slope of the

curve matched the slope of the experimental data. This case showed the better agreement with the experimental data.

The effect of conditional averaging was examined with respect to simulated average d_{32}, and the effect is highest in the radial direction toward the walls as expected.

The flow in the column was observed to spread toward the walls when employing a constant lift coefficient of 0.5. When using the lift coefficient proposed by Tomiyama (2004) the flow was observed to be almost channelling along the axial centreline. This was concluded to be due to the difference in magnitude between the two lift coefficients and not because of the ability of the Tomiyama lift coefficient to become negative, which results in migration of the large bubbles toward the middle of the column.

Chapter 7

Conclusions and Future Work

In this thesis the bubble size distribution (BSD) in a square bubble column has been measured with Interferometric Particle Imaging and Particle Tracking Velocimetry (IPI/PTV). Computational Fluid Dynamics (CFD) has been employed to model the flow and bubble size in the square bubble column and a flat pseudo-2D bubble column.

7.1   Experiments

From the experimental IPI results on the square bubble column it was found that the bubble Sauter Mean Diameter (SMD) was approximately 6.0mm in the field of view. This was supported by visual observations. The SMD seems to be constant in the axial direction, whereas the bubble diameter profiles in the radial direction show that the SMD is smaller near the walls when compared to the SMD at the axial centreline. This was also expected as large bubbles migrate toward the middle or core region of the bubble column and smaller bubbles migrate toward the wall, which is in accordance with experimental observations. The SMD seems to be decreasing with increasing superficial gas velocity when looking at both axial and radial diameter profiles.

The experimental PTV results were not in good agreement when compared to experimental Particle Imaging Velocimetry (PIV) data from Deen (2001). The core velocity was too low and the velocity toward the walls was a bit too high. It is believed that this was due to a too large

time between bursts, which is essential for the quality of the PTV data. Furthermore a mirroring effect was observed at two distinct locations in the field of view, which distorted the data, so that the data was unusable in the vicinity of those locations.

7.2 Flow modelling

The flow pattern in the square bubble was simulated with Fluent 6.3 and compared with experimental PIV data by Deen (2001). The diameter of the dispersed phase was kept at a constant value of 4mm.

Excellent agreement with experimental data were obtained by employing the Large Eddy Simulation (LES) sub-grid approach as proposed by Smagorinsky (1963), the distorted drag model by Ishii & Zuber (1979) and a constant lift force with $C_L = 0.5$. It was concluded in Chapter 4.4 that Bubble Induced Turbulence (BIT) and bubble size dependent lift force should not be used when simulating the flow pattern in the bubble column with a constant diameter of the dispersed phase.

7.3 Bubble size modelling

The mean bubble size in the square bubble column was modelled with an Interfacial Area Concentration Equation (IACE) approach and compared with experimental IPI data. Kernels by Wu *et al.* (1998) and Moilanen *et al.* (2008) were employed to account for coalescence and breakage.

It was observed with a superficial gas velocity of 4.9 mm/s that the simulation with kernels by Moilanen *et al.* (2008) performed better than the simulation with kernels by Wu *et al.* (1998) regarding the prediction of bubble size in the axial direction when compared to the experimental IPI data. In the radial direction both simulations are under predicting the time averaged SMD, d_{32}, near the walls quite severely compared to the experimental data. It is believed that by introducing conditional averaging with a volume fraction threshold this under prediction can me minimized or even eliminated.

The simulated time averaged d_{32} was observed to be increasing with superficial gas velocity. This trend was however not seen in the experimental IPI data, where the bubble size seemed constant or even slightly decreasing with increasing superficial velocity.

Through a parameter study it was observed that introduction of a bubble size dependent lift force and bubble induced turbulence did not yield good results as the bubble diameter was severely over predicted along the axial centreline of the bubble column. Also it was seen that the inlet bubble diameter has a significant influence on the time averaged d_{32}.

The mean bubble size in the flat pseudo 2D bubble column was modelled and compared with experimental data by van den Hengel (2004). Kernels by Wu *et al.* (1998) and Moilanen *et al.* (2008) were employed in the IACE model.

The kernels by Wu *et al.* under predicted the SMD in the column when compared to the experimental data and the trend of the axial SMD was not captured. The Moilanen *et al.* kernels did a better prediction of the axial SMD, but none of the simulations were in excellent agreement with the experimental data. It was observed in Chapter 6.3 that when employing BIT and a bubble size dependent lift force, the trend of the experimental data was captured.

The two different kernels used for predicting bubble size were not specifically developed for bubble columns. The kernels by Wu *et al.* (1998) were developed for one dimensional area-averaged vertical bubbly pipe flow for nuclear engineering and the kernels by Moilanen *et al.* (2008) were developed for stirred tanks. Even though the kernels, especially the Moilanen *et al.* (2008) kernel, in some cases show good agreement with experimental data, it is also seen that when including physically correct effects such as a bubble size dependent lift force or bubble induced turbulence, the kernels fail to predict the mean bubble size satisfactorily.

The lift force is essential for correct modelling of flow pattern in bubble columns, as this interfacial force is the main driving force in achieving a fluctuating behaviour of the bubble plume. Since the IACE model only yields one single bubble size in every cell of the computational domain,

the effect of the bubble size dependent lift force is diminished, which could explain why the jet-like flow in the core region of the bubble column occur. Bove (2005) clearly showed with three bubble size classes that the smaller bubbles were located near the walls and the larger bubbles were confined to the core region of the bubble column.

7.4   Future work

On the basis of the conclusions drawn, some future work considerations are presented in the following.

Experimental work

The time between bursts should be optimized by repeating the experiment, so that the PTV data could be compared with experimental PIV data by Deen (2001).

A different approach to measuring the bubble size in the square bubble column could also be employed. The shadow imaging technique used by van den Hengel (2004) would be an obvious choice, since the technique is quite simple. This would allow for comparison of BSD from the two different techniques.

Computational work

Bove *et al.* (2004) showed that the discretisation of the momentum equations and volume fraction equations is essential for correct prediction of the flow field. A fluctuating bubble plume using 2nd order flux corrected central differencing was obtained without employing lift force. In this work the lift force was essential for obtaining bubble plume fluctuations using third order discretisation (QUICK). It would therefore be interesting to conduct a study on the discretisation schemes.

In the present work the kernels for the IACE model were not manipulated. Even though the IACE modelling approach might not be suitable for bubble columns it should be investigated what effect a simple tuning or modification of kernels would have on the simulation results. It would also be interesting to search and implement different kernels for coalescence and breakage into the IACE model.

Instead of using the two-phase IACE approach for modelling bubble size in bubble columns, it would be interesting to use multiphase approaches as the Quadrature Method Of Moments (QMOM), the Direct Quadrature Method Of Moments (DQMOM) or the method of Parallel Parent and Daughter Class (PPDC). In these approaches the dispersed phase is usually divided into two to four separate phases, each having its own diameter size and velocity field. This would probably increase the accuracy of the bubble size and flow field predictions, but the computational cost will also increase quite dramatically.

References

Albrecht, H.E., Borys, M., Damaschke, N. and Tropea, C. (2003). *Laser Doppler and Phase Doppler Measurement Techniques*. Springer-Verlag Berlin Heidelberg.

Bannari, R., Kerdouss, F., Selma, B., Bannari, A. and Proulx, P. (2008). *Three-dimensional mathematical modelling of dispersed two-phase flow using class method of population balance in bubble columns*. Computers and Chemical Engineering, **32**, 3224-3237.

Becker, S, Sokolichin, A. and Eigenberger, G. (1994). *Gas-liquid flow in bubble columns and loop reactors: Part II: Comparison of detailed experiments and flow simulations*. Chem. Eng. Sci., **49**, 5747-5762.

Becker, S., De Bie, H. and Sweeney, J. (1999). *Dynamic flow behaviour in bubble columns*. Chem. Eng. Sci., **54**, 4929-4935.

Bhavaraju, S.M., Russell, T.W.F. and Blanch, H.W. (1978). *The design of gas sparged devices for viscous liquid systems*. AIChE Journal, **24**, 454-466.

Borchers, O., Busch, C., Sokolichin, A. and Eigenberger, G. (1999). *Applicability of the standard k-ε turbulence model to the dynamic simulation of bubble columns. Part ii: Comparison of detailed experiments and flow simulations*. Chem. Eng. Sci., **54**, 5927-5935.

Bove, S., Solberg, T. and Hjertager, B.H. (2004). *Numerical aspects of bubble column simulations*. International Journal of Chemical Reactor Engineering, **2**, A1.

153

Bove, S., Solberg, T. and Hjertager, B.H. (2005). *A novel algorithm for solving the population balance equations: The parallel parent and daughter classes. Derivation, analysis and testing*. Chem. Eng. Sci., **60**, 1449-1464.

Bove, S. (2005). *Computational Fluid Dynamics of Gas-Liquid Flows including Bubble Population Balances*. **Ph.D. thesis**, Aalborg University Esbjerg, Denmark.

Bröder, D., Sommerfeld, M. and Tisler, T. (1998). *Analysis of the hydrodynamics in a bubble column by phase-doppler anemometry*. Third Int. Conf. on Multiphase Flow, **ICMF'98**, Lyon, France.

Bröder, D. and Sommerfeld, M. (2000). *A PIV/PTV system for analysing turbulent bubbly flows*. **Proceedings of 10th Int. Symp. on Appl. of Laser Techniques to Fluid Mech**., Lisbon, Portugal.

Cheung, S.C.P., Yeoh, G.H. and Tu, J.Y. (2007). *On the numerical study of isothermal vertical bubbly flow using two population balance approaches*. Chem. Eng. Sci., **62**, 4659-4674.

Dantec (2003). *Flowmap Particle Sizer Installation & User's guide*. Dantec Dynamics A/S, Skovlunde, Denmark.

Davidson, L. and Schuler, B.O.G. (1960). *Bubble formation at an orifice in a viscous liquid*. Trans. Inst. Chem. Engrs., **38**, 144.

Deen, N.G., Solberg, T. and Hjertager, B.H. (2001). *Large eddy simulation of the gas-liquid flow in a square cross-sectioned bubble column*. Chem. Eng. Sci., **56**, 6341-6349.

Deen, N.G. (2001). *An Experimental and Computational Study of Fluid Dynamics in Gas-Liquid Chemical Reactors*. **Ph.D. thesis**, Aalborg University Esbjerg, Denmark

Delhaye, J.M. (2001). *Some issues related to the modelling of interfacial areas in gas-liquid flows, II. Modeling the source terms for dispersed flows*, C. R. Acad. Sci. Paris, **t. 329, Série IIb**, 473–486.

Delnoij, E., Kuipers, J.A.M., van Swaaij, W.P.M., and Westerweel, J. (2000). *Measurement of gas-liquid two-phase flow in bubble columns using ensemble correction PIV*. Chem. Eng. Sci., **55**, 3385-3395.

Dillerop, C. (2000). *Numerical and experimental study of three dimensional gas and liquid flow in bubble columns*. **M.Sc. Thesis**, University of Twente, The Netherlands.

Drew, D.A. (1983). *Mathematical modeling of two-phase flow*. Ann. Rev. Fluid Mech, **15**, pp. 261-291.

Drew, D.A. and Passmann, S.L. (1999), *Theory of multicomponent fluids*. Applied Mathematical Sciences, **135**, Springer.

Glover, A.R., Skippon, S.M. and Boyle, R.D. (1995). *Interferometric laser imaging for droplet sizing: a method for droplet-size measurement in sparse spray systems*. Applied Optics, **34**, 8409-8421.

Hansen, R., Madsen, J., Solberg, T. and Hjertager, B.H. (2007). *Experimental determination of the bubble size distribution in a square bubble column by the use of IPI*. ICMF-2007, Paper No. **342,** Leipzig, Germany.

Hansen, R., Solberg, T. and Hjertager, B.H. (2008). *CFD-modelling of bubble size in a bubble column using the one-group interfacial area concentration equation*. 6th International Conference on CFD in Oil & Gas, Metallurgical and Process Industries, Paper No. **039,** SINTEF/NTNU, Trondheim, Norway.

Hibiki, T. and Ishii, M. (2002). *Development of one-group interfacial area transport equation in bubbly flow systems*. Int. J. of Heat Mass Transfer, **45**, 2351–2372

Ishii M. and Chawla T.C. (1979). *Local drag laws in dispersed two-phase flow*. Technical report, **ANL-79-105**, Argonne, National Laboratory, Chicago.

Ishii, M. and Zuber, N. (1979), *Drag coefficient and relative velocity in bubbly, droplet and particulate driven flows*. AIChE J., **25**, 843-855.

Ishii, M. and Kim, S. (2001). *Micro four-sensor probe measurement of interfacial area transport for bubbly flow in round pipes*. Nuclear Engineering and Design, **205**, 123-131.

Jacobsen, H.A., Sannæs, B.H., Grevskott, S. and Svendsen, H.F. (1997). *Modelling of vertical bubble-driven flows*. Ind. Eng. Chem. Res., **36**, 4052-4074.

König, G., Anders, K. and Frohn A. (1986). *A new light scattering technique to measure the diameter of periodically generated moving droplets*. Journal of Aerosol Science, **17**, 157-167.

Krepper, E., Lucas, D., Frank, T., Prasser, H-M. and Zwart, P.J. (2008). *The inhomogeneous MUSIG model for the simulation of polydispersed flows*. Nuclear Engineering and Design, **238**, 1690-1702.

Lage, P.L.C. and Espósito, R.O., (1999). *Experimental determination of bubble size distributions in bubble columns: prediction of mean bubble diameter and gas hold up*. Powder Technology, **101**, 142-150.

Laín, S, Bröder, D. and Sommerfeld, M. (1999). *Experimental and numerical studies of the hydrodynamics in a bubble column*. Chem. Eng. Sci., **54**, 4913-4920.

Lane, G.L., Schwarz, M.P. and Evans, G.M. (2005). *Numerical modelling of gas-liquid flow in stirred tanks*. Chemical Engineering Science, **60**, 2203-2214.

Madsen, J., Harbo, J., Nonn, T.I., Blondel, D., Hjertager, B.H. and Solberg, T. (2003). *Measurement of droplet size and velocity distributions in sprays using Interferometric Particle Imaging (IPI) and Particle Tracking Velocimetry (PTV)*. Proc. ICLASS 2003, Paper No. **0906**, Sorrento, Italy.

Madsen, J. (2006). *Computational and Experimental Study of Sprays from the Breakup of Water Sheets*. Ph.D. thesis, Aalborg University Esbjerg, Denmark.

Maeda, M., Kawaguchi, T. and Hishida, K. (2000). *Novel interferometric measurement of size and velocity distribution of spherical particles in fluid flows*. Measurement Science and Technology, **11**, L13-L18.

Magaud, F., Souhar, M., Wild, G. and Boisson, N., (2001). *Experimental study of bubble column hydrodynamics*, Chem. Eng. Sci., **56**, 4597-4607.

Majumder, S.K., Kundu, G. and Mukherjee, D., (2006). *Bubble size distribution and gas-liquid interfacial area in a modified downflow bubble column*. Chemical Engineering Journal, **122**, 1-10.

Moilanen, P., Laakkonen, M., Visuri, O., Alopaeus, V., Aittamaa, J. (2008). *Modelling mass transfer in an aerated 0.2 m^3 vessel agitated by Rushton, Phasejet and Combijet impellers*. Chemical Engineering Journal, **142**, 95-108.

Pope, S.B. (2000), *Turbulent Flows*. Cambridge University Press, Cambridge.

Rafique, M., Chen, P. and Duduković, M.P. (2004). *Computational modeling of gas-liquid flow in bubble columns*. Reviews in Chemical Engineering, **20**, 225-375.

Sanyal, J., Marchisio, D.L., Fox, R.O. and Dhanasekharan, K. (2005). *On the comparison between population balance models for CFD simulation of bubble columns*. Ind. Chem. Res., **44**, 5063-5072.

Sato, Y. and Sekoguchi, K. (1975). *Liquid velocity distribution in two-phase bubble flow*. Int. J. Multiphase Flow, **2**, 79-95.

Smagorinsky, J. (1963). *General circulation experiments with the primitive equations*. Mon. Weather Rev., **91**, 99-165.

Tomiyama, A. (2004). *Drag, lift and virtual mass forces acting on a single bubble*. **3rd Int. Symp. on Two-phase Flow Modelling and Experimentation**, Pisa, Italy, 22-24 Sept.

van den Hengel, E. (2004). *Multi-level modeling of gas-liquid two-phase flow in a bubble column*. **Ph.D. thesis**, University of Twente, The Netherlands.

Wellek R.M., Agrawal A.K. and Skelland A.H.P. (1966). *Shapes of liquid drops moving in liquid media*. AIChE Journal, **12**, 854-862.

Wu Q., Kim S. and Ishii M. (1988). *One-group interfacial area transport in vertical bubbly flow*. Int. J. Heat Mass Transfer, **41,** 8-9, 1103-1112.

Yao, W. and Morel, C. (2004). *Volumetric interfacial area prediction in upwards bubbly two-phase flow*. Int. J. of Heat Mass Transfer, **47**, 307–328

Zhang, D., Deen, N.G. and Kuipers, J.A.M. (2005). *Numerical simulation of dynamic flow behavior in a bubble column: comparison of the bubble-induced turbulence models in the k-ε model*. Fourth International Conference on CFD in the Oil and Gas, Metallurgical & Process Industries, Trondheim, Norway

Zhang, D., Deen, N.G. and Kuipers, J.A.M. (2006). *Numerical simulation of the dynamic flow behavior in a bubble column: A study of closures for turbulence and interface forces*. Chem. Eng. Sci., **61**, 7593-7608.

Zhang, D. (2007). *Eulerian modelling of reactive gas-liquid flow in a bubble column*. **Ph.D. Thesis**, University of Twente, The Netherlands.